TriDurLE

National Center for Transportation
Infrastructure Durability & Life-Extension

EVALUATION OF DOWNDRAG LOADS ON BRIDGE PILE FOUNDATIONS IN INUNDATED COLLAPSIBLE SOILS

Prepared by:

Mohamed Ashour, Ph.D., P.E.
Professor and Head of Civil Engineering Program

And

Aser Abbas
Graduate Research Assistant

Department of Civil and Mechanical Engineering
Alabama A&M University

Project No. 2020-AA&M-01

June 2022

DISCLAIMER

The contents of this report reflect the views of the authors, who are responsible for the facts and the accuracy of the data presented herein. The contents do not necessarily reflect the official views or policies of the US Department of Transportation or the Federal Highway Administration. This report does not constitute a standard, specification, or regulation.

This report and the accompanying design software (Drag_Pile) were prepared for use by the State Departments of Transportation, federal agencies and consulting firms technical staff. Neither the National Center for Transportation, Infrastructure Durability & Life-Extension (TriDurLE) nor the Principal Investigator warrants the report, the software, and results to be free of defects.

FORWARD

This report and the accompanying computer code (Software, Drag_Pile) describe the mobilized response analysis of piles under axial loads with the consideration of downdrag forces caused by the settlement of inundated collapsible soil layer(s). Pile foundations in collapsible soils may experience a sudden increase in the axial load (i.e., negative skin friction) due to the inundation of the surrounding soils, which may lead to significant reduction in the pile capacity and excessive pile settlement. A soil-pile model is developed to determine the downdrag force (negative skin friction) acting on the pile and pile settlement due to the inundation of the collapsible soil layer(s) in the vicinity of the pile foundations. The established pile downdrag force-settlement model depends on the variation in the collapsible soil properties due to inundation. Large number of collapsible sand and sandy silt soils (pre- and post-inundation) are used to develop a soil model that allows the assessment of the soil's collapse potential (Cp) (i.e., soil settlement), post-collapse friction angle and unit weight based on pre-inundation soil properties (such as initial void ratio, saturation and friction angle). The developed collapsible soil model is integrated into a mobilized soil-pile model to account for the settlement of soil layer(s) around the pile and induced downdrag force combined with the external loads at the pile head. Therefore, the presented technique couples the soil and pile settlement profiles with the pile-mobilized skin friction and end-bearing resistance in an interactive model to determine the downdrag force and load distribution along the pile length, and the location of the neutral plane. The load transfer (t–z and q–z) models employed in the current technique are constructed based on soil and pile properties, soil–pile interaction, and a constitutive soil model. Therefore, the presented technique couples soil and pile settlement profiles with the pile-mobilized skin friction and end-bearing resistance in an interactive fashion to determine the negative skin friction/downdrag load distribution along the pile length, and the associating pile settlement. The variation of the neutral plane location with the increase of pile-head load up to the pile's geotechnical limit can be also detected. The proposed procedure is compiled into a computer code with a friendly input/output graphical user interface. The developed interactive soil-pile model is validated based on field tests. However, very limited case studies or field/lab tests have been conducted to investigate the case of negative skin friction on piles caused by the inundation of the surrounding collapsible soils.

Table of Contents

Chapter 1. Introduction 1-10

1.1 Problem statement 1-10

1.2 Proposed models 1-12

1.2.1 Pile head load-settlement model 1-12

1.2.2 Post-Inundation properties of collapsible soils 1-12

1.2.3 Downdrag and drag loads 1-12

1.3 Objectives 1-13

1.4 Report overview 1-13

Chapter 2. Collapse potential and behavior of inundated collapsible soils 2-18

2.1 Introduction 2-18

2.2 Prediction of collapse potential based on experimental data 2-21

2.2.1 Soil properties/parameters influencing the soil collapse potential 2-22

2.3 Shear strength and stress-strain relationship of inundated collapsible soil 2-25

2.4 Effect of initial soil parameters on the behavior of inundated soil 2-26

2.5 Validation 2-28

2.6 Conclusions 2-30

Chapter 3. Pile side and tip response in sandy soil 3-1

3.1 Introduction 3-1

3.1.1 Side Resistance (Load Transfer–Settlement Model, t-z, of Sands) 3-2

3.2 Pile tip (point) resistance and settlement ($Q_p - z_p$) in sand 3-3

3.3 Pile tip settlement 3-5

Chapter 4. Pile side and tip response in clay soil 4-1

4.1 Introduction 4-1

4.2 Methodology 4-1

4.3 Pile side shear resistance in clay 4-2

4.4 Pile tip resistance and settlement 4-4

4.5 (t-z) curve assessment procedure 4-6

Chapter 5. Downdrag analysis procedures and validation 5-1

5.1 Introduction 5-1
5.2 FHWA 2016 method 5-1
5.2.1 FHWA 2016 step-by-step procedure (Hannigan et al., 2016) 5-1
5.3 Developed downdrag model 5-4
5.3.1 Downdrag and load distribution assessment procedure 5-5
5.3.2 Case Studies for Comparison and Validation 5-7
5.3.3 Full Scale Pile Test at Nikopol Region [Grigorian 1997] 5-7
5.3.4 Full Scale Pile Test at Volgodon Region [Grigorian 1997] 5-8
Chapter 6. References 6-2

List of Tables

Table 2-1. Effect of confining pressure (σ_3) on the properties of inundated collapsible soil. .. 2-27

Table 2-2. Effect of initial void ratio on the properties of inundated collapsible soil. 2-28

Table 2-3. Effect of initial degree of saturation on the properties of inundated collapsible soil. . 2-28

Table 2-4. Initial soil properties, as reported by Rinaldi and Capdevila (2006). 2-29

Table 2-5. Soil properties employed in the proposed model..... 2-29

Table 2-6. Initial soil properties of the intact specimens as reported by Haeri et al. (2019). ... 2-30

Table 2-7. Soil properties employed in the proposed model..... 2-30

Table 5-1. Soil profile and properties at Nikopol test site (Noor et al. 2013 after Grigorian, 1997). 5-8

Table 5-2. Predicted and measured pile drag force and pile-head settlement for the Nikopol test. 5-8

Table 5-3. Soil profile and properties at Volgodon test site (Noor et al. 2013 after Grigorian 1997). 5-9

Table 5-4. Soil properties at the Volgodon region. 5-9

List of Figures

Fig. 1-1. The United States collapsible soil map after Dudley (1970). 1-15
Fig. 1-2. Illustrates different soil conditions that can lead to drag forces. 1-16
Fig. 1-3. FHWA/Pioneering work of Fellenius' method for the calculation of the downdrag force on piles induced by the soil consolidation settlement based on ultimate downdrag and pile resistance force distribution. 1-17
Fig. 2-1. Typical bonding structures of collapsible soils (Clemence and Finbarr 1981)..... 2-32
Fig. 2-2. Sudden volume change of inundated collapsible soils (El-Howayek et al., 2011). 2-33
Fig. 2-3. F.G. Bell, in Encyclopedia of Geology (2005). 2-34
Fig. 2-4. Relationship of the collapse potential versus initial void ratio and dry unit weight... 2-35
Fig. 2-5. Relationship between the collapse potential and the initial degree of saturation. 2-36
Fig. 2-6. Predictions of the proposed model versus experimental data of inundated collapsible soils. 2-37
Fig. 2-7. Predictions of Eqs. 3 and 4 versus experimental data of inundated collapsible soils. 2-38
Fig. 2-8. Correlations of strength characteristics for granular soils after NAVFAC (1986). 2-39
Fig. 2-9. Soil constitutive model after (Norris, 1986; Ashour et al., 2019)..... 2-40
Fig. 2-10. Relationship between (ε_{50}), uniformity coefficient (C_u) and void ratio (e) after Norris (1986)..... 2-41
Fig. 2-11. Effect of confining pressure (σ_3) on the behavior of inundated collapsible soil as obtained from a conventional triaxial test..... 2-42
Fig. 2-12. Effect of initial void ratio on the behavior of inundated collapsible soil..... 2-43
Fig. 2-13. Effect of soil saturation on the behavior inundated collapsible soil. 2-44
Fig. 2-14. Comparison between predicted and measured stress-strain curves. 2-45
Fig. 2-15. Comparison between predicted and measured stress-strain curves. 2-46
Fig. 3-1. Axially loaded pile-soil model. 3-7
Fig. 3-2. Variation of displacement and shear stress with radial distance..... 3-8
Fig. 3-3. Progress of shear stress τ_0 at the soil-pile interface. 3-9
Fig. 3-4. Soil constitutive model (after Ashour et al., 2019 and Norris, 1986). 3-10
Fig. 3-5. Degradation in the secant friction angles of circles tangent to a curvilinear envelope of sand due to the increase in the confining pressure (Elfass, 2001). 3-11

Fig. 3-6. Changes of Friction Angle (ϕ) with the Confining Pressure (Ashour et al., 2004) 3-12
Fig. 3-7. Strain profile and the associated mobilized stresses immediately below the pile tip (after Elfass, 2001) 3-13
Fig. 4-1. Clay-pile adhesion based on pile materials and clay. 4-9
Fig. 4-2. Soil layer deformations around an axially loaded pile. 4-10
Fig. 4-3. Idealized relationship between shear strain in soil and pile displacement, Norris (1986). 4-11
Fig. 4-4. Soil modeling at the soil-pile interface. 4-12
Fig. 4-5. Normal and shear stress-strain relationship in soil and the associated Young's and shear modulus. 4-13
Fig. 4-6. Relationship of ε_{50} vs. Su (After Evans and Duncan 1982). 4-14
Fig. 4-7. Strain profile and the associated mobilized stresses immediately below the pile tip (After Elfass et al., 2008). 4-15
Fig. 5-1. Plot of static analysis results (after Siegel et al., 2013). 5-10
Fig. 5-2. Plot of normalized toe resistance versus toe movement (after Siegel et al. 2013). 5-11
Fig. 5-3. Axial load and resistance plot cumulative shaft resistance vs. depth (after Siegel et al., 2013). 5-12
Fig. 5-4. Axial load and resistance plot of unfactored permanent load plus cumulative shaft resistance vs. depth (after Siegel et al., 2013)..... 5-13
Fig. 5-5. Axial load and resistance plot, including mobilized resistances (after Siegel et al., 2013). 5-14
Fig. 5-6. Axial Load and resistance plot, including neutral plane location based on mobilized toe resistance (after Siegel et al., 2013). 5-15
Fig. 5-7. Soil-pile modeling in sublayers and segments with a set of t-z and q-z springs..... 5-16
Fig. 5-8. Pile and soil settlement profiles coupled with pile side/toe load-displacement relationships to capture the mobilized response of a pile subjected to negative skin friction... 5-17
Fig. 5-9. Flowchart for the implemented procedure of downdrag force/settlement acting on a pile embedded into inundated collapsible soil(s). 5-18
Fig. 5-10. (a) Predicted values of Cp over the depth at Nikopol Test (b) Predicted soil and pile settlement of inundated soil at Nikopol Test. 5-19
Fig. 5-11. Downdrag and resistance force along the pile at Nikopol test. 5-20

Fig. 5-12. Saturation drain holes and soil profile at Volgodon Region (Grigorian, 1997 and Noor et al., 2013). 5-21
Fig. 5-13. Soil and pile settlement profiles for a 43-m long pile test in Tokyo, Japan..... 5-22
Fig. 5-14. (a) Predicted values of Cp over the depth settlement of inundated soil at Volgodon Test (b) Predicted soil and pile of inundated soil at Volgodon Test..... 5-1

Chapter 1. Introduction

1.1 Problem statement

Collapsible soils or metastable soils are unsaturated soils that experience a substantial volume reduction upon saturation with or without additional load. Such soils maintain an open ‘‘honeycombed’’ structure that could have cementing agents that produce considerable shear strength. In addition to a substantial soil settlement, the inundation of collapsible soil also causes a significant change in its shear strength. Collapsible soils constitute a major area of concern in geotechnical engineering due to the significant human and economic losses accompanying the damages to structures, roads, and bridges induced by their collapse. Considerable collapsible soils' formations have been reported in many of the United States (e.g., Louisiana (Thornton 1972), California (Knodel 1992), Colorado (White 2006), Arizona (Houston et al., 2001), Nevada (Roullier 1992), Indiana (El-Howayek et al., 2011), New Mexico (Lommler and Bandini 2015), and Utah (Owens and Rollins 1990). etc.) as shown in Fig. 1-1.

Piles seem to be the favorable foundation option whenever collapsible soils are encountered. Qian et al. (2014), Kalashinkova (1976), and Grigorian and Ivanov (1975) conducted full-scale field tests on axially loaded piles in collapsible soils and marked a considerable reduction in the pile capacity due to inundation. Abid-Awn and Hussain (2017) and Mashhour and Hanna (2016) conducted lab tests to investigate axially loaded piles embedded in collapsible soil. Mashhour and Hanna (2016) observed that negative skin friction on the tested pile increased with the increase in the soil collapse potential (Cp). Noor et al. (2013) and Zaretskii and Karabaev (1987) presented numerical models that incorporate the effects of collapsible soils inundation and the associated negative skin friction on vertical piles subjected to compression loads. However, research concerned with modeling the behavior of piles embedded in collapsible soils analytically has been quite lagging (Mashhour and Hanna 2016). To develop an analytical model that determines the response of piles embedded in collapsible soils under developing downdrag forces acting on piles after soil inundation, the inundated collapsible soil's behavior and interaction between the pile and adjacent soil layers need to be evaluated.

Numerous efforts have been made to study the relationships between the collapsible soil's initial properties and its collapse potential through laboratory and field tests. The collapsible soil's initial saturation ratio (Sr) is probably the most influential parameter on its Cp severity. Roullier et al. (1992), Williams and Rollins (1991), and Basma and Tuncer (1992) indicated that soils with lower values of dry densities exhibit larger deformations due to collapse than soils with higher dry densities.

It should be noted that the downdrag force could develop any time during the bridge life, which results in an additional (i.e., damaging) axial load on the pile foundation. Therefore, the anticipated downdrag force caused by the inundation of collapsible soils should be accounted for in the design of the pile foundation to improve the durability and serviceability and to extend the life of the bridge. The downdrag force could be triggered by excessive soil settlement through different scenarios caused by 1) consolidation of clay soil layers under fill; 2) inundation of collapsible soils; and 3) soil liquefaction (Fig. 1-2). AASHTO LRFD Bridge Design Specifications (2016) recommends the use of the FHWA (2016)/ Fellenius' method for the calculation of the downdrag force on piles induced by soil deposit settlement associated to any of the above-mentioned scenarios (Fig. 1-3).

The current study targets the evaluation of the downdrag force/negative skin friction acting on the pile as induced by the settlement of inundated collapsible soils. In order to tackle this problem, the amount of settlement that the collapsible soil layer experiences due to the inundation should be estimated. In addition, the post-inundation soil characterization (i.e., change in soil properties such as unit weight, relative density, friction angle) should be evaluated. Such collapsible soil modeling and characterization rely on collecting large amount of related database from the literature. Please notice that the negative skin friction acting on the pile skin will be calculated in this study based on the relative pile-soil displacement and developing pile-soil shear stress along the pile (Fig. 1-3), which is a more realistic mechanism/technique compared to the current practice (FHWA/AASHTO) that only depends on pile-soil shear strength.

1.2 Proposed models

1.2.1 Pile head load-settlement model

There are several methods to calculate the ultimate axial capacity of piles. The developed model enables the program Drag_Pile to calculate and plot the full pile head load-displacement curve under compression loads with/without downdrag forces. The presented technique is based on soil-pile interaction (i.e., t-z nonlinear model) and utilizes the basic properties of soils and pile. Moreover, to assure a sort of consistency, the developed mobilized pile response model utilizes basic soil properties (unit weight γ, angle of internal friction φ, and cohesion C) as input data used for determining the pile axial response. The employed pile head load-displacement assessment procedure adopts t-z curves developed by Ashour and Abbas (2019); Ashour and Helal (2017); and Ashour et al. (2010), and the q-z curves developed by Elfass (2001) and Elfass et al. (2009).

1.2.2 Post-Inundation properties of collapsible soils

The current study presents a correlation/equation that allows the prediction of the collapse potential (Cp) of collapsible soils and accompanying volume change (settlement. Δe) of soil, as a result of soil inundation. The desired correlation is function of the pre-inundation/initial soil properties (such as initial void ratio, e_o, saturation ratio, S_{ro}, and overburden pressure, σ_3). Large number of tested samples of collapsible soils have been used to develop the targeted correlation. It should be noted that the current study is concerned with collapsible soils predominantly comprised of silts and sands.

1.2.3 Downdrag and drag loads

As addressed in AASHTO 2014, downdrag occurs when the soil settlement along the side of the pile results in a downward movement of the pile surrounding soil relative to the pile. In the case of frictional piles with limited tip resistance, the downdrag load can exceed the geotechnical resistance of the pile, causing the pile to move down enough to allow service limit state criteria for the structure to be exceeded. As a result, service limit state tolerances will govern the geotechnical design. Therefore, designers need to estimate the developing scenario of downdrag force and associated settlement regardless of the causing scenario (fill placement, soil liquefaction or inundation of collapsible soils). Hannigan et al. (2016) classify the drag force and the downdrag as structural strength and geotechnical serviceability limit states problems,

respectively. However, Hannigan et al. (2016) did not consider the profile of soil settlement in the evaluation of the neutral plane location. Additionally, the mobilized toe resistance associated with a given permanent pile-head load and drag force is assumed using curves for normalized pile-toe resistance versus movement for guidance.

The developed model employs a load-settlement mechanism that allows the calculation of the soil displacement relative to pile settlement. Therefore, negative skin shear stresses acting downward along the pile side (i.e., downdrag force) due to the settlement of surrounding soil layers can be estimated and accounted for in the analysis of axially loaded piles.

1.3 Objectives

The main objective of this study is to predict the pile head load-displacement curve for piles subjected to axial compression forces and embedded into multilayer soil profiles with collapsible soil layer(s) that might be inundated (i.e., subjected to downdrag force). The negative skin friction (i.e., downdrag) acting on piles as induced by the settlement of inundated collapsible soil is evaluated based on the initial properties of collapsible soils. An empirical model/correlation based on experimental data is also established to evaluate the collapse potential of soil and its post-inundation properties as a function of the initial properties of this collapsible soil. The study also addresses the current method suggested by the FHWA 2016 (Hannigan et al., 2016) for the assessment of the pile response when subjected to drag forces. The designer can evaluate the pile settlement/serviceability caused by superstructure axial load and additional unexpected axial forces (drag force) that could have a damaging impact on pile foundations and the superstructure if neglected or underestimated. The developed model is compiled into a software package with input/output friendly graphics user interface.

1.4 Report overview

The presented report comprises chapters that includes developed soil and soil-pile models to assess the collapse potential of inundated collapsible soils, developing negative skin friction (i.e., down drag force acting on the pile, and the pile response (load-settlement curve of axially loaded pile with the consideration of down drag force. Chapter 1 presents an introduction to the current study and a description of the problem statement and targeted objectives. Chapter 2 presents an empirical correlation for the prediction of collapse potential of inundated collapsible soil using experimental data from a broad range of soil specimens that vary from sandy, silty

sand, sandy silt, to silt. Chapters 3 and 4 present the load transfer mechanism of piles embedded in sand and clay soils subjected to compression loading. Chapter 5 presents a summary on the FHWA (2016) method for the analysis of piles subjected to downdrag and a detailed description of the new technique that couples the soil and pile settlement profiles with the pile mobilized skin-friction and end-bearing in an interactive model to determine the downdrag (pile settlement), load distribution along the pile length, and location of the neutral plane. Chapter 5 also presents case studies and validation/implementation of the developed technique. The developed technique is compiled in a software package with a user manual which are submitted separately with this final report.

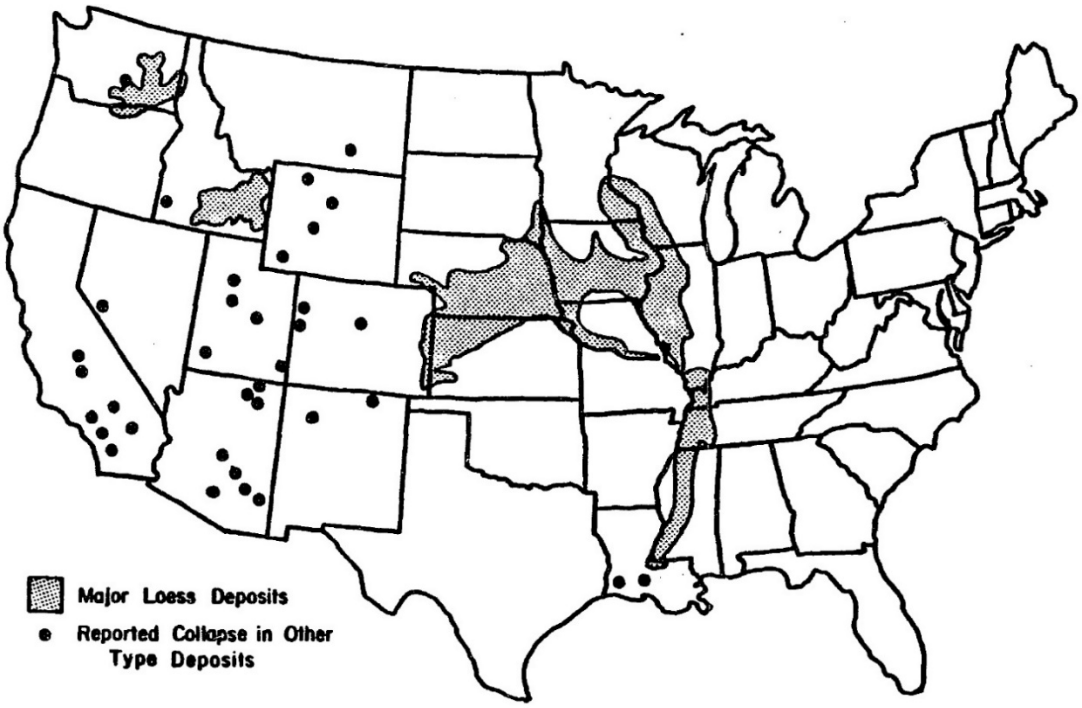

Fig. 1-1. The United States collapsible soil map after Dudley (1970).

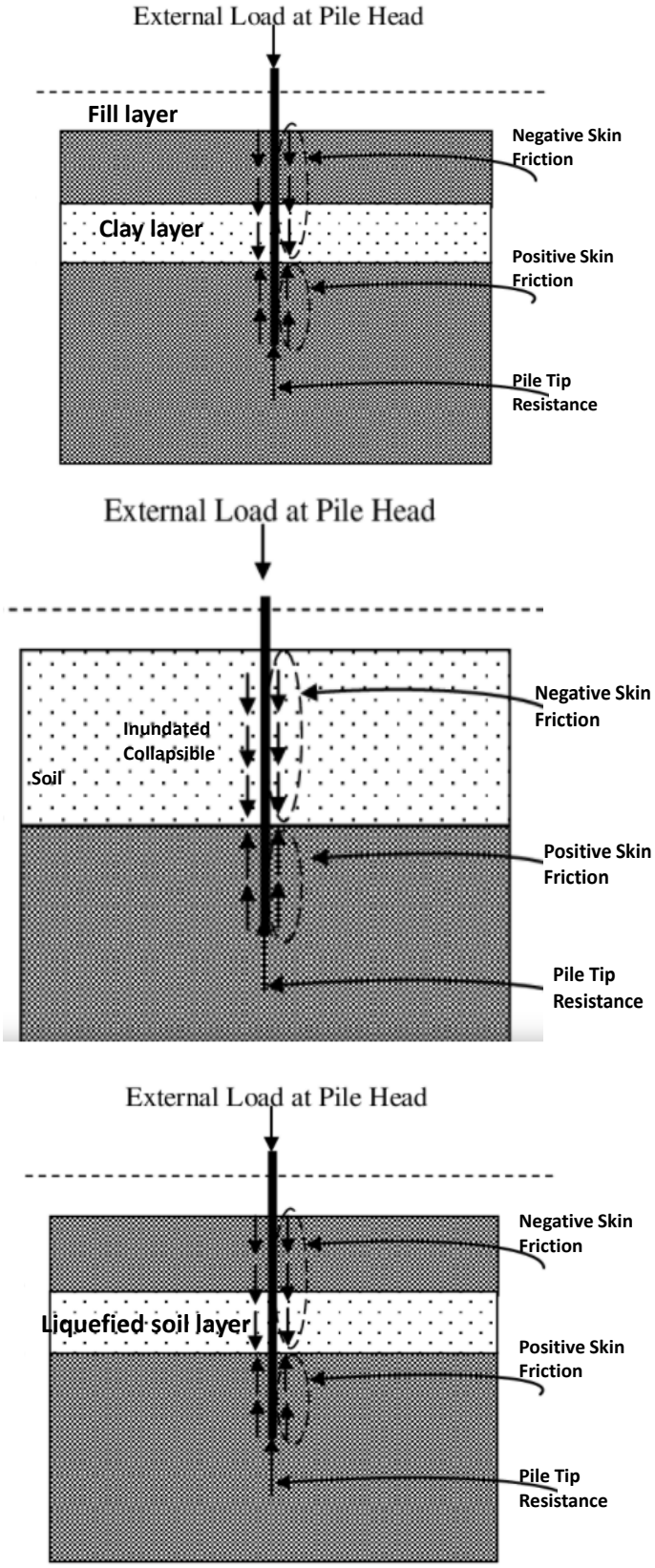

Fig. 1-2. Illustrates different soil conditions that can lead to drag forces.

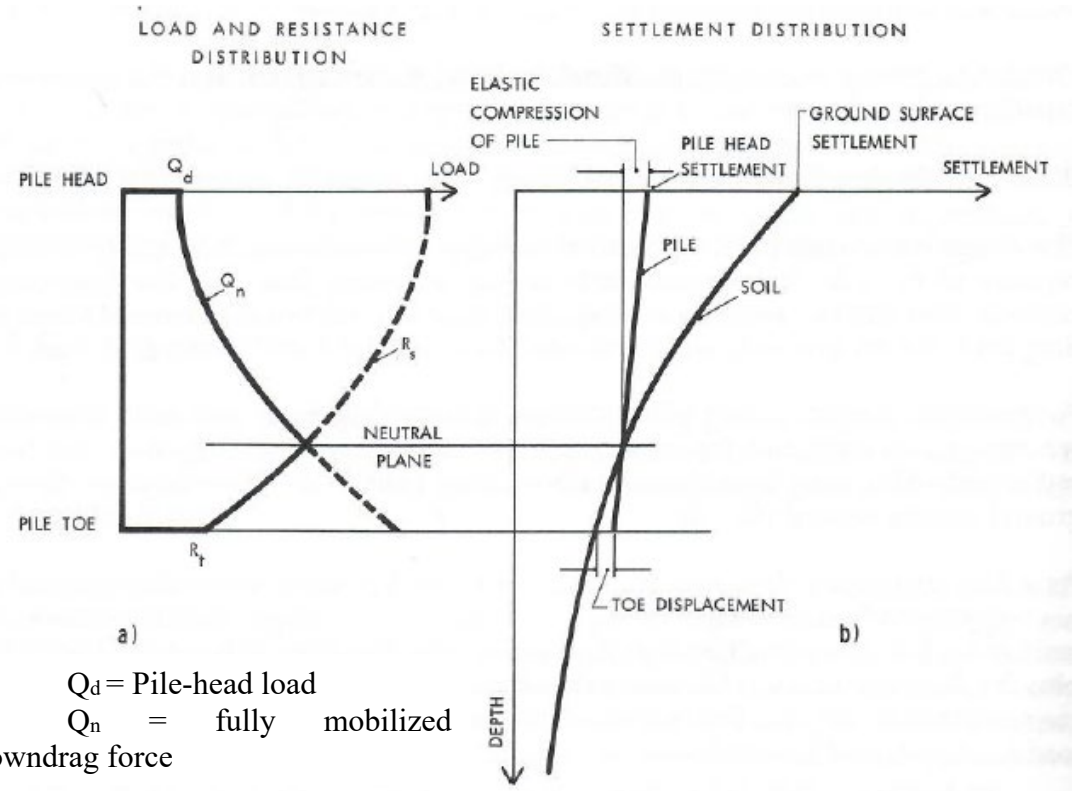

Fig. 1-3. FHWA/Pioneering work of Fellenius' method for the calculation of the downdrag force on piles induced by the soil consolidation settlement based on ultimate downdrag and pile resistance force distribution.

Chapter 2. Collapse potential and behavior of inundated collapsible soils

2.1 Introduction

Collapsible soils or metastable soils are soils with a loose structure; a large void ratio; and a water content much lower than saturation. Soil grains are usually coated by clays and/or silt, the bonding can be provided by aggregated clay/silt grains (Fig. 2-1). Generally, collapsible soils maintain an open ‘‘honeycombed’’ (Fig. 2-1). However, the water dissolves or softens the bonds between the particles, causing soil collapse and a denser particle packing. Therefore, collapsible soils undergo a significant volume reduction upon saturation/inundation with or without additional load (Fig. 2-2). It should be emphasized that this study focuses on collapsible soils dominated by sand and silt grains (i.e., sandy, silty sand and silty soils) (Fig. 2-3).

There are different laboratory and field methods that measure the collapse potential (Cp) of soils. The most common practice to measure the collapse potential is by conducting laboratory tests using either the oedometer test or the triaxial test. Medero et al. (2009) suggested a sample preparation technique to produce a metastable collapsible soil, which was then used to investigate soil collapsibility. Medero et al. (2009) observed that, for the same initial conditions, samples tested using the single oedometer test resulted in higher collapse potential than samples tested using the double oedometer test. On the other hand, Haeri et al. (2016) performed triaxial tests on intact and reconstituted collapsible soil specimens to identify the effect of specimen disturbance and structure on the behavior of collapsible soil. Haeri et al. (2016) observed volumetric strain values for the intact soil specimens higher than those of the reconstituted specimens, especially under low mean net stress. Furthermore, the reconstituted soil specimens demonstrated strain softening, dilatancy at failure, and exhibited higher shear strength when

compared to the intact soil specimens, which displayed highly contractive behavior. The observations of Haeri et al. (2016) indicate that the results obtained from reconstituted soil specimens might lead to overestimation of shear strength and underestimation of the volume change induced by the collapse. Rinaldi and Capdevila (2006) examined the stress-strain behavior of collapsible soils by conducting triaxial tests on disturbed and undisturbed collapsible soil samples and concluded that confining pressure and water content are the predominant parameters that affected the yielding stress, shear strength and volume change of the tested samples during loading.

Vilar and Davies (2002) studied the collapse behavior of clayey sand using the suction controlled oedometer test and the triaxial compression test. The collapse deformations observed in the oedometer tests were more significant than those measured in the triaxial compression tests, which may be attributed to the influence of the lateral deformations on the collapse magnitude Vilar and Davies (2002). Lloret and Alonso (1980) used the finite element method coupled with a finite difference scheme to model the volume change behavior of unsaturated soils based on air and water continuity equations. Lloret and Alonso (1980) also developed a method to calculate the water and air pressures caused by undrained loading. Khalili et al. (2004) conducted triaxial and oedometer saturated and unsaturated tests in addition to analyzing several tests' results obtained from the literature and suggested that the effective stress principle is applicable in the prediction of the unsaturated soil's shear strength and volume change.

Delage et al. (2013) examined the collapse susceptibility of some loess deposits, which were especially sensitive to the changes in the water content, in the light of their microstructure composition. Based on simple and double oedometer tests performed on four intact samples, Delage et al. (2013) reported that the collapse potential is significantly sensitive to the changes in

the water content, as the collapse volume was reduced by more than 5% when the water content was smaller than 12 %. Additionally, Delage et al. (2013) reported that the collapsible soil in some areas was composed of a porous microstructure with a heterogeneous scattering of clay filling the inter-grains pores, which behaved as a linking agent between the grains.

Habibagahi and Taherian (2004) experimented with three collapsible soil types with different initial conditions obtained from a site in Seavand, Iran. A series of 192 single oedometer tests were conducted in which the soil samples were inundated at different applied pressures. Habibagahi and Taherian (2004) proposed the use of three types of neural networks to predict the collapse potential based on the initial collapsible soil properties. Basma and Tuncer (1992) investigated the effect of compaction water content, initial dry unit weight, applied pressure at wetting and soil type on the collapse potential by conducting 138 single oedometer tests on eight different soil types obtained from different locations in Jordan. Basma and Tuncer (1992) proposed a method to estimate the water content after which no collapse takes place (i.e., critical water content). Furthermore, a nomograph was suggested by Basma and Tuncer (1992) to predict the collapse potential based on the pressure at wetting, coefficient of uniformity, dry unit weight, and the critical water content. Qian et al. (2014) conducted a series of laboratory tests on nine groups, each composed of three undisturbed collapsible soil specimens to study the hydro-collapsibility and characteristics of loess in Northwest China. Qian et al. (2014) concluded that the collapse potential decreases with increasing initial density and moisture content.

Based on laboratory and field investigations, Milovic (1988) observed that loess subsidence due to wetting depends to a large extent on dry density, water content, and stress level acting during saturation. Milovic (1988) examined the impact of loess sample disturbance on laboratory results and reported that loess specimens were susceptible to mechanical

disturbance, which leads to misguiding (unsafe) laboratory results. Roullier (1992) examined a database of collapsible soil tests and also observed that the water content and dry density of soil have the most significant weight/effect on the soil collapsibility. Additionally, Roullier (1992) used discriminant analysis to predict the soil probability of being collapsible or non-collapsible based on dry density, water content, and soil classification. Finally, Roullier (1992) recommended that different collapse potential prediction models be derived for different regions.

Because of the significant effect of soil inundation on the properties and behavior of collapsible soil, the inundation effect needs to be considered in the foundation design. Some representative correlations to assess the variation in the basic soil properties of collapsible soils due to inundation could be valuable to reduce the need for performing collapse tests either in the laboratory or in-situ. To develop correlations between the collapse potential and the variation in basic soil properties, a database of a substantial number of tests was collected from various research to provide a model that predicts the collapsible soil's shear strength and stress-strain relationship after full inundation (i.e., after collapse). The prediction of the post-inundation collapsible soil properties and associated stress-strain relationship enhance the design and behavior analysis of foundations (e.g., deep foundations).

2.2 Prediction of collapse potential based on experimental data

The collapse potential (Cp) is the collapse strain value due to the inundation of an undisturbed sample under 200 kPa pressure as tested in the oedometer apparatus and calculated using Eq. 2-1 (ASTM 2004).

$$C_P = \frac{\Delta e \times 100}{1+e_0} = \frac{\Delta H \times 100}{H_0} \quad (2\text{-}1)$$

Where, Δe and ΔH are the change in the sample's void ratio and height due to inundation, respectively. E_0 and H_0 are the sample's initial (i.e., pre-inundation) void ratio and initial height, respectively.

The collapse potential prediction model is developed by, first, selecting the high-quality tests from the gathered database then; identifying the soil properties that influence the collapse potential and lastly; utilizing the database in a multiple regression analysis with transforms where the independent variables are the identified soil properties and, the dependent one is the collapse potential.

The current study is concerned with collapsible soils predominantly comprised of sands and silts. Different testing techniques yield different Cp results, even if the tests were conducted on the same soil. Even though a large database containing more than one thousand tests was assembled from various geotechnical reports and research papers, most of the tests were excluded because either the tests were conducted on disturbed samples or due to the insufficiency of reported soil properties. Habibagahi and Taherian (2004), Basma and Tuncer (1992), and Qian et al. (2014) reported results for 339 single oedometer tests conducted on undisturbed samples of different types of collapsible soils with sufficient initial soil properties. Therefore, those 339 tests are the only tests considered in the current analysis (see Table ------for collected soil sample data) .

2.2.1 Soil properties/parameters influencing the soil collapse potential

Soils with higher values of void ratio and lower values of dry densities typically exhibit larger deformations due to collapse (Basma and Tuncer 1992; Roullier 1992; Williams and Rollins 1991). Figures 2-4a and 2-4b show the collapse potential relationships with the soil's

initial void ratio and dry density, respectively. While there is a considerable scatter in the data presented in Fig. 2-4, it's evident that the collapse potential is directly proportional to the value of the soil's initial void ratio (e_0) and inversely proportional to the initial value of the soil's dry unit weight (γ_d). The effect of the initial void ratio on the collapse potential is considered in the proposed model as it generates a slightly higher correlation coefficient with the collapse potential compared to the initial dry unit weight. However, using e_0 alone as an indication of collapse would be rather a crude approach due to the wide range of e_0 values exhibiting significant collapse, as indicated by the scatter in the data presented in Fig. 2-4.

The initial degree of saturation (S_{ro}) is probably the most significant parameter in determining the soil's susceptibility to collapse. The collapse potential decreases with the increase in initial water content and soil saturation (El-Howayek et al., 2011; Choudhury and Bharat 2018; Lawton et al., 1989). In fact, Booth (1977) and Basma and Tuncer (1992) suggested that soils with a degree of saturation larger than the critical value are not prone to collapse. Figure 2-5 depicts the variation of the collapse potential with the degree of saturation. However, it can be noticed that the collapse potential of soil almost diminishes beyond S_{ro} of 60%. Similar to the initial void ratio, there is a notable correlation between the collapse potential and degree of saturation. Nevertheless, it can't be used solely as a measure of collapse potential.

The collapse potential increases with the increase in consolidation pressure (Basma and Tuncer 1992; Lawton et al., 1989; Reginatto and Ferrero 1973). Popescu (1986) noted that the collapse potential increases considerably with pressure beyond a specific pressure value (i.e., collapse pressure). It's noteworthy that the collapse pressure can't be considered the same as the pre-consolidation pressure as it varies with the degree of saturation Reginatto and Ferrero (1973). The curves reported by (Haeri et al., 2019; Williams and Rollins, 1991; Booth, 1977) describing

the relationship between the collapse potential and pressure indicate that beyond a small pressure value, the collapse potential increases linearly with the logarithm of pressure until it reaches some maximum value then decreases again. Booth (1977) and Basma and Tuncer (1992) reported that the collapse potential is affected by the particle size distribution and soil type. However, Booth (1977) noted that the effect of soil grading and mineralogy on the amount of collapse is complicated and less significant when compared to the impact of initial dry density.

In light of the above, the initial soil properties employed in the multiple regression analysis are the void ratio (e_o), degree of saturation (S_{ro}), applied (overburden) pressure (σ_3), and the coefficient of uniformity (Cu). The result of the regression analysis is given in Eq. 2-2, and the prediction of the results based on the obtained equation is shown in Fig. 2-6.

$$C_p = [-15 + 1.355 \ln \sigma_3 + 16.156\, e_0 + 21.366\, e^{-5.5\, S_{ro}} + 0.00088\, Cu^2] * \left[1 - \frac{Sro}{100}\right]^{0.5} \left[\frac{\sigma_3}{200}\right]^{0.1} \quad C_p \geq 0 \qquad (2\text{-}2)$$

Where σ_3 in kPa and S_{ro} in percent. Basma and Tuncer (1992) proposed Eqs. 2-3 and 2-4 for collapse potential prediction. Figures 2-7a and 2-7b show the predictions of Eqs. 2-3 and 2-4. It can be seen from Figs. 2-6 and 2-7 that the proposed equation gives better predictions and less scatter compared to Eqs. 2-3 and 2-4 with a coefficient of correlation (R^2) value of 0.81 compared to R^2 values of 0.75 and 0.68 for Eqs. 2-3 and 2-4, respectively.

$$C_p = 48.496 + 0.102\, Cu + 0.457\, w_i - 3.533\, \gamma_d + 2.80 \ln \sigma_3 \qquad (2\text{-}3)$$

$$C_p = 47.506 - 0.072\, (s - c) - 0.439\, w_i - 3.123\, \gamma_d + 2.851 \ln \sigma_3 \qquad (2\text{-}4)$$

Where (s - c) is the difference between the sand and clay percentages and w_i is the soil's initial water content.

2.3 Shear strength and stress-strain relationship of inundated collapsible soil

The proposed collapse potential equation (Eq. 2-2) is developed based on single Oedometer tests' data and is used to calculate the inundated void ratio ($e_{inundated}$) via Eq.2-5. $e_{inundated}$ along with some initial soil properties, are then utilized to assess the new properties of the soil after collapse. It should be emphasized that the newly obtained post-inundation soil properties are then used to predict the stress-strain behavior of inundated soil as obtained from a conventional triaxial test performed on the inundated collapsible soil specimen.

$$e_{inundated} = e_0 - \frac{C_p*(1+e_0)}{100} \quad (2\text{-}5)$$

After full inundation of collapsible soil, the cementing bonds between particles get broken, and the remaining shear strength is derived from the intergranular frictional forces. Consequently, the angle of internal friction can be utilized as an adequate measure of shear strength. The friction angle (ϕ) can be determined using the soil classification and $e_{inundated}$ through the correlation presented in Fig. 2-8 (NAVFAC, 1986). It should be mentioned that the current study is concerned only with the hatched zone shown in Fig. 2-8.

Norris (1986) and then Ashour et al. (2019) developed a stress-strain relationship based on triaxial test results conducted on a large number of different samples of sandy soils (Fig. 2-9). The stress level (SL) is calculated using Eq. 2-7, and λ is a fitting parameter for the stress-strain exponential relationship shown in Fig. 2-9. In this relationship (Fig. 2-9), the soil strain at 50% stress level (ε_{50}) and SL are required input parameters to build the soil full stress-strain curve up to failure. ε_{50} varies with soil type and confining pressure and can be obtained from a conventional drained triaxial test in which the confining pressure (σ_3) is set equal to the desired

overburden pressure. Alternatively, ε_{50} can be assessed using its correlation with Cu and e (Norris, 1986) (Fig. 2-10). The curves shown in Fig. 2-10 were developed from CD tests at 42.5 kPa confining pressure and should be adjusted for other values of confining pressures using Eq. 2-6 (Norris, 1986). SL is the ratio of the deviatoric stress (σ_d) at any loading increment to the deviatoric stress at failure (σ_{df}) under the associating σ_3 value, as shown in Eqs. 2-7 and 2-8.

$$\varepsilon_{50} = (\varepsilon_{50})_{42.5} * \left(\frac{\sigma_3}{42.5}\right)^{0.2} \quad (2\text{-}6)$$

$$\text{SL} = \frac{\sigma_d}{\sigma_{df}} = \frac{2\tau}{\sigma_{df}} \quad (2\text{-}7)$$

$$\sigma_{df} = \sigma_3 * \left[\left(\tan\left(45 + {}^{\Phi}/_{2}\right)\right)^2 - 1\right] \quad (2\text{-}8)$$

2.4 Effect of initial soil parameters on the behavior of inundated soil

The majority of available research focuses on the effect of soil's initial properties on the collapse potential, and only a few research focuses on the impact of the change of soil properties on the collapsible soil inundated stress-strain behavior. Soil properties are interconnected; for instance, poorly-graded soils with low Cu values would typically have higher void ratios than well-graded soils with high Cu values. However, for the purpose of inspecting the impact of initial soil parameters on the stress-strain behavior of inundated collapsible soils, each parameter in Eq. 2-2 has been changed individually while all other parameters were held constant.

Table 2-1. Effect of confining pressure (σ_3) on the properties of inundated collapsible soil.

Initial				Inundated			
σ_3 (kPa)	e_0	Sr (%)	Cu	Cp	$e_{inundated}$	ϕ	$\varepsilon_{50} * 10^{-2}$
200	0.85	30	6	7.68	0.71	33.18	1.47
400				8.62	0.69	33.72	1.59
800				9.56	0.67	34.26	1.72
1200				10.11	0.66	34.58	1.79

The used values of confining pressure and their associating impact on the inundated soil parameters are given in Table 2-1. Figure 2-11 shows the stress-strain curves for four specimens of collapsible soils with four values of σ_3 applied during the soil inundation and then confined with σ_3 in the triaxial test. It can be inferred from Table 2-1 and Fig. 2-11 that higher values of confining pressure produce stiffer soil response. This stiffer soil response with higher σ_3 can be attributed to the increase in collapse potential leading to denser packing of soil particles after inundation, hence high frictional resistance, and friction angle. The combination of high ϕ and σ_3 derives the stiffer soil response with increasing σ_3 as illustrated in Fig. 2-11. It should be noted that the improvement in soil resistance with σ_3 agrees with the experimental findings of Rinaldi and Capdevila (2006).

The effect of changing the initial void ratio (i.e., density) on the inundated soil properties and stress-strain behavior of collapsible soils are given in Table 2-2 and Fig. 2-12, respectively. Although the collapse potential increases with the increase of e_0, the void ratio after full inundation ($e_{inundated}$) for soils with lower e_0 remains less than those with higher e_0, as seen in Table 2-2. Thus, soils with higher initial density and lower e_0 display higher ϕ values, and progress to greater deviatoric stresses than those with a lower initial density (Fig. 2-12).

Furthermore, lower $e_{inundated}$ values result in lower ε_{50} as deduced from Fig. 2-8 hence a stiffer soil behavior.

Table 2-2. Effect of initial void ratio on the properties of inundated collapsible soil.

Initial				Inundated			
e_0	σ_3 (kPa)	Sr (%)	Cu	Cp	$e_{inundated}$	ϕ	$\varepsilon_{50} * 10^{-2}$
0.7	200	30	6	5.26	0.61	36.21	1.02
0.85				7.68	0.71	33.18	1.47
1				10.11	0.8	30.38	1.97
1.15				12.53	0.88	27.8	2.51

Table 2-3 presents the employed values of the initial S_{ro} and their accompanying impact on the inundated soil properties. Figure 2-13 shows an almost 25% drop in soil resistance when S_{ro} increased from 10% to 30%, whereas negligible loss in strength is noticed when S_{ro} rose from 60% to 90%. This observation can be attributed to the exponential decay of Cp with S_{ro} (Eq. 2-2). In addition, the negligible difference in resistance between the cases where S_{ro} was equal to 60% and 90%, endorses the concept of critical water content (i.e., S_{ro}) advocated by Basma and Tuncer (1992) and Booth (1977)

Table 2-3. Effect of initial degree of saturation on the properties of inundated collapsible soil.

Initial				Inundated			
Sr (%)	σ_3 (kPa)	e_0	Cu	Cp	$e_{inundated}$	ϕ	$\varepsilon_{50} * 10^{-2}$
10	200	0.85	6	5.91	0.56	37.92	0.80
30				7.68	0.71	33.18	1.47
60				4.37	0.77	31.27	1.8
90				3.72	0.78	30.9	1.87

2.5 Validation

Rinaldi and Capdevila (2006) conducted an experimental investigation to address the impact of suction and cementation on the stress-strain behavior of loess. Consolidated drained triaxial tests were conducted on disturbed and undisturbed, saturated and unsaturated loess

samples interchangeably. The strains were measured in the triaxial test by means of three local displacement transducers placed on the specimen being tested. The initial soil properties reported by Rinaldi and Capdevila (2006) and the predicted soil properties using our suggested model are given in Tables 2-4 and 2-5, respectively. The soil samples were tested under different confining pressures of 10, 20, 40, and 80 kPa. Only the undisturbed saturated soil sample tested under confining pressure of 80 kPa was considered in the validation to ensure that all cementation effects were disrupted. Figure 2-14 shows a comparison between the measured stress-strain curve and the ones calculated using the bilinear model developed by Rinaldi and Capdevila (2006) and the proposed model. A better agreement with the measured data can be observed at the initial deviatoric stresses compared to the bilinear model.

Table 2-4. Initial soil properties, as reported by Rinaldi and Capdevila (2006).

USCS	w_0 (%)	PI	γ_d (kN/m^3)	Sr	Pass. No. 200 (%)
ML	18.0	3.6%	12.5	0.42	2.4 %

Table 2-5. Soil properties employed in the proposed model.

σ_3 (kPa)	ϕ (degrees)	ε_{50}
80	22	0.015

Haeri et al. (2019) conducted wetting-induced collapse and suction controlled triaxial tests on intact and reconstituted collapsible soil specimens using a modified triaxial test apparatus. The test procedure comprised four stages, namely equalization, isotropic compression,

wetting, and shearing. Sixteen drained triaxial tests were conducted in total, where the specimens were subjected to net stresses of 50, 200, and 400 kPa and a range of matric suctions. Only the stress-strain curves of undisturbed samples subjected to zero matric suction are used to validate the proposed model. Furthermore, Haeri et al. (2019) reported that the intact specimens tested at low net stress of 50 kPa displayed high shear resistance due to the presence of cementing bonds between the particles. The reported soil properties of the intact specimen and the soil properties predicted using the proposed model are given in Tables 2-6 and 2-7, respectively. Figure 2-15 shows a reasonable agreement between the measured and predicted stress-strain behavior of the specimens subjected to net stresses of 200 and 400 kPa.

Table 2-6. Initial soil properties of the intact specimens as reported by Haeri et al. (2019).

USCS	e_0	γ_d kN/m^3)	w_0 (%)	Sr	Pass No. 4, %	Pass No. 200 (%)	Clay frac. <2mm
ML	0.77	15.07	7.1	0.25	100	96.5	2 5.9

Table 2-7. Soil properties employed in the proposed model.

σ_3 (kPa)	ϕ (degrees)	ε_{50}
200	32	0.022
400	32	0.025

2.6 Conclusions

The established model allows the calculation of the collapse potential of sandy and silty collapsible soils due to inundation as a function of the soil's initial void ratio and degree of saturation, uniformity coefficient, and applied pressure. Compared to other correlations, the

presented model maintains a higher coefficient of correlation (R^2) value of 0.81. The study displays the influence of e_o, S_{ro}, σ_3, and Cu on the value of Cp due to soil inundation and the associating $e_{inundated}$, ϕ and ε_{50} where S_{ro} and e_o maintain larger effect on the resulting Cp compared to σ_3. Unlike the limited effect of Cu, it can be noticed that the larger the value of e_o and/or the smaller the values of S_{ro}, the larger the effect on Cp. On the other hand, the influence of S_{ro} on the Cp of inundated soils substantially decreases by the increase of S_{ro} and becomes almost negligible beyond S_{ro} = 60%

The drop in the collapsed soil's void ratio due to inundation produces new values for the soil's friction angle and ε_{50} which are reflected in the stress-strain curve of the collapsed soil. The utilized constitutive model employs the soil properties ($e_{inundated}$, ϕ, and ε_{50}) of inundated soil to predict the stress-strain curve for the soil (in its new state) as obtained from the conventional triaxial test. A significant effect for the variation of e_o, σ_3, and Sr can be observed on the stiffness of resulting stress-strain curves.

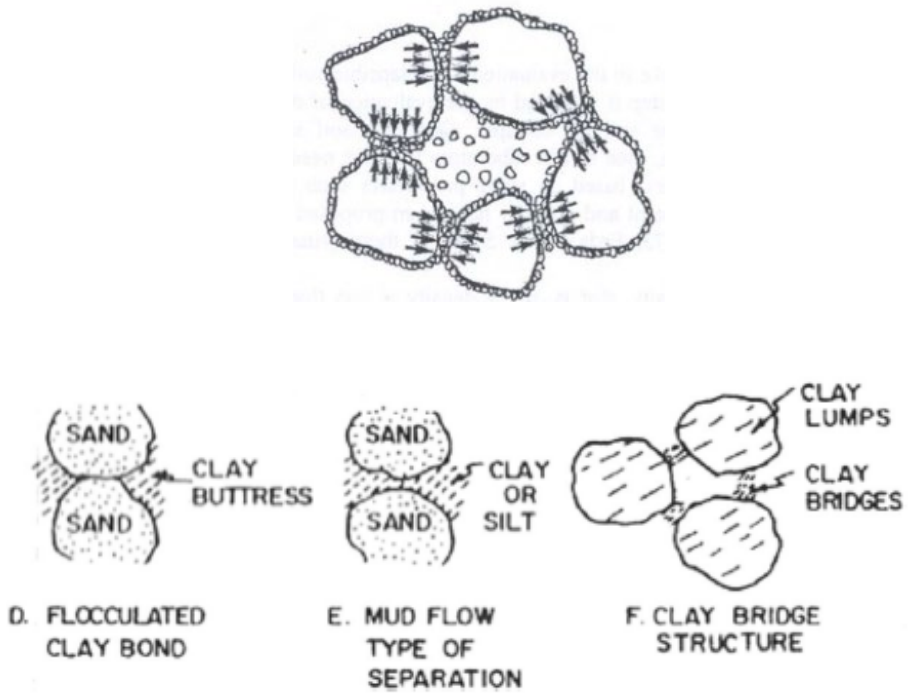

Fig. 2-1. Typical bonding structures of collapsible soils (Clemence and Finbarr 1981).

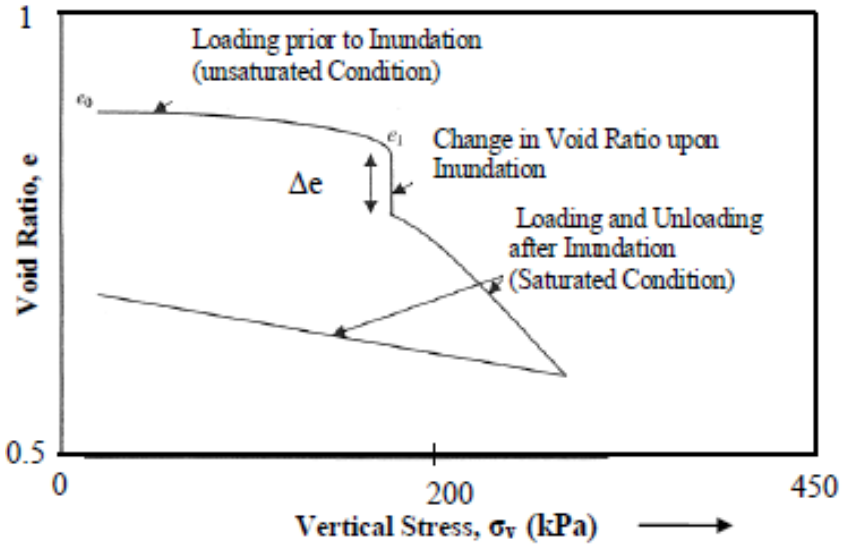

Fig. 2-2. Sudden volume change of inundated collapsible soils (El-Howayek et al., 2011).

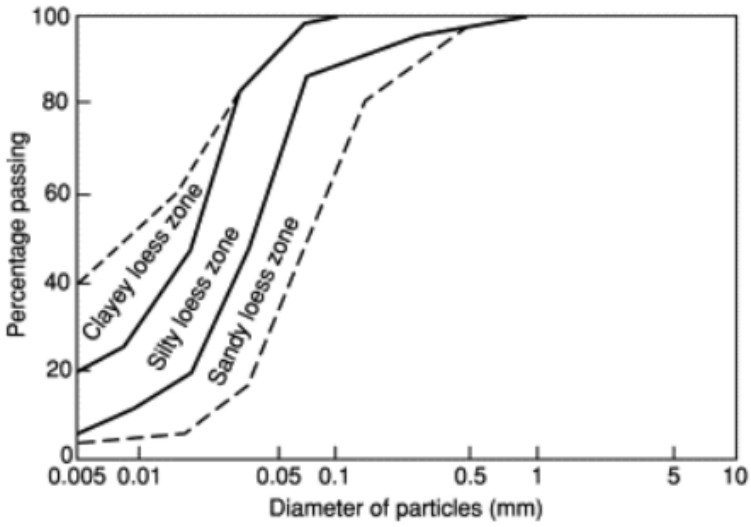

Fig. 2-3. F.G. Bell, in Encyclopedia of Geology (2005).

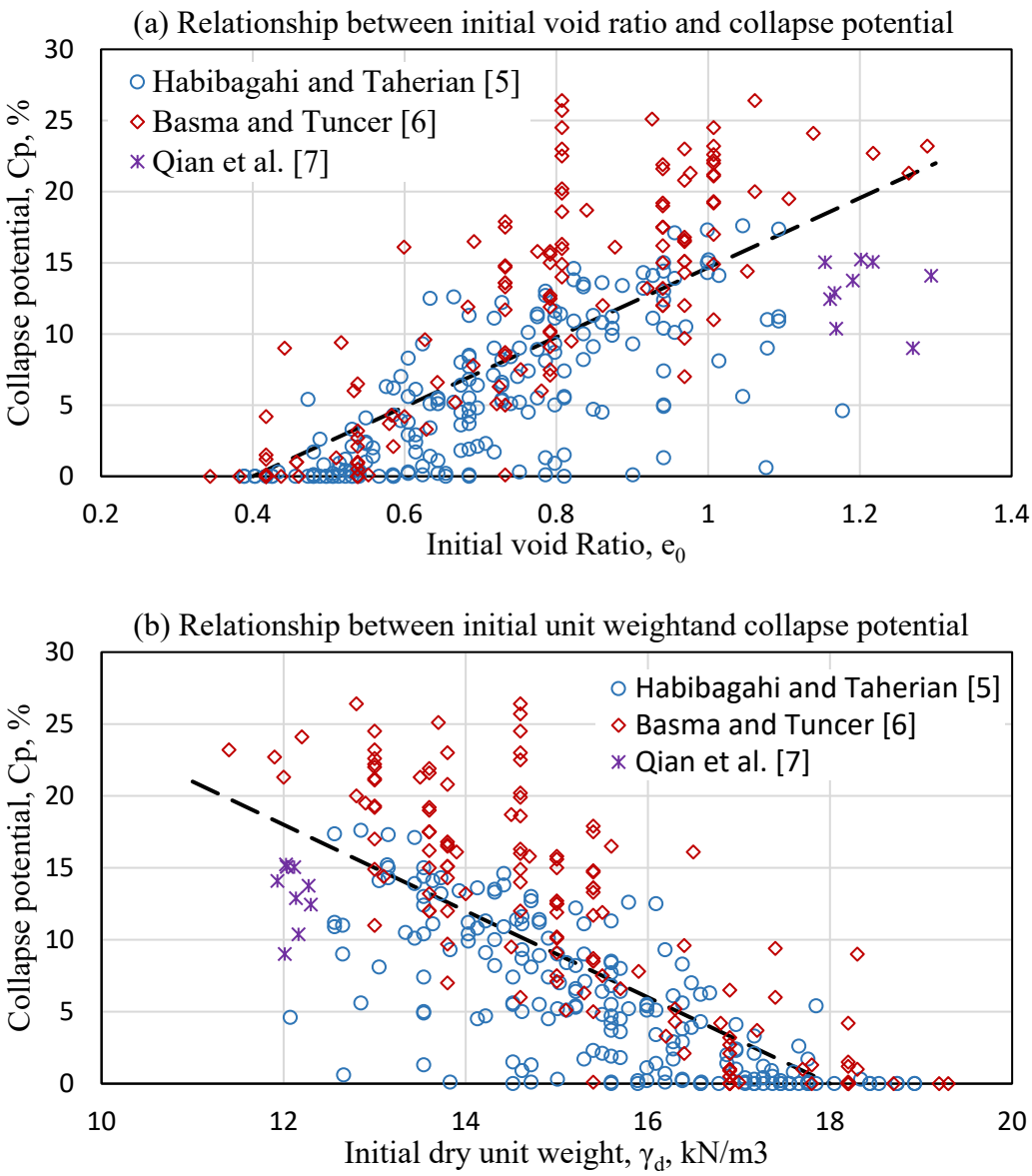

Fig. 2-4. Relationship of the collapse potential versus initial void ratio and dry unit weight.

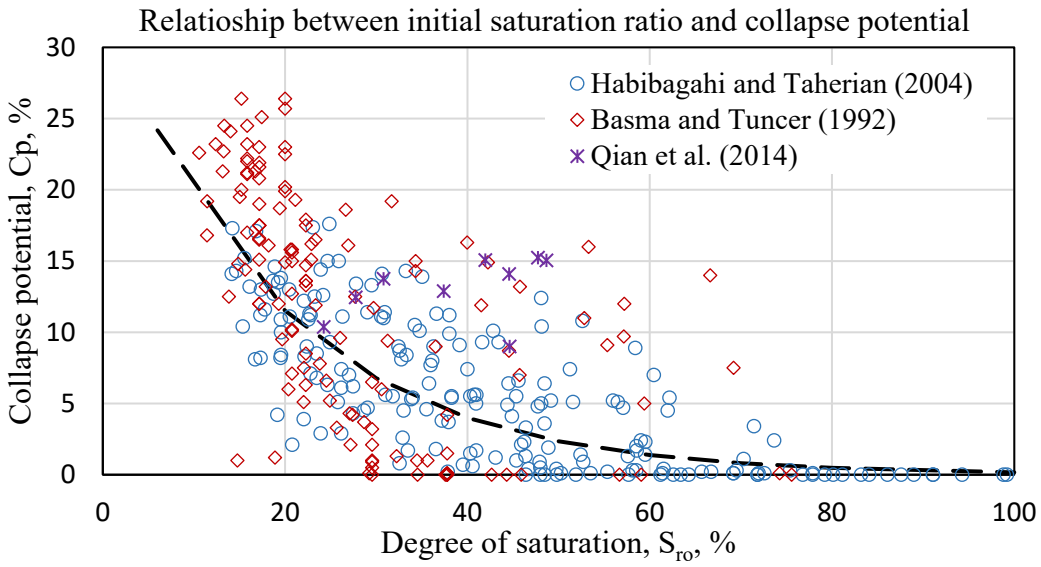

Fig. 2-5. Relationship between the collapse potential and the initial degree of saturation.

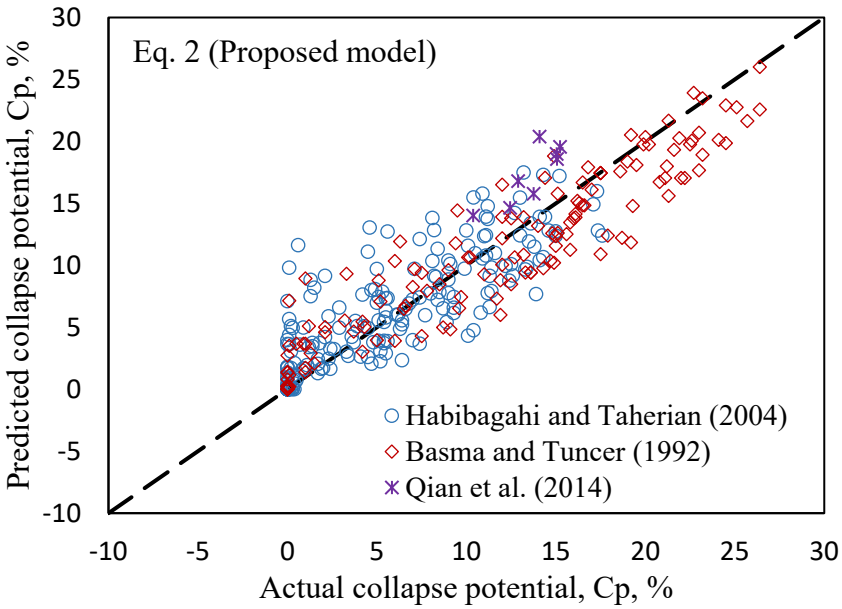

Fig. 2-6. Predictions of the proposed model versus experimental data of inundated collapsible soils.

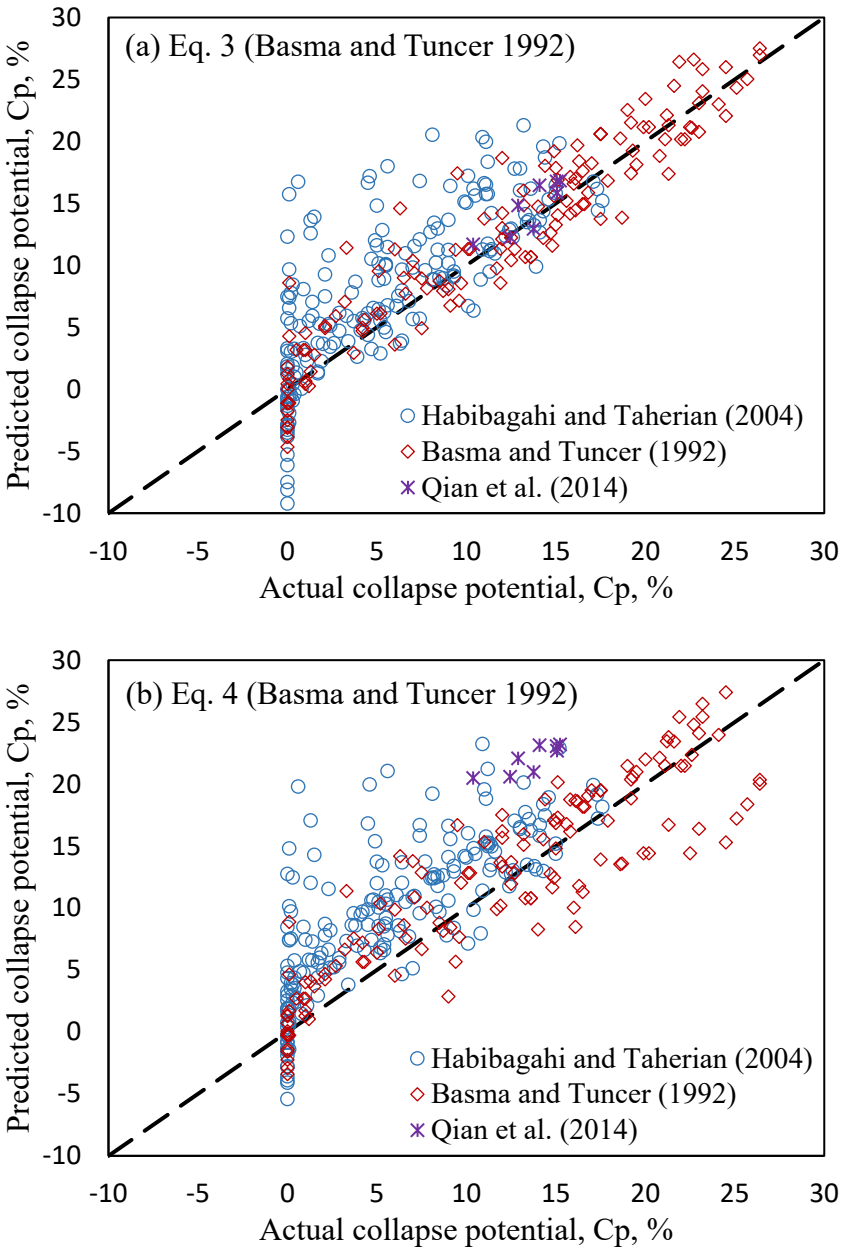

Fig. 2-7. Predictions of Eqs. 3 and 4 versus experimental data of inundated collapsible soils.

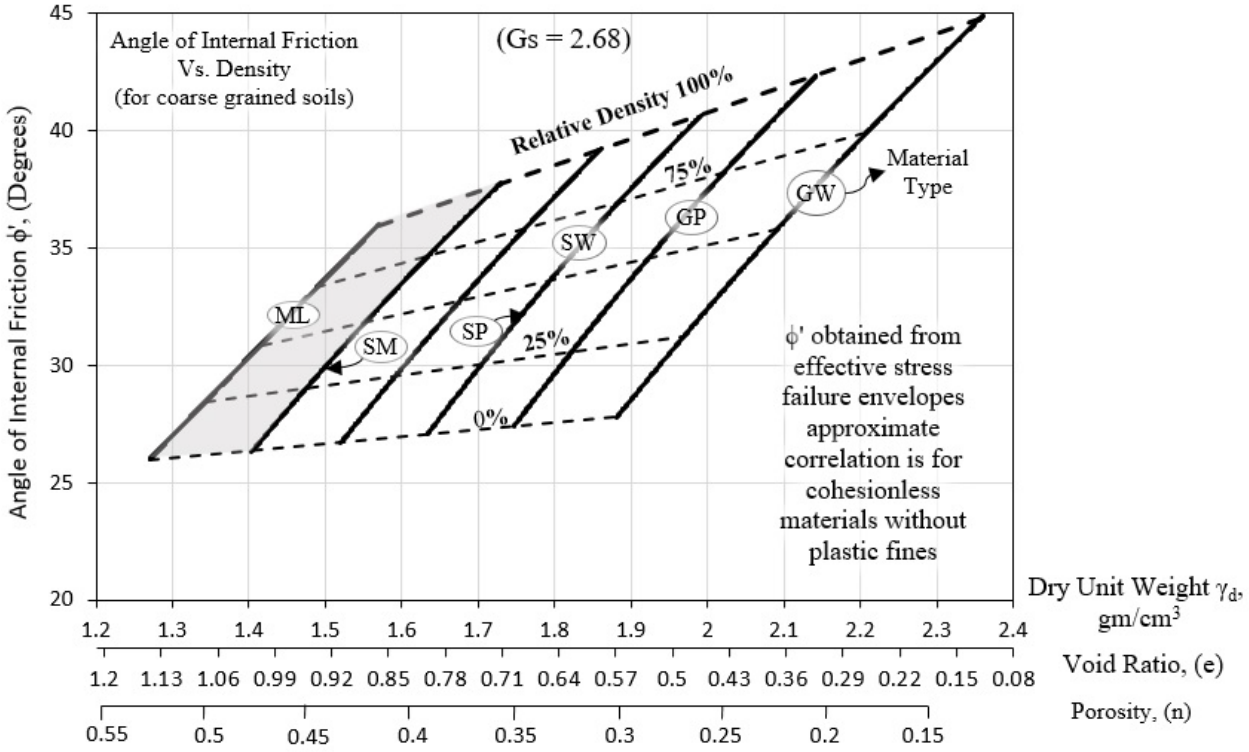

Fig. 2-8. Correlations of strength characteristics for granular soils after NAVFAC (1986).

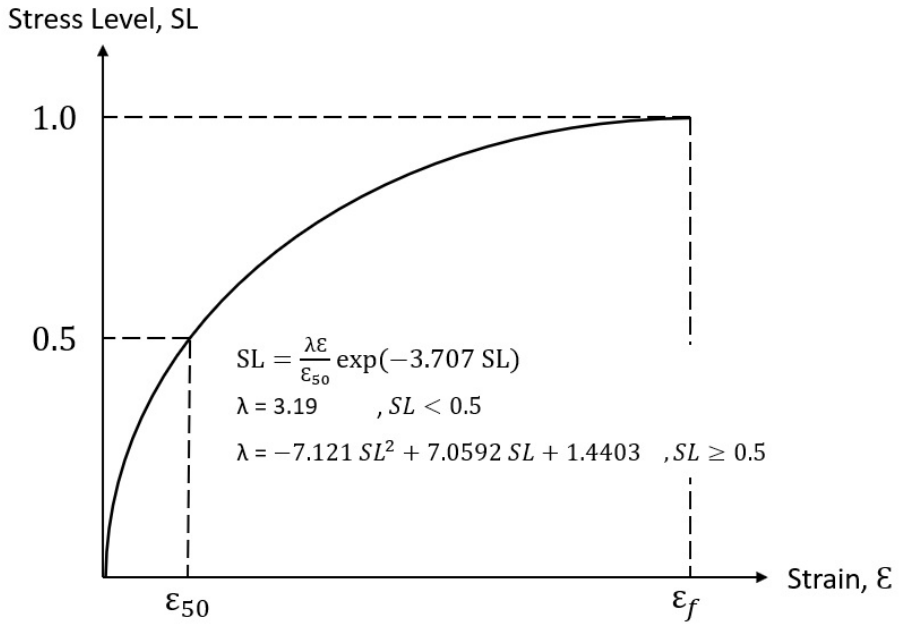

Fig. 2-9. Soil constitutive model after (Norris, 1986; Ashour et al., 2019).

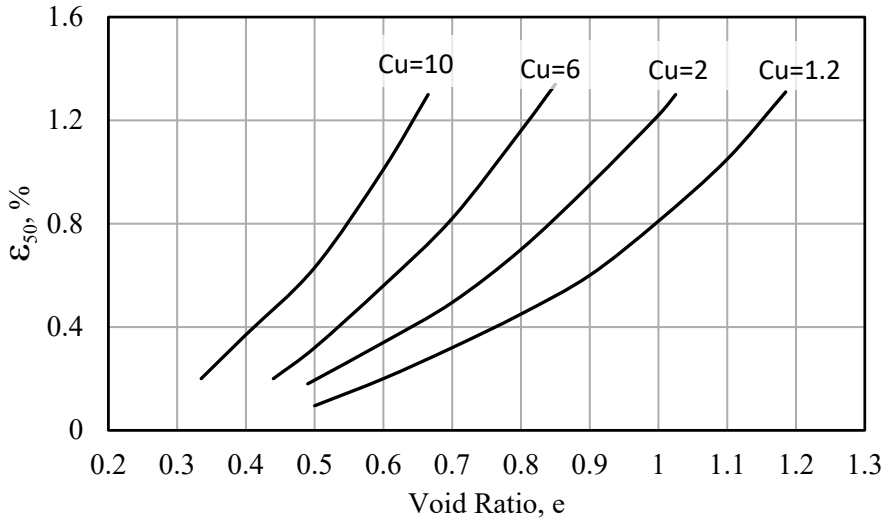

Fig. 2-10. Relationship between (ε_{50}), uniformity coefficient (C_u) and void ratio (e) after Norris (1986)

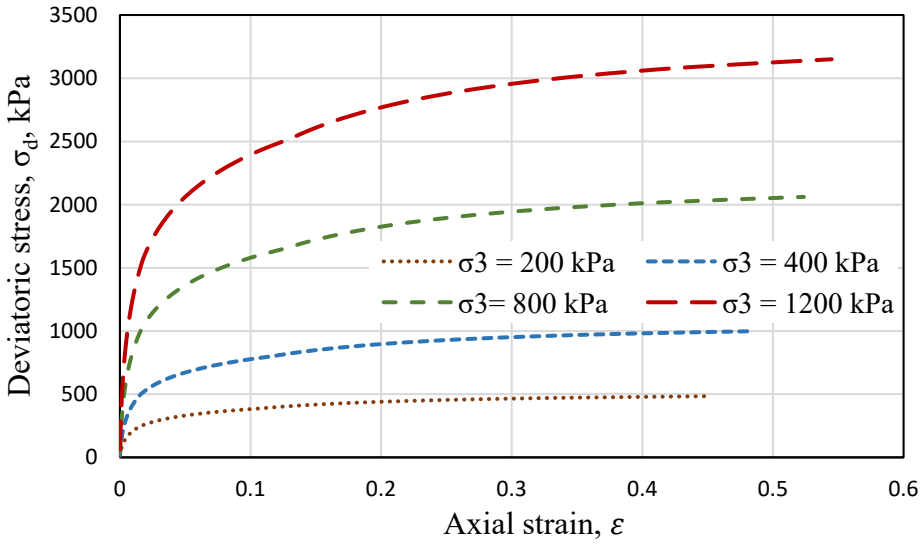

Fig. 2-11. Effect of confining pressure (σ_3) on the behavior of inundated collapsible soil as obtained from a conventional triaxial test.

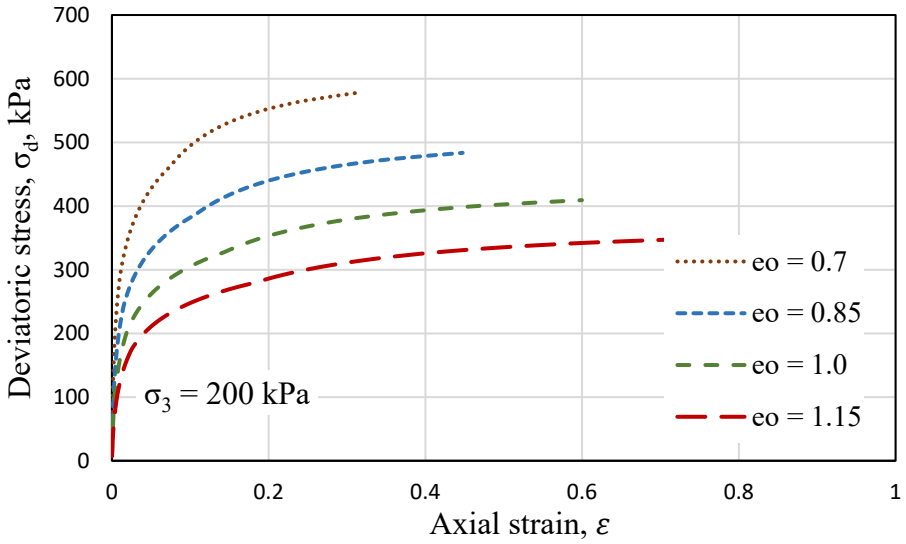

Fig. 2-12. Effect of initial void ratio on the behavior of inundated collapsible soil.

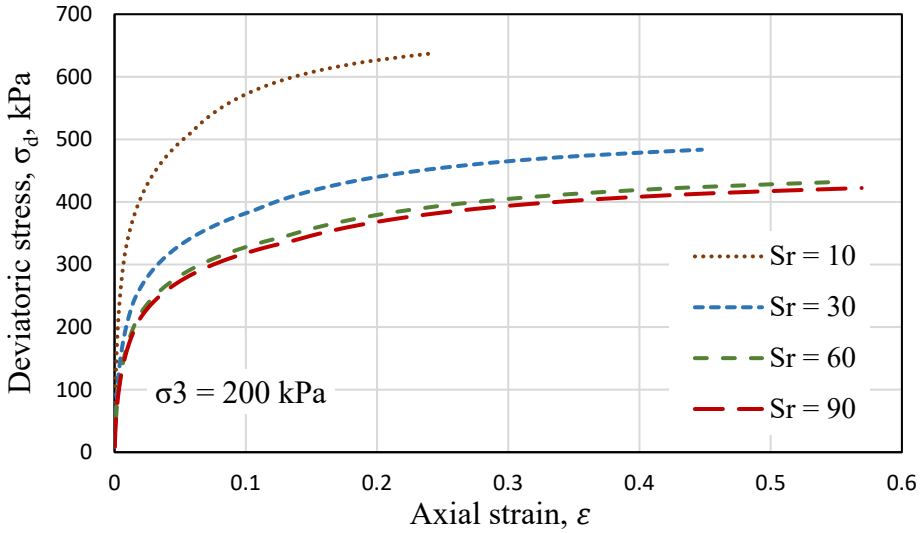

Fig. 2-13. Effect of soil saturation on the behavior inundated collapsible soil.

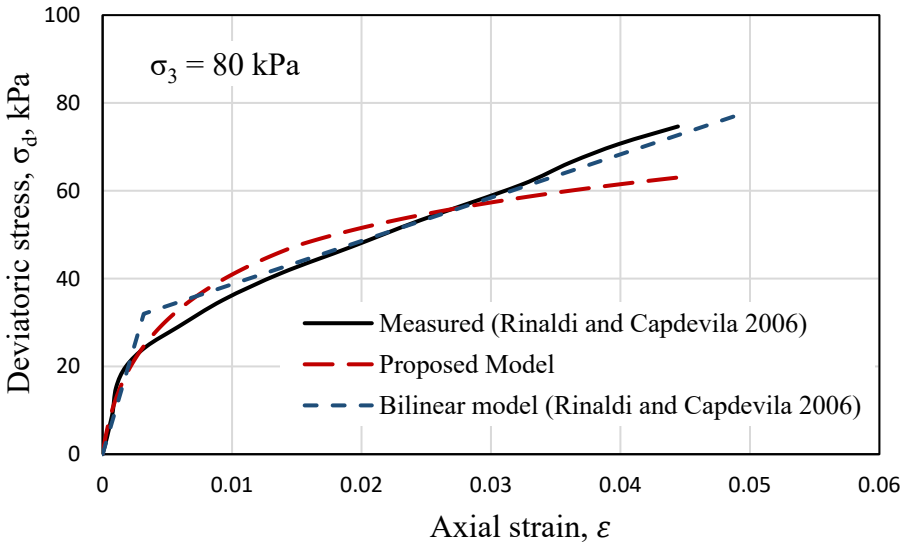

Fig. 2-14. Comparison between predicted and measured stress-strain curves.

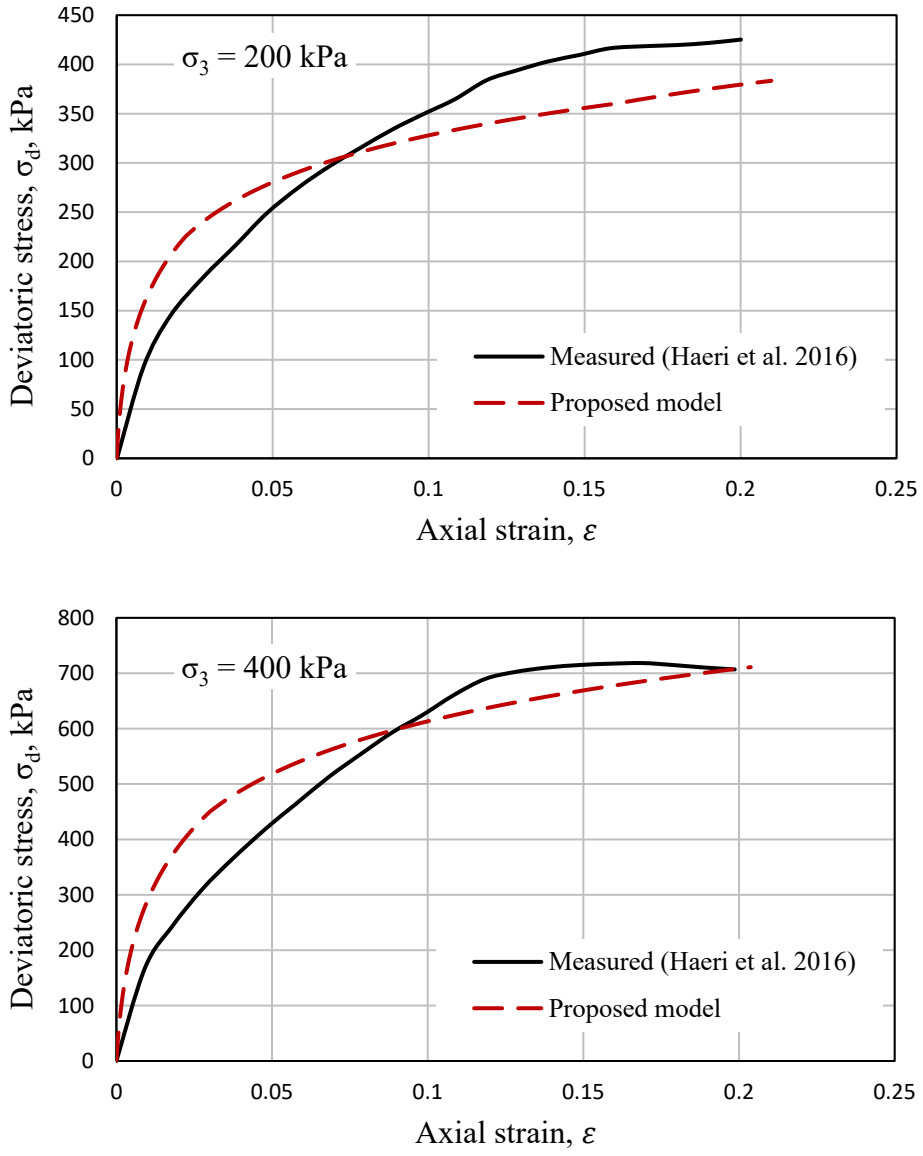

Fig. 2-15. Comparison between predicted and measured stress-strain curves.

Chapter 3. Pile side and tip response in sandy soil

3.1 Introduction

Piles in cohesionless soil gain their support from the tip resistance and transfer of axial load via the pile wall/shaft resistance along its length. The contribution of pile shaft resistance to the axial load carried by the pile proportionally increases with pile embedded length. It should be noted that both the pile tip and skin resistance are interdependent. The estimation of the axial pile capacity relies heavily on empirical correlations. The pile shaft resistance is influenced by the state and properties of soils within the critical zone immediately surrounding the pile. In addition, the method utilized for driving the pile, the roughness of the pile surface (i.e., pile materials), and the state of the pile end (closed/open end) have their influence on the pile shaft resistance.

The assessment of the mobilized load transfer of a pile in sand depends on the success in developing a representative (t-z) relationship. This can be achieved via empirical relationships or numerical methods. The load transfer-settlement (t-z) curve method is the most widely used technique to compute the response of axially loaded piles and is particularly useful when the soil behavior is clearly nonlinear and/or when the soil surrounding the pile is stratified. This method involves modeling the pile as a series of elements (segments) supported by discrete nonlinear springs, which represent the soil-pile skin friction (t-z springs), along with a nonlinear pile tip (end - bearing) Q_p-Z_p spring as seen in Fig. 3-1

The semi-empirical procedure presented in this report for axially loaded piles utilizes the stress-strain relationship of sand (Norris, 1986 and Ashour et al., 1998) to obtain the t-z curve and pile shaft resistance in sand as established by Ashour and Helal (2017). The method of slices utilized in this technique determines the degradation of shear stress/strain and vertical displacement within the vicinity of the axially loaded pile under drained static conditions. As a result, the t-z curves and the variation of side resistance along the pile length can be assessed using a combination of tip and side resistance/displacement of the pile and associated pile elastic deformation. In reality, it is recognized that mobilizing the shaft resistance requires very small movements, whereas mobilizing an ultimate toe resistance requires many times larger movement (Fellenius, 1999).

3.1.1 Side Resistance (Load Transfer–Settlement Model, t-z, of Sands)

The proposed methodology models the soil around the pile-shaft segment, Hs, at depth x with soil slices (1, 2, 3, …, m + n) that deform vertically, as shown in Fig. 3-2. Hs can be assumed equal to the pile diameter, D. The shear stress-strain caused by the shaft settlement, z, at a particular depth gradually decreases along the radial distance, r, from the pile shaft. As seen in Fig. 3-2, the shear stress, τ, settlement z (i.e., soil shear strain, γ) show the largest values (τ_0, z_0, and γ_0) for a particular load increment at the soil-pile interface where r is r_0. Kraft et al. (1981) showed that the actual radial decrease of shear stress and displacement in the sand in the vicinity around the pile takes a parabolic pattern. The suggested model assumes a nonlinear parabolic decreasing pattern for soil vertical displacement z versus radial distance r as

$$Z_s = Z_0 \left(\frac{r_0}{r}\right)^2 \tag{3-1}$$

where r = radial distance of the point of question; and $z = z_0$ at $r = r_0$. The variation of vertical soil displacement in the radial direction [Eq. (2-1)] is assumed on the basis of experimental data observed by Robinsky and Morrison (1964) and the analyses presented by Seo et al. (2008) and Chow (2007).

Isotropic conditions are assumed in sands after pile installation, and horizontal (confining) stress is equal to the effective vertical overburden, $\bar{\sigma}_{v_0}$ (i.e., lateral earth pressure coefficient K = 1 and $\bar{\sigma}_{3_0} = \bar{\sigma}_{v_0}$ before loading), as shown in Fig. 3-3a. The shear strain associated with vertical soil displacement in a sand slice i between r_i and r_{i+1} [Fig. 3-2] is determined via Eq. 3-2.

$$\gamma_i = \frac{z_i - z_{i+1}}{r_{i+1} - r_i} = \frac{\Delta z_i}{\Delta r_i} \tag{3-2}$$

where Δr_i has smaller values close to the pile wall that increase away from the pile [Fig. 3-2]. The pile settlement at depth x is accompanied by τ_0 at the soil-pile interface, Mohr's circle of radius τ_0, and confining pressure $\bar{\sigma}_3$. As shown in Fig. 3-3, the progress in the axial load produces larger Mohr's circles with larger values of τ_0 and decreasing values for $\bar{\sigma}_3$ until τ_0 is equal to τ_{max} when the mobilized friction angle, ϕ_m, in the sand become equal to the soil-pile friction angle, δ. Fig. 3-2 demonstrates the decrease of τ_0 at the soil-pile interface (caused by pile settlement z) with radial distance r until τ and z become equal to 0 at a large value of r. The

constitutive model for drained soil presented by Norris (1986) and then improved by Ashour et al. (2019) (Fig. 3-4) is used to determine the associated normal and shear strains, ε and γ, respectively, as

$$\gamma = \varepsilon(1 + \upsilon) \tag{3-3}$$

$$\text{SL} = \frac{\sigma_d}{\sigma_{df}} = \frac{2\tau}{\sigma_{df}} \tag{3-4}$$

$$\sigma_{df} = \bar{\sigma}_3 * \left[\left(\tan\left(45 + {}^{\Phi}/_{2}\right)\right)^2 - 1\right] \tag{3-5}$$

The Poisson's ratio υ is assumed to change from 0.1 to 0.5 as a function of the stress level in soil, *SL*, as

$$\upsilon_s = 0.1 + 0.4SL \tag{3-6}$$

The development of the t-z curve for sand requires the assessment of the shear strain at the soil-pile interface (γ_0) corresponding to a given value of the pile displacement at the midpoint of the pile segment in question (z_{mid}) using Eqs. 3-1 and 3-2. For a specific segment settlement z_{mid} at depth x, a mobilized value of τ_0 (Fig. 3-3) is assumed to calculate the associated confining pressure, $\bar{\sigma}_3$, *SL*, ε_0 , and γ_0 at the soil-pile interface using the constitutive model shown in Fig. 3-4 and Eqs. (3-3 through 3-6). τ_0 is adjusted for the pile segment in question until the calculated γ_0 converges properly with γ_0 of the pile segment obtained from the global iterative stability analysis of the pile-side and tip-resistance model shown in Fig. 3-1.

3.2 Pile tip (point) resistance and settlement ($Q_p - z_p$) in sand

It is evident that the associated pile tip resistance manipulates the side resistance of the pile shaft. As presented in the analysis procedure, the pile tip resistance should be assumed in the first step. As a result, the shear resistance and displacement of the upper segments of the pile can be computed based on the assumed pile tip movement. This indicates the need for a practical technique that allows the assessment of the pile tip load-displacement relationship under a mobilized or developing state. It should be emphasized that the presented procedure has the advantage of utilizing the same stress-strain model of sand (Fig. 3-4) to determine the mobilized resistance and associated settlement at the pile tip and along the side of the pile.

In association with the pile side shear resistance model presented in this study, the approach established by Elfass (2001) is employed to compute the pile tip load-settlement in sand. The failure mechanism model assumes four failure zones represented by four Mohr circles, as shown in Fig. 3-5. This mechanism yields the bearing capacity (q) and its relationship with the deviatoric stress (σ_d) of the last (fourth Mohr circle), as shown in Fig. 3-5.

$$\sigma_d = 0.6\, q \tag{3-7}$$

The pile tip resistance (Q_P) is given as,

$$Q_p = q\, A_{base} = \frac{\sigma_d}{0.6}\, A_{base} \tag{3-8}$$

where A_{base} is the cross-sectional area of the pile tip.

As seen in Fig. 3-5, the Mohr-Coulomb strength envelope is nonlinear and requires the evaluation of the secant angle of the fourth circle (ϕ_{IV}) tangent to the curvilinear envelope. The angle of the secant line tangent to the first circle (ϕ_I) at effective overburden pressure can be obtained from the field blow data count (SPT test) or a triaxial laboratory test at approximately 100 kPa [1 ton per square foot (tsf)] confining pressure. Due to the increase in the confining pressure ($\bar{\sigma}_3$) from one circle to the next, the friction angle (ϕ) decreases from ϕ_I at $(\bar{\sigma}_3)_I$ to ϕ_{IV} at $(\bar{\sigma}_3)_{IV}$ assuming a value for $\Delta\phi$ where

$$\phi_{IV} = \phi_I - \Delta\phi \tag{3-9}$$

Based on the following Bolton (1986) relationship modified by Elfass (2001), as shown in Fig. 2-6,

$$\phi_{peak} = \phi_{min} + \phi_{diff} \tag{3-10}$$

$$\phi_{diff} = 3I_R = 3D_r \left\{10 - \ln\left[\left(\frac{2+\tan^2(45+\phi/2)}{3}\right)\bar{\sigma}_3\right]\right\} - 1 \tag{3-11}$$

$\bar{\sigma}_3$ is in kPa, and ϕ_{min} is the lowest friction angle that ϕ may reach at high confining pressure, and D_r is used as a decimal value. Knowing the sand relative density (D_r) and associated friction angle under original confining pressure ($\bar{\sigma}_3 = \bar{\sigma}_{v0}$), Eq. 3-11 can be used to calculate the reduction in the friction angle $\Delta\phi$ due to the increase of the confining pressure from $\bar{\sigma}_{v0}$ to $(\bar{\sigma}_3)_{IV}$ and the associated decrease of the friction angle from ϕ_I to ϕ_{IV}. Assume a reduction

($\Delta\phi$ = 3 or 4 degrees) in the sand friction angle at ($\bar{\sigma}_3 = \bar{\sigma}_{v0}$) due to the increase in the confining pressure from $\bar{\sigma}_{v0}$ to $(\bar{\sigma}_3)_{IV}$, as seen in Fig. 3-6. Therefore,

$$\Delta \int \phi \quad = \left(\int \phi_{diff}\right)_I - \left(\int \phi_{diff}\right)_{IV} \tag{3-12}$$

However, the friction angle ϕ_{IV} associated with $(\bar{\sigma}_3)_{IV}$ can also be calculated as

$$\phi_{IV} = \phi_I - \Delta\phi \log \frac{(\bar{\sigma}_3)_{IV}}{\bar{\sigma}_{v0}} \tag{3-13}$$

Compare the assumed value of ϕ_{IV} with the value obtained in Eq. 3-9. If they are different, adjust for new value and repeat the process (Eqs. 3-9 through 3-13) until the value of ϕ_{IV} converges and the difference in $\Delta\phi$ calculated yields to the targeted tolerance.

Using the deviatoric stress (σ_d) of the fourth circle, one obtains,

$$\sigma_{df} = (\bar{\sigma}_3)_{IV}\left[\tan^2\left(45 + \phi_{IV}/2\right) - 1\right] \tag{3-14}$$

where

$$(\bar{\sigma}_3)_{IV} = \bar{\sigma}_{v0} + q - \sigma_d = \bar{\sigma}_{v0} + 0.4q \tag{3-15}$$

The current stress level (SL) in soil (Zone 4 below pile tip) is evaluated as

$$SL = \frac{\tan^2(45+\phi_m/2)-1}{\tan^2(45+\phi_{IV}/2)-1} = \frac{\sigma_d}{\sigma_{df}}; \quad \sigma_d = SL\,\sigma_{df} \tag{3-16}$$

where

$$\phi_m = \sin^{-1}\left[\frac{\sigma_d/2}{(\bar{\sigma}_3)_{IV}+\sigma_d/2}\right] \tag{3-17}$$

3.3 Pile tip settlement

The pile tip displacement in the sand can be determined based on the drained stress-strain relationship presented in Fig. 3-4 where the soils strain (ε) below the pile tip is evaluated according to the model shown in Fig. 3-7.

For a constant Young's modulus (E) with depth, the strain or ε_1 profile has the same shape as the elastic ($\Delta\sigma_1$ - $\Delta\sigma_3$) variation or Schmertmann's I_z factor (Schnertmann, 1970, Schnertmann et al., 1979 and Norris, 1986). Taking ε_1 at depth r_o below the pile tip (the peak of

the I_z curve), the pile tip displacement (z_P) is a function of the area of the triangular variation (Fig. 3-7).

$$Z_p = 2\,\varepsilon\,r_0 \tag{3-18}$$

where r_o is the radius of the pile tip. Dealing with different values for pile tip resistance (Eq. 3-11), the associated deviatoric stress (Eq. 3-7), stress level (Eq. 3-16), and principal strain (ε) (Fig. 3-4) can be used to assess the tip movement in order to construct the pile tip load-settlement ($Q_P - z_P$) curve.

$$Z_p = 2\,\varepsilon\,r_0 \tag{3-19}$$

where r_o is the radius of the pile tip. Dealing with different values for pile tip resistance (Eqn. 3-11), the associated deviatoric stress (Eq. 3-7), stress level (Eq. 3-15), and principal strain (ε) (Fig. 3-4) can be used to assess the tip movement in order to construct the pile tip load-settlement ($Q_P - z_P$) curve.

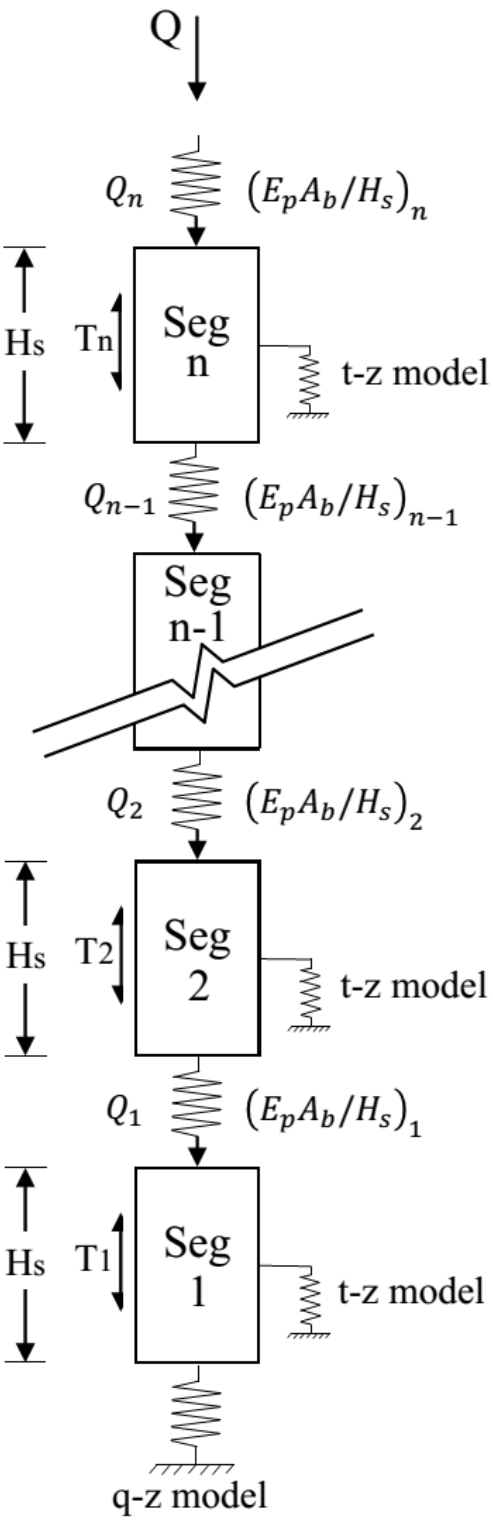

Fig. 3-1. Axially loaded pile-soil model.

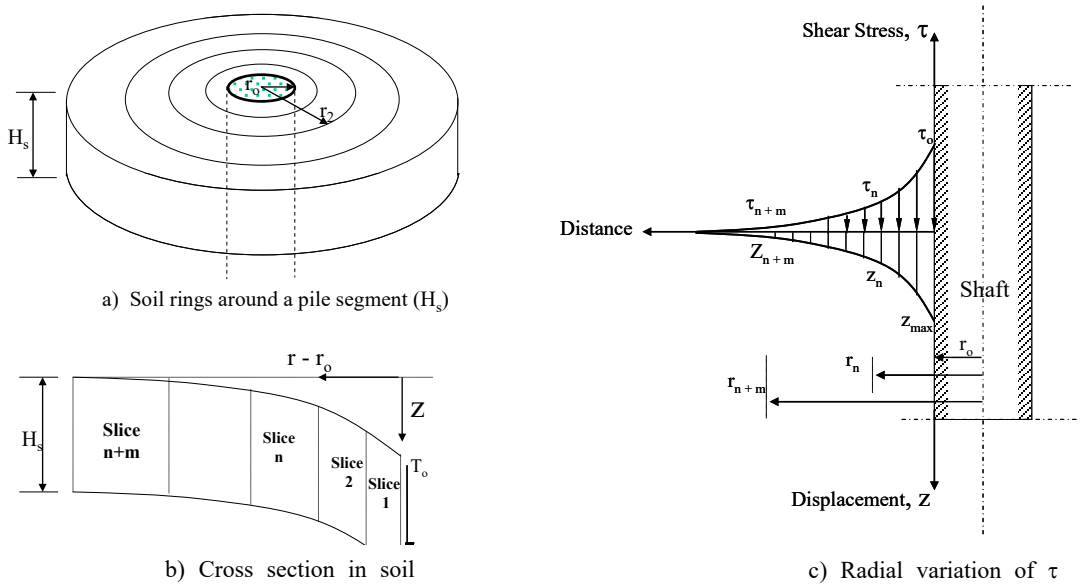

Fig. 3-2. Variation of displacement and shear stress with radial distance.

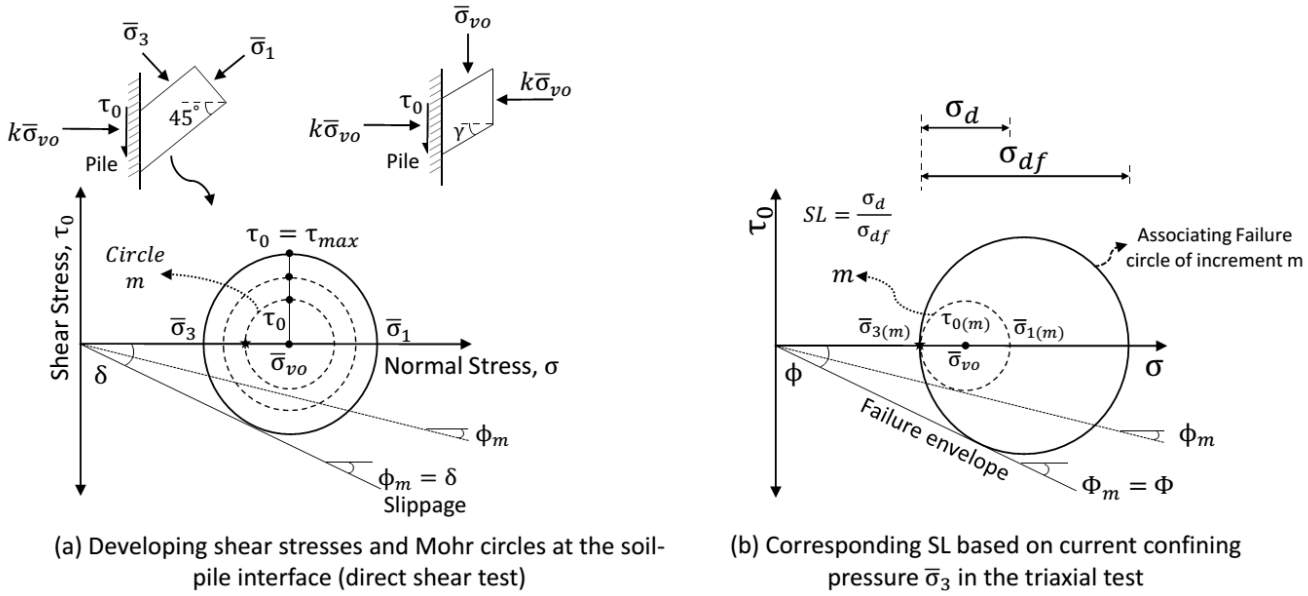

(a) Developing shear stresses and Mohr circles at the soil-pile interface (direct shear test)

(b) Corresponding SL based on current confining pressure $\overline{\sigma}_3$ in the triaxial test

Fig. 3-3. Progress of shear stress τ_0 at the soil-pile interface.

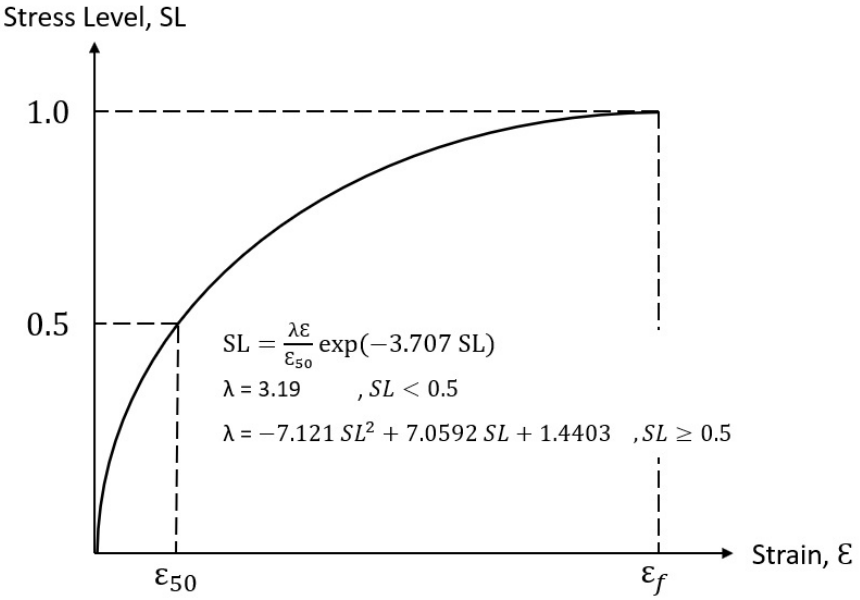

Fig. 3-4. Soil constitutive model (after Ashour et al., 2019 and Norris, 1986).

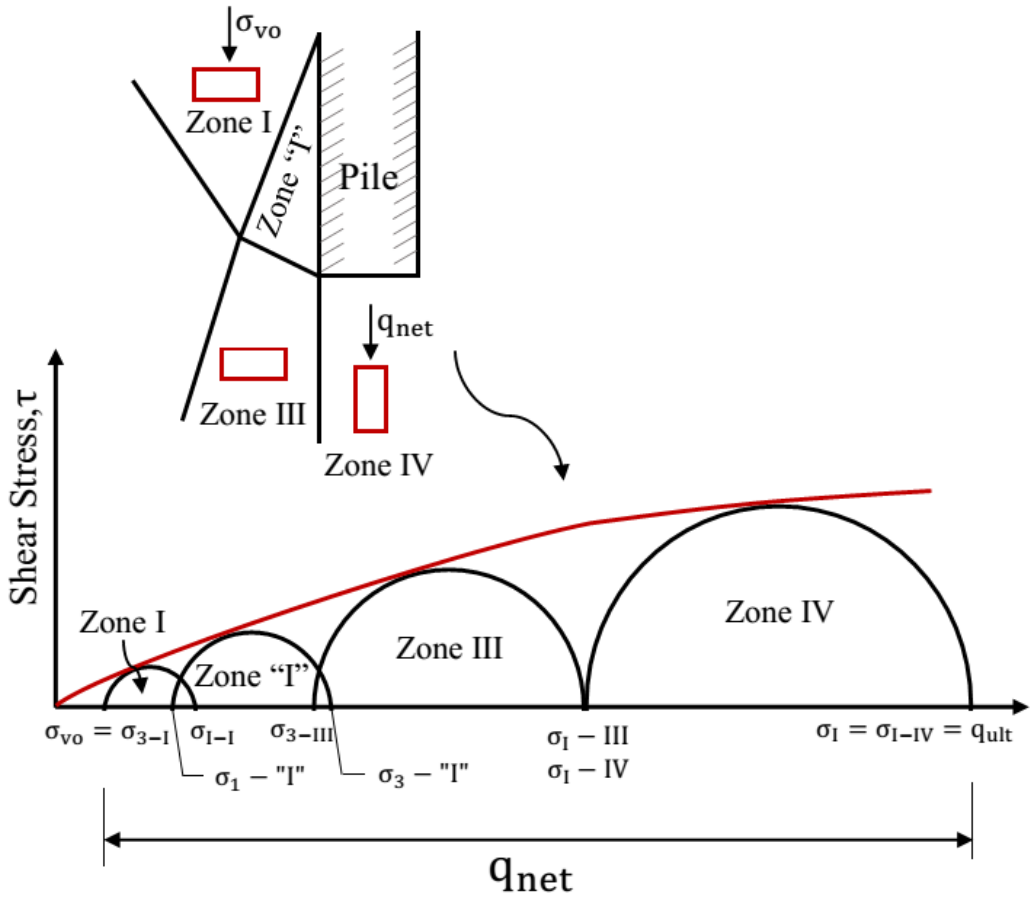

Fig. 3-5. Degradation in the secant friction angles of circles tangent to a curvilinear envelope of sand due to the increase in the confining pressure (Elfass, 2001).

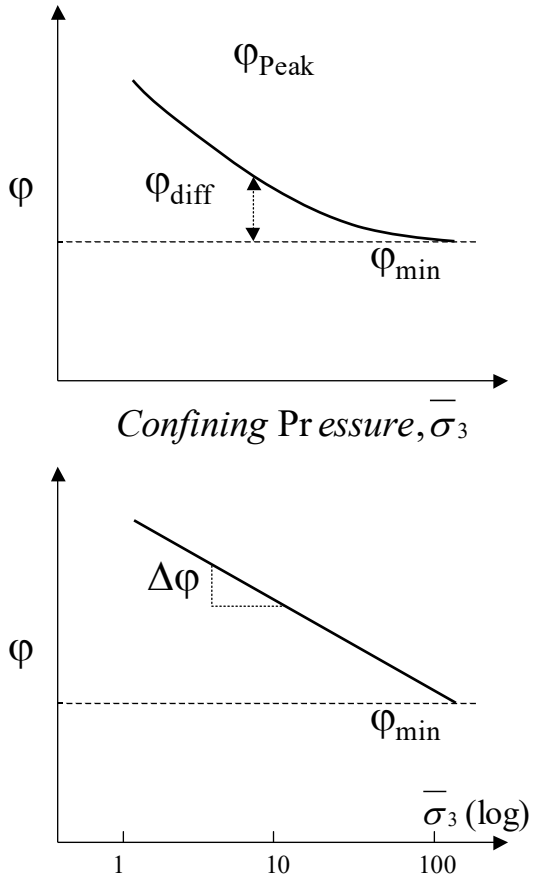

Fig. 3-6. Changes of Friction Angle (ϕ) with the Confining Pressure (Ashour et al., 2004)

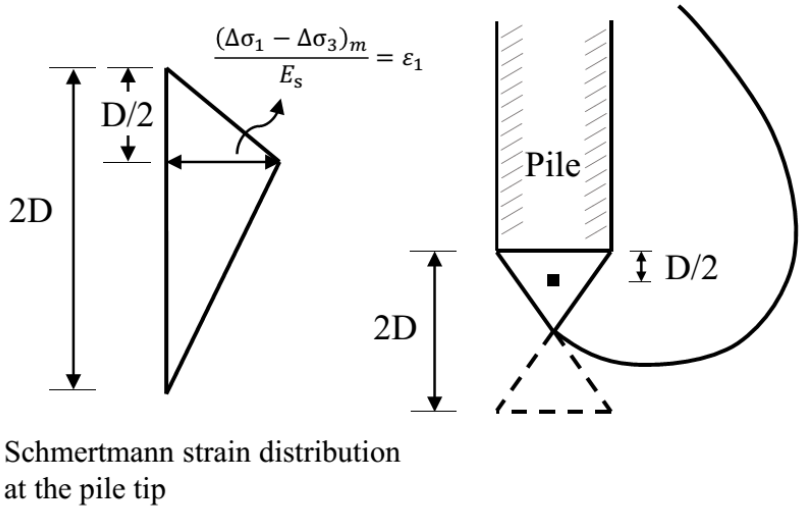

Fig. 3-7. Strain profile and the associated mobilized stresses immediately below the pile tip (after Elfass, 2001)

Chapter 4. Pile side and tip response in clay soil

4.1 Introduction

This chapter presents a procedure to evaluate the pile side load transfer (t-z) curves and the pile tip load-settlement curve with the consideration of pile material elastic deformation and the nonlinear stress-strain behavior of normally consolidated clay under undrained conditions. The technique presented allows the prediction of the radial variation (attenuation) of the pile settlement (z) and vertical shear stress in the soil zone around the pile. The study also evaluates the change in the axial load carried by the pile skin in clay soil as opposed to the pile tip. Despite the use of the undrained shear strength of clay, the technique presented (Ashour et al. 2010) employs the effective stress analysis by determining the pore water pressure induced under shear and normal stresses.

4.2 Methodology

The prediction of the mobilized vertical side shear of axially loaded piles is not feasible unless a relationship between the vertical pile displacement and the associated shear resistance is first established. To construct the load transfer and pile-head movement in clay under vertical load, the t-z curve for that particular soil should be assessed. As described by Randolph (2003), the driven pile history goes through three main phases (installation, equilibrium, and then loading). Also, it should be noted that the drop-in soil cohesion as a result of the installation disturbance is accompanied by a drop in the initial shear modulus of the clay, which is recovered after some time. The methodology presented herein deals with the loading phase and considers the effect of the pile materials (surface roughness) and the stiffness (type) of clay soil adjacent to the pile by adjusting the residual shear strength of the saturated clay in the immediate vicinity of the pile as presented in the NAVFAC (1986), Fig. 4-1.

The pile side load transfer (*t-z*) curve is assessed in this study by modeling the tip and side resistances of the pile using the elastic theory and Ramberg-Osgood (R-O) characterization of the stress-strain behavior of the soil. The approach involves modeling the pile as a series of elements supported by discrete nonlinear springs, which represent the resistance of the soil in skin friction (*t-z* springs), and a nonlinear spring at the pile tip representing the end-bearing (Q_p-z_p spring), as shown in Fig. 3-1 Accordingly, the axially loaded pile is sliced into a number of segments. Starting from the bottom segment, the side shear resistance and displacement of each

segment are then estimated. The method of slices reflects the analytical portion of the model that allows the assessment of the attenuating shear stress/strain and vertical displacement within the vicinity of the driven pile.

4.3 Pile side shear resistance in clay

For a given displacement (z), the mobilized shear stress (τ) at the pile-soil interface can be expressed as a function of the ultimate shear strength (τ_{ult}) via the shear stress level (SL_t). τ_{ult} is adjusted by the (C_α/C) ratio obtained from Fig. 4-1.

$$\mathrm{SL} = \frac{\tau}{\tau_{ult}} \tag{4-1}$$

The shear displacement of the soil around the pile decreases with increasing distance from the pile wall (Fig. 4-2). Based on a model study of the soil displacement pattern adjacent to a vertically loaded pile conducted by Robinsky and Morrison (1964), Norris (1986) estimated that the average shear strain, γ, within a zone of $D/2$ wide adjacent to the pile accounts for 75% of the shear displacement, z, as shown in Fig. 4-3. A linear shear strain, γ, in the influenced zone ($D/2$) can be expressed as

$$\gamma_{\mathrm{avg}} = \frac{0.75z}{D/2} = \frac{1.5\,z}{D} \tag{4-2}$$

For a given pile, one can find from Eq. (3-2) that

$$\frac{z_{50}}{z_f} = \frac{\gamma_{50}}{\gamma_f} \tag{4-3}$$

where z_{50} and γ_{50} are the pile displacement and associated shear strain in the soil at SL_t = 0.5 (i.e. $\tau = 0.5\tau_{ult}$), respectively. z_f and γ_f are the pile displacement and associated shear strain at failure where SL_t = 1.0 (i.e. $\tau = \tau_{ult}$). Therefore, the variation in the soil shear strain (γ) occurs in concert with the variation in pile displacement, as seen in Fig. 4-4. It should be noted that soil shear modulus (G) exhibits its lowest value next to the pile skin and increases radially away from the pile to reach it is maximum value (G_i) at γ and $z \cong 0$. Contrary to the shear modulus, the vertical displacement (z) and the shear strain (γ) reach their maximum value in the soil adjacent to the pile skin and decrease with increasing radial distance from the pile (see Fig. 4-3).

Using Eq. 4-3, the Ramberg-Osgood model represented by Richart (1975) can then be used to characterize the t-z curve as shown in the following equation,

$$\frac{Z_{mid}}{Z_r} = \frac{\gamma}{\gamma_r} = \frac{\tau}{\tau_{ult}}\left[1 + \beta\left(\frac{\tau}{\tau_{ult}}\right)^{R-1}\right] \quad (4\text{-}4)$$

or

$$\frac{Z_{mid}}{Z_r} = \frac{\gamma}{\gamma_r} = SL[1 + \beta(SL)^{R-1}] \quad (4\text{-}5)$$

where $\gamma_r = G_i / \tau_{ult}$, z is the total midpoint movement of pile segment (z_{mid}), γ and τ are the average shear strain and stress in the soil adjacent to the pile segment, G_i is the initial shear modulus at a very low stress/strain, and z_r is the pile segment movement associated to γ_r. As given in Eqs. (4-4) and (4-5), β and *R-1* are the fitting parameters of the Ramberg-Osgood model. At $\tau / \tau_{ult} = 1$, β can be presented as follows,

$$\beta = \frac{\gamma_f}{\gamma_r} - 1 \quad (4\text{-}6)$$

where γ_f is failure shear strain in the soil adjacent to the pile.

At $\tau / \tau_{ult} = 0.5$ and $\gamma = \gamma_{50}$, *R-1* is expressed as

$$R - 1 = \frac{\log\left[\left(2\frac{\gamma_{50}}{\gamma_r} - 1\right)/\beta\right]}{\log(0.5)} = \frac{\log\left[\left(2\frac{\gamma_{50}}{\gamma_r} - 1\right)/\left(\frac{\gamma_f}{\gamma_r} - 1\right)\right]}{\log(0.5)} \quad (4\text{-}7)$$

In order to determine β and *R-1*, the normal stress-strain relationship of clay (σ-ε) can be assessed to find γ_r, γ_{50}, and γ_f as shown in Fig 4-5 (a and b) and presented in the following equations.

Norris (1986) and then Ashour et al. (2019) developed a relationship that utilizes ε_{50} (normal strain at normal stress level, $SL = 0.5$) and S_u of clay, and provides the whole undrained stress-strain curve up to failure (i.e., E_i, E_{50} and ε_f).

$$\gamma_r = \frac{S_u}{G_i} = \frac{\tau_{ult}}{G_i} \quad (4\text{-}8)$$

and

$$\gamma_{50} = \frac{0.5\, S_u}{G_{50}} = \frac{S_u}{2G_{50}} \quad (4\text{-}9)$$

The initial shear modulus (G_i) at a very low SL_t and the shear modulus at $SL_t = 0.5$ (i.e., G_{50}) can be determined via their direct relationship with the normal stress-strain relationship and

Poisson's ratio (ν), where $\nu = 0.5$ for clay under undrained conditions as given in the following equations,

$$G_i = \frac{E_i}{2(1+\upsilon)} = \frac{E_i}{3} \tag{4-10}$$

$$G_{50} = \frac{E_{50}}{2(1+\upsilon)} = \frac{E_{50}}{3} = \frac{S_u}{3\varepsilon_u} \tag{4-11}$$

where E_i is the initial Young's modulus of clay at a very small value of the normal strain (ε) or normal stress level (SL). ε_{50} is the undrained normal strain of the clay soil at $SL = 0.5$ and can be obtained the triaxial undrained unconsolidated (UU) test or based on the value of S_u as presented by Evans and Duncan (1982), Fig. 4-6.

The shear strain at failure (γ_f) is determined in terms of the normal strain at failure (ε_f) as given in Eq. 3-12, ε_f is evaluated at $SL = 1$ or at normal strength σ_f where $\sigma_f = 2\ S_u$.

$$\gamma_f = \frac{\varepsilon_f}{(1+\upsilon)} = \frac{\varepsilon_f}{1.5} \tag{4-12}$$

Using the above equations, the Ramberg-Osgood (R-O) model fitting parameters β and R-1 are equal to 18.14 and 2.92, respectively.

4.4 Pile tip resistance and settlement

In this study, the bottom segment is the starting point for the mobilized shear stress and movement reconnaissance procedure from tip to head. Therefore, the pile resistance and settlement at the base of the pile should be identified for the progression of the analysis. The concept of Skempton's characterization (1951) is used in this study to determine the ultimate pile tip/base resistance in clays, Q_P.

$$\left(Q_p\right)_{ultimate} = q_{net}\ A_{tip} = 9\ C\ A_{tip} \tag{4-13}$$

Where q_{net} is the net bearing capacity of the pile at the base, A_{tip} is the area of the pile tip, and C is the cohesion of the soil below the pile tip (i.e., undrained shear strength, S_u). The mobilized pile tip resistance can be expressed as

$$Q_p = 9\ C_m\ A_{tip} = (q_{net})_m\ A_{tip} = 9\ C\ Sl\ A_{tip} \tag{4-14}$$

where $SL = C_m / C = \Delta\sigma_d / \sigma_{df} = \Delta\sigma_d / 2C$ as described in Fig. 3-7. $\Delta\sigma_d$ is the mobilized (current) deviator stress, and σ_{df} is the deviator stress at failure. The mobilized pile tip resistance $(q_{net})_m$ is a function of SL in the soil immediately below the pile tip.

Unlike Skempton's approach that finds the displacement beneath strip footing at 50% normal stress level (y_{50}) as $y_{50} = 2.5\ \varepsilon_{50}\ B$ (Skempton 1951), the approach in this study implements the elastic theory to determine the mobilized movement of the pile at any vertical soil strain level (ε) where E and $\nu = 0.5$ are the undrained Young's modulus and Poisson's ratio of clay, respectively. $\Delta\sigma_1$, $\Delta\sigma_2$, and $\Delta\sigma_3$ are the increase of the normal stresses in three dimensions. For $\Delta\sigma_2 = \Delta\sigma_3$, then

$$\varepsilon = \frac{\Delta\sigma_1 - \Delta\sigma_3}{E} + (1 - 2\nu)\frac{\Delta\sigma_3}{E} = \frac{\Delta\sigma_1 - \Delta\sigma_3}{E} = \frac{\Delta\sigma_d}{E} \quad (4\text{-}15)$$

where $\Delta\sigma_d$ is the current deviator stress.

Therefore, for a constant undrained Young's modulus (E_u) with depth under the pile tip (at a particular step of loading), the strain or (ε) profile has the same shape as the elastic ($\Delta\sigma_1 - \Delta\sigma_3$) variation or Schmertmann's I_z factor (Norris 1986, Schmertmann 1970, and Schmertmann et al. 1979) (Fig. 4-7). By ignoring Schmertmann's nonzero value of ε_1 at the base of the foundation and taking ε at depth D/2 below the pile tip (i.e., location of the peak of the I_z curve), the pile tip displacement (z_P) can be evaluated as a function of the area of the triangular variation (see Fig. 4-7).

$$z_p = \varepsilon\ D \quad (4\text{-}16)$$

where D is the diameter of the pile base/tip. Schmertmann's method, which is based on the elastic solution, allows the evaluation of the pile tip settlement by modeling the strain with depth below the pile tip and knowing the elastic modulus of soil.

To assess the undrained stress-strain curve of clay, the current procedure employs the normal stress-strain relationship (Eq. 4-17) developed by Norris (1986) and modified by Ashour et al. (2019).

$$SL = \frac{C_m}{C} = \frac{\lambda\varepsilon}{\varepsilon_{50}}\exp(-3.307\ SL) \quad (4\text{-}17a)$$

where 3.707 and λ represent the fitting parameters of the relationship. λ is equal to 3.19 at $\varepsilon = \varepsilon_{50}$ and then varies linearly with the stress level between 3.19 at $\varepsilon = \varepsilon_{50}$ and 2.14 at $\varepsilon = \varepsilon_{80}$. If *SL* is greater than 80 percent, the stress-strain relationship is given as

$$SL = 0.2 \exp\left(\frac{100\varepsilon}{59\varepsilon + 95.4\,\varepsilon_{50}}\right) \quad \text{(4-17b)}$$

As described earlier, ε_{50} of clay is determined based on the value of the undrained shear strength as developed by Evans and Duncan (1982).

4.5 (t-z) curve assessment procedure

The aforementioned approach of this study involves modeling the axially loaded pile as a series of elements supported by discrete nonlinear springs. Accordingly, the pile is sliced into a number of segments as employed in the Coyle and Reese (1966) method. However, the Coyle and Reese method (1966) was established for frictional piles (very small tip load) in soft clay and used standard and averaged t-z curves (curves A, B, and C) that were developed from full- and model-scale load test data. It should be noted that the pile tip load could become influential with stiff bearing soil layer. In the current study, ε_{50} and S_u are used to assess the normal and shear stress-strain relationships of the clay soil along the side and at the tip of the pile, the R-O model parameters, and then the shear resistance-displacement (load transfer) curve.

The assessment procedure begins at the bottom by assuming a small pile base resistance, computing the shear and axial forces and movement of each segment, and working up the pile. For the assumed pile tip resistance Q_P, the *t-z* curve can then be assessed from the obtained shear stress and the associated displacement at each depth. For different assumed tip resistances and associated tip settlements (Q_P-z_P), different values of pile head load and displacement at the pile top will be obtained, and a load-settlement curve (Q-δ) can be plotted. The step-by-step procedure for the incremental solution employed in the methodology developed for the assessment of (*t-z*), (Q-δ) and (Q_P-z_P) curves is given as follows:

1. Assume a small pile tip resistance, q_P (i.e., a small percentage of the soil net bearing capacity, q_{net}).
2. Compute the stress level (*SL*) and the mobilized undrained shear strength C_m (Eq. 4-14)
3. Compute the induced axial (deviatoric) soil strain ε_P, using the evaluated stress and the presented stress-strain relationship based on Eq. (4-15) and by using Eq. (4-17).

4. Compute the pile base displacement, z_P, using Eq. (4-16).
5. Divide the pile into several segments of an equal length (H_s) and consider the bottom load (Q_B) and base movement (z_B) of the last segment as tip load (Q_P) and tip settlement (z_P), respectively.
6. Estimate the total midpoint movement of the segment (z_{mid}) starting with the bottom segment (segment 1 in Fig. 3-1). The total midpoint movement of a segment is the combination of the segment bottom movement (z_B) and the elastic axial deformation ($z_{elastic}$), as seen in Eq. (4-18). The elastic axial deformation of the bottom half of a segment can be determined using Eq. (4-19). For the first trial, the midpoint movement for a segment can be assumed equal to the segment base movement.

$$z_{mid} = z_B + z_{elastic} \tag{4-18}$$

$$z_{elastic} = \frac{Q_B h/2}{EA_{base}} \tag{4-19}$$

7. Characterize the backbone response using the soil properties of the surrounding soil (S_u and ε_{50}) and the Ramberg-Osgood formula as in Eq. (4-5).
8. Obtain iteratively the average shear stress level ($SL_t = \tau / \tau_{ult}$) in clay around the pile segment using Eq. (4-5), and the evaluated movement z_{mid} in step 6.
9. Calculate the shear stress at clay-pile contact surface using Eq. (4-1).
10. Calculate the axial load carried by the pile segment in skin friction/adhesion (Q_s)

$$Q_s = \pi \mathrm{D} \mathrm{H}_s \tau \tag{4-20}$$

11. Calculate the total axial load (Q_T) carried at the top of the segment.

$$Q_T = Q_s + Q_B \tag{4-21}$$

12. Determine the elastic deformation at the bottom half of the segment, assuming a linear variation of the load distribution along the segment.

$$z_{elastic} = \left(\frac{Q_{mid} + Q_B}{2} H_s\right) / E_p A_p \tag{4-22}$$

where E_p is Young's modulus for the pile material, A_p is the area of the pile cross-section, and

$$Q_{mid} = \frac{Q_T + Q_B}{2} \tag{4-23}$$

13. Compute the new midpoint movement of the segment. Note that $z_B = z_p$ for the bottom segment (Segment 1 in Fig. 3-1),

$$z_{mid} = z_B + z_{elastic} \tag{4-24}$$

14. Compare the z_{mid} value calculated from step 13 with the previously estimated midpoint movement in step 4. If the difference between the two displacements is not within a specified tolerance, then repeat steps 7 through 14 using the new values of z_{mid} and Q_{mid} until convergence is achieved.
15. Calculate the top movement of the segment, z_T

$$z_T = z_B + \frac{Q_T + Q_B}{2} \frac{h}{E_P + Q_P} \tag{4-25}$$

16. Repeat the procedure (steps 6 through 15) for successive segments going up until reaching the top of the pile. Consecutively, the baseload (Q_B) and movement (z_B) of each segment are taken as Q_T and z_T of the previous segment, respectively. Eventually, the pile head load (Q) and top pile movement (δ) will be, respectively, the top axial load (Q_T) and the top movement (z_T) of the top segment (segment N in Fig. 3-1).
17. Using the shear stress (τ) and the associated displacement at each depth (i.e., the midpoint of the pile segment), plot the *t-z* curve for the specified pile head load.
18. Repeat steps 1 through 17 with different assumed tip resistances, q_p, to obtain different values of pile head load and displacement and finally plot the load-settlement (Q-δ) curve.

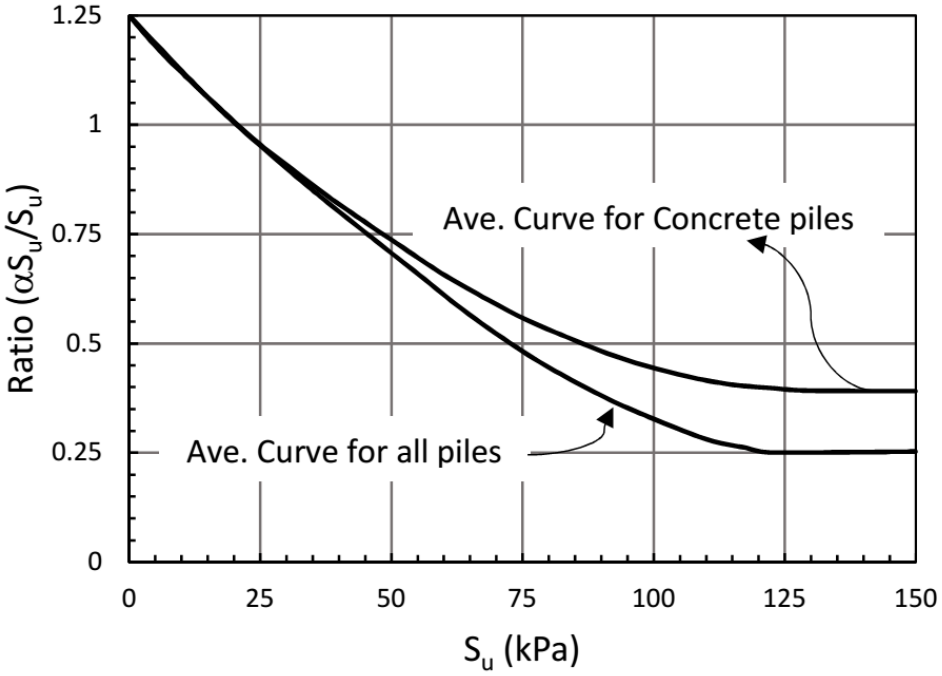

Fig. 4-1. Clay-pile adhesion based on pile materials and clay.

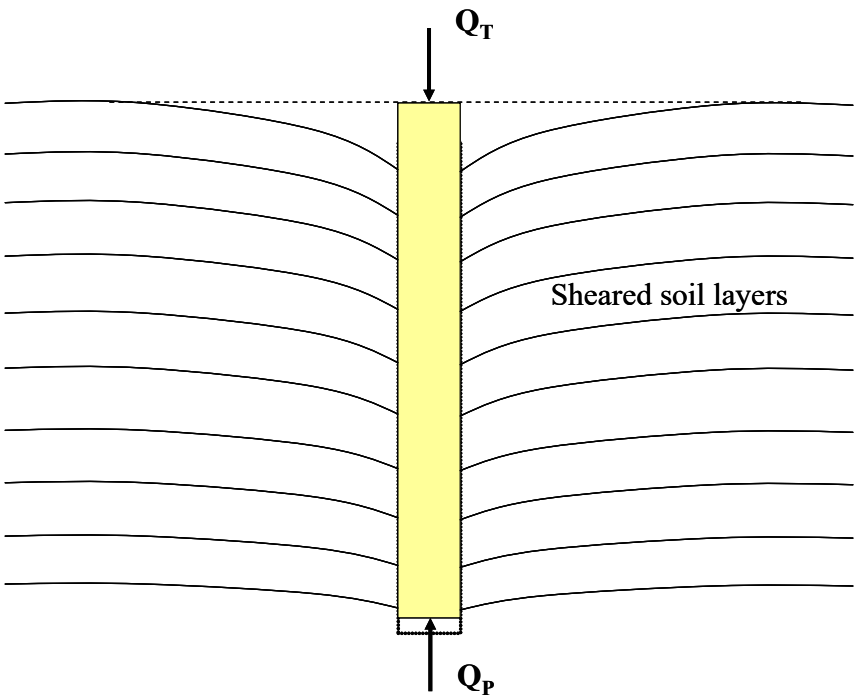

Fig. 4-2. Soil layer deformations around an axially loaded pile.

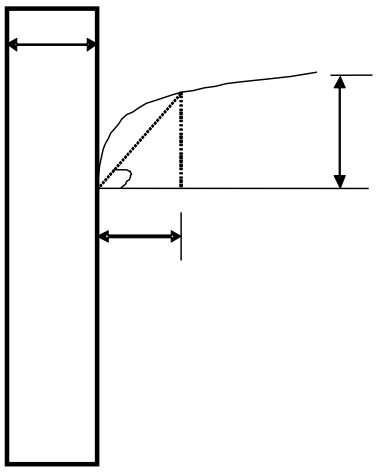

Fig. 4-3. Idealized relationship between shear strain in soil and pile displacement (Norris 1986).

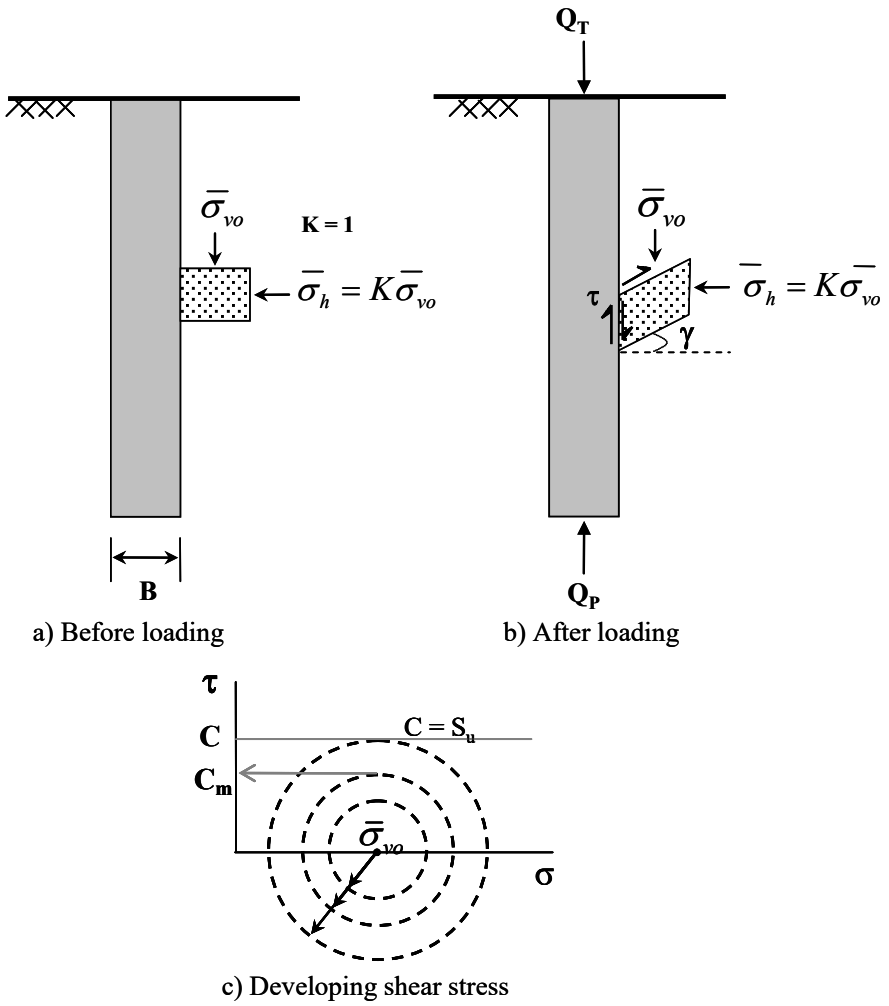

Fig. 4-4. Soil modeling at the soil-pile interface.

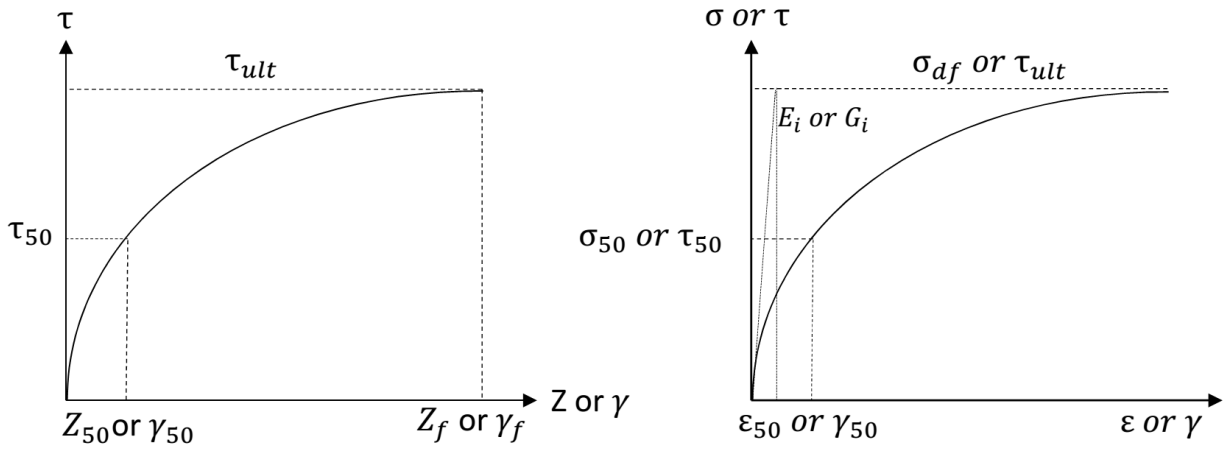

(a) Soil shear stress Vs. Shear strain and pile displacement

(b) Initial Young's and Shear modulus from soil normal/shear stress- strain curve

Fig. 4-5. Normal and shear stress-strain relationship in soil and the associated Young's and shear modulus.

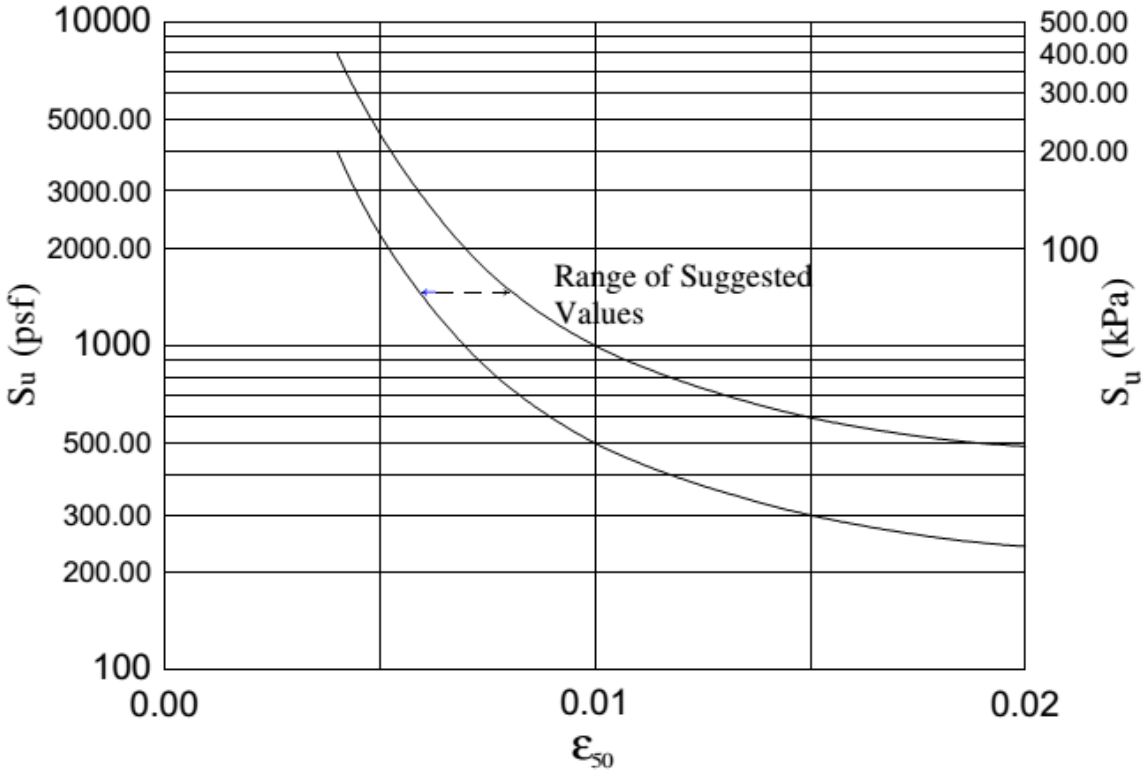

Fig. 4-6. Relationship of ε_{50} vs. Su (After Evans and Duncan 1982).

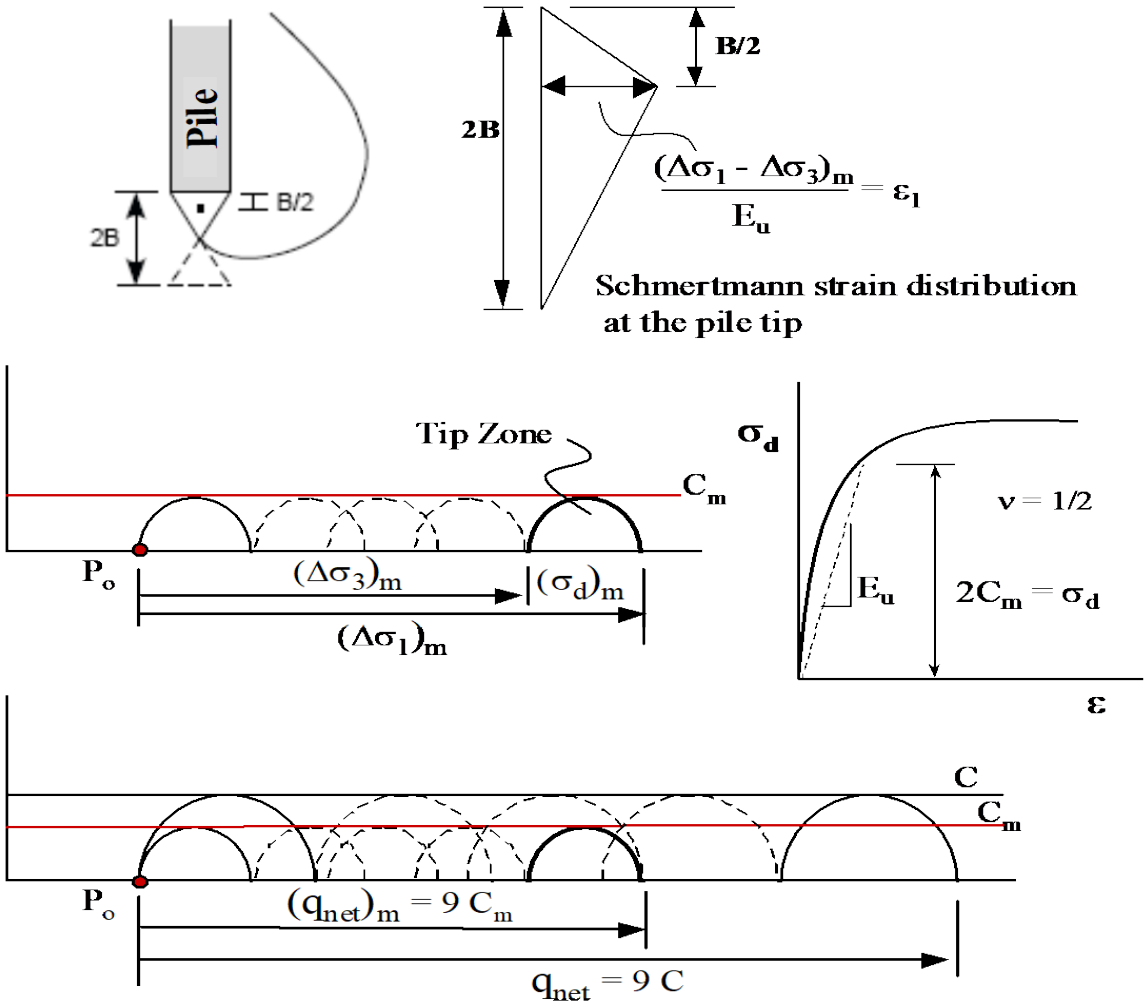

Fig. 4-7. Strain profile and the associated mobilized stresses immediately below the pile tip (After Elfass et al., 2008).

Chapter 5. Downdrag analysis procedures and validation

5.1 Introduction

The assessment of the mobilized pile negative skin friction depends on the relative soil downward movement to the pile displacement. This chapter presents two models for the analysis of piles subjected to downdrag. The first model presented herein is the model proposed by the FHWA (2016) (Hannigan et al., 2016). Second, the suggested technique, which couples the soil and pile settlement profiles with the pile mobilized skin-friction and end-bearing in an interactive model to determine the downdrag (pile settlement), load distribution along the pile length, and location of the neutral plane or transition zone.

5.2 FHWA 2016 method

Hannigan et al. (2016) classify the drag force and the downdrag as structural strength and geotechnical serviceability limit states problems, respectively. Hannigan et al. (2016) adopted the method developed by Fellenius (1989) and modified by Siegel et al. (2013) for downdrag analysis. The approach adopted by Hannigan et al. (2016) allows the assessment of the neutral plane location based on the equilibrium between the pile-head permanent load plus the mobilized negative skin friction on one side, and an assumed value of the mobilized pile toe resistance plus the mobilized positive pile side resistance on the other side. The settlement due to the downdrag is then determined as the settlement of the compressible soil layer below the neutral plane, which is induced by the increase of the soil's effective stress due to fill placement, dewatering, or other reasons.

5.2.1 FHWA 2016 step-by-step procedure (Hannigan et al., 2016)

Step 1 Assume soil consolidation and ground settlement will occur.

Step 2 Using an appropriate static analysis method for the pile type and subsurface conditions, determine the nominal shaft, mobilized toe, and total mobilized resistance as a function of pile penetration depth.

Shaft resistance is typically fully mobilized at relatively small pile movements of 0.10 inches or less. The full toe resistance, however, may require a toe movement as much as 4 to 5% of the pile diameter depending on the geomaterial at the pile toe. An assessment of the mobilized toe resistance magnitude can be made using engineering judgment along with t-z and q-z

behavior in static analysis software, or from t-z and q-z values derived from instrumented static load tests.

Example output of the required static analysis results versus pile penetration depth is included in Fig. 5-1. An illustration of the percentage toe resistance mobilized relative to the toe movement normalized by the pile diameter is presented in Fig. 5-2.

Step 3 Select the pile toe elevation for analysis.

Step 4 Develop the axial load and resistance versus depth diagram at the selected pile toe elevation.

Plot the accumulated shaft resistance versus depth ($\sum R_s$) from Step 2 on the load and resistance diagram. This is depicted by the solid line in Fig. 5-3.

Determine the unfactored permanent load on the pile. Add the unfactored permanent load to the accumulated shaft resistance versus depth. This is indicated by the solid line in Fig. 5-4.

Subtract the sum of the accumulated shaft resistance at a given depth from the nominal resistance at the selected pile toe elevation ($R_n - \sum R_s$). Plot this resistance on the load and resistance diagram. This is denoted by dashed lines in Fig. 5-5. Graphs a, b, and c, represent the total mobilized resistance based on the shaft resistance plus a mobilized toe resistance of 100%, 50%, and 0% of the nominal toe resistance, respectively.

Step 5 Determined the location of the neutral plane, the magnitude of the maximum axial compression load in a pile, and the magnitude of the drag force.

For the example given in Figure 5-6, the neutral plane occurs at depth A, B, or C, depending on the magnitude of the mobilized toe resistance. If 100% of the toe resistance is mobilized, the neutral plane occurs at a depth of 30 feet (point A), the maximum axial load in a pile is 80 tons, and the drag force is 40 tons (80 tons – 40-ton permanent pile head load). Conversely, if no toe resistance is mobilized, the neutral plane occurs at a depth of 20 feet (point C), the maximum axial load in a pile is 60 tons, and the drag force is 20 tons (60 tons – 40-ton permanent pile head load).

Step 6 Check the structural strength limit state due to loading conditions, including drag force. The factored structural resistance of the pile in the strength limit state in axial compression, *Pr,* must exceed the factored permanent load and factored drag force per Eq. 7-70.

$$1.25\ (Q_d) + \gamma_p(DF) < P_r \quad (5\text{-}1)$$

Where Q_d is the permanent load on the pile (kips), DF is the drag force on the pile (kips), γ_p is the load factor for drag force in neutral plane analysis, and P_r is the factored axial compression resistance of pile (kips).

An AASHTO load factor for drag force, γ_p, determined by static analysis methods using the neutral plane procedure is not yet available. Therefore, local calibration is required for the implementation of this approach. The Minnesota DOT has adopted a load factor of 1.1 for drag force with the neutral plane downdrag procedure while a local calibration effort is in progress. This load factor was based on an equivalent minimum factor of safety 1.5 for material strength evaluation.

Step 7 Calculate the settlement due to downdrag with respect to the neutral plane.

a. Calculate the thickness of compressible soil, $t_{soil,}$ beneath the neutral plane.

$$t_{soil} = D_{il} - D_{np} \quad (5\text{-}2)$$

Where t_{soil} is the thickness of compressible soil beneath neutral plane (feet), D_{il} is the depth from reference to the top of the incompressible layer (feet), and D_{np} is the depth from reference to the neutral plane (feet).

b. Determine settlement due to downdrag from stress increase.

$$S_{dd} = t_{soil}\left(\frac{\gamma_p \Delta\sigma}{E_s}\right) \quad (5\text{-}3)$$

Where S_{dd} is the settlement due to downdrag (feet), $\Delta\sigma$ is the increase in vertical stress (ksf), and E_S is the elastic modulus of in-situ soil (ksf).

It should be noted that effective stress changes such as approach fill placement after pile driving will alter the plot of the permanent load

plus cumulative shaft resistance. This will, in turn, alter the location of the neutral plane, the maximum compression force in the pile, the magnitude of the drag force, and calculated settlement due to downdrag. Similarly, changes in the permanent load to be applied to the pile or changes in the pile toe elevation will also alter the analysis results.

5.3 Developed downdrag model

The interaction between the pile and the surrounding soil profile is a function of the amount and direction of the mobilized soil-pile relative displacement (δ_r). The development of the shear resistance on the pile side (i.e., skin resistance) requires a positive δ_r where the displacement of the pile segment (i) at that particular depth is larger than the displacement of the surrounding soil. However, some soil layers around the pile could experience settlement values larger than those of the adjacent pile segments, which generate negative values of δ_r and associating downward (driving) shear stresses on the pile side (i.e., a downdrag force). It should be noted that the mobilized negative (downdarg) and positive (resistance) pile side forces and the associating mobilized pile end bearing resistance are highly influenced by the soil-pile relative displacement (δ_r). Therefore, pile and soil settlement profiles should be coupled with the pile side and toe load-displacement relation ships (i.e., t-z and q-z, respectively) to capture the equilibrium between the mobilized driving and resisting forces.

Since the soil properties and the soil-pile interaction varies with depth, the proposed technique models the pile and surrounding soils in segments and sublayers, respectively, of equal thicknesses as described in Fig. 5-7. While the pile mobilized end bearing resistance is modeled via a nonlinear q-z spring at the pile toe, the negative (driving) and positive (resisting) side friction are modeled through a set of nonlinear t-z springs, as shown in Fig. 5-7. In addition, a linear spring relationship models the elastic compression of the pile segment materials (Fig. 5-7). It should be noted that the presented research employs the side load transfer curves developed by Ashour et al. (2010); Ashour and Helal (2017); and Ashour and Abbas (2020). The pile tip load-settlement relationships developed by Elfass (2001) and Elfass et al. (2009) for sandy and clayey soils, respectively, are also adopted in the proposed model (described in chapters 3 and 4).

5.3.1 Downdrag and load distribution assessment procedure

The pile segments and surrounding soil sublayers are numbered in ascending order from the pile tip to the pile top. Each pile segment is subjected to a force at its top and bottom $(Q_t)_i$ and $(Q_b)_i$, respectively, in addition to a vertical side shear force (T). The direction of side shear, either downwards or upwards (i.e., negative or positive) at the soil-pile interface (i.e., the pile segment and soil sublayer under investigation) is contingent on whether the soil settles more than the pile, or the pile settles more than the soil, respectively. Nevertheless, the mobilized value of negative or positive side shear depends on the value of the relative displacement (δ_r) between the soil and pile. It should be emphasized that the plane at which the soil and pile settlements are the same (i.e., the location where the pile side shear reverses from negative to positive) is the location of the neutral plane.

The evaluation of the drag force and load distribution along the pile length initially relies on the assessment of the cumulative soil settlement S_i of each soil sublayer due to the inundation of the collapsible soil layer(s) and its impact on the overlaying soil layers. The evaluation of the driving or resisting forces acting on the pile in the suggested technique starts with the first segment (i = 1) at the pile tip and then advances upward to the pile top (i = n). Hence, the type and properties of the soil sublayer in which the pile tip is embedded are identified. A minimal initial value of pile tip settlement is assumed $(Z_b)_{1\ assumed}$, and the associated pile tip resistance is calculated based on the employed end bearing model of that soil sublayer. Since only the relative settlement between the pile tip and soil mobilizes the pile end bearing resistance, the actual settlement at the pile tip $(Z_b)_{1\ actual}$, which is associated with the calculated value of tip resistance $(Q_b)_1$ is equal to the settlement of the soil sublayer adjacent to the pile tip segment (i =1) plus the assumed value of the pile tip settlement, as given in Eq. 5-4.

$$(Z_b)_{1\ actual} = (Z_b)_{1\ assumed} + S_1 \tag{5-4}$$

The calculation process of the pile load-settlement (starting with i = 1) continues to evaluate the segment's midpoint settlement $(Z_{mid})_i$ which is taken equal to the elastic compression of the lower half of the pile segment (Z') plus its base settlement $(Z_b)_i$. Z' is assumed to be zero in the first trial. It should be noted that $(Z_{mid})_i$ is compared to the settlement at the midpoint of the soil sublayer $(S_{mid})_i$, which is surrounding the pile segment (i) in question. If $(Z_{mid})_i$ is larger than $(S_{mid})_i$ (i.e., the downward vertical displacement of the pile segment i

exceeds the soil settlement at that depth), the pile segment would be subjected to upward (i.e., positive) side shear resistance (Fig. 5-8). However, if $(Z_{mid})_i$ is less than $(S_{mid})_i$, the pile segment would be subjected to negative skin friction (downward side shear stress), as described in Fig. 5-8.

The magnitude and direction of the mobilized side shear stress (τ_o) at the soil-pile interface depends on the value of the relative settlement (δ_r) between the pile segment and adjacent soil sublayer. τ_o is determined from the load transfer model of that soil sublayer (Chapters 3 and 4) as a function of the absolute value of δ_r as given in Eq. 5-5.

$$(\delta_r)_i = (Z_{mid})_i - (S_{mid})_i \tag{5-5}$$

On the other hand, the force $(Q_t)_i$ at the top of the pile segment i and displacement $(Z')_i$ are calculated as a function of the T_i, $(Q_b)_i$, and the pile properties as presented in Eqs. 5-6 and 5-7. This process is repeated until acceptable convergence of Z' is obtained. The values of T_i and $(Q_t)_i$ obtained from the last iteration are then used to determine the elastic deformation (Z") of the segment i and its top settlement $(Z_t)_i$ as given in Eqs. 5-8 and 5-9, respectively.

$$(Q_t)_i = (Q_b)_i \pm T_i \tag{5-6}$$

$$(Z')\mathrm{i} = \frac{(3Q_b+Q_t)_i \, \mathrm{H_s}}{8A_bE_p} \tag{5-7}$$

$$(Z'')\mathrm{i} = \left(\frac{Q_b+Q_t}{2}\right)\left(\frac{\mathrm{H_s}}{A_bE_p}\right) \tag{5-8}$$

$$(Z_t)_i = (Z_b)_i + (Z'')_i \tag{5-9}$$

Where $\mathrm{H_s}$ = the height of the pile segment and the soil sublayer; and E_p = pile material Young's modulus. It should be noted that the segments' top force $(Q_t)_i$ increases from one segment to another (moving upward, i = 1 through n) and then subsequently decreases once the segments experience negative skin friction. The current segment $(Q_t)_i$ and $(Z_t)_i$ are equated to the next segment's $(Q_b)_{i+1}$ and $(Z_b)_{i+1}$, respectively.

If $(Q_t)_i$ has a negative value at certain segment i, then a larger pile tip displacement $(Z_b)_1$ needs to be assumed, and the process should be repeated until the top pile segment (i = n) yields a value of $(Q_t)_i \geq$ zero. $(Q_t)_i$ and $(Z_t)_i$ of the pile top segment (i = n) form a point on the pile-

head load-displacement (Q-Z) curve. The above-mentioned procedure is repeated for larger values of $(Z_b)_{1\ assumed}$ to build the whole Q-Z curve until failure transpires. Failure for such a case can be characterized based on soil shear failure, excessive pile-head settlement, or the pile's structural capacity. It should be noted that the pile-head load obtained from the suggested technique represents a permanent and unfactored imposed pile load. Moreover, the obtained pile-head load-displacement curve represents a spectrum of pile displacement generated by different permanent pile-head loads and does not represent the mobilized pile stiffness under cyclic or transient loading. The flowchart presented in Fig. 5-9 illustrates in detail the above-mentioned procedure as implemented in the associating computer code (Drag_Pile).

5.3.2 Case Studies for Comparison and Validation

The suggested technique is validated through a number of comparisons with full-scale field tests conducted on piles embedded into collapsible soils and experiencing negative skin friction due soil inundation. Very few tests were conducted on piles embedded into inundated collapsible soils with measurements of induced downdrag forces acting on the pile.

5.3.3 Full Scale Pile Test at Nikopol Region [Grigorian 1997]

The proposed model has been validated using the results of a full-scale pile (bored and cast in situ types) reported by Grigorian (1997). Soil properties at the Nikopol region are given in Table 5-1. The installed pile had a length of 22 m and a diameter of 0.5 m. The full-scale pile test was conducted under prolonged wetting (from top) in a test pit (20-m x 20-m plan area and 1-m deep). The water level in the test pit was maintained at a height of 0.5 m for 2.5 months. The tested pile was equipped with three strain gauge dynamometers at 9.2, 12.3, and 22 m (pile tip) from the pile head. The longitudinal force (at the pile section) and the normal stress (at the pile base) were interpreted from the dynamometer readings. The pile head was subjected to an external load of 600 kN. The top to bottom inundation technique allowed the full saturation of the upper 6-m of the top collapsible soil that maintained an initial degree of saturation (S_{ro}) of 20%. It should be mentioned that the axial load at the pile head was applied after the soil was saturated which is consistent with the applied methodology.

As reported by Grigorian (1997), the collapsible soil had a Cp = 7. As shown in Fig. 5-10a, it can be seen that the predicted values of Cp varies with depth from 2.5 to 6.5, which is in a good agreement with experimental value. The drag force developed on the pile due to the soil

inundation increases with depth to reach its maximum value of 183 kN at 6-m depth below the ground surface, as presented in Fig. 5-11 (the axial load on the pile increased from 600 kN at the pile head to 783 kN at 6-m depth). The pile head settled 17.8 mm under the pile head load (600 kN) and the induced downdrag force (183 kN) as shown in Fig. 5-10b.

Table 5-1. Soil profile and properties at Nikopol test site (Noor et al. 2013 after Grigorian, 1997).

Depth (m)	w_n (%)	Void ratio, $e_{initial}$	w_{sat} (%)	γ_{sat}(kN/m^3)	C (kPa)	φ (degrees)
0–8	7	0.91	28.7	17.57	5	20
8–23	4.3	0.86	30.82	18.34	6	16
23–30	11.3	0.71	21.2	18.4	5	18

Table 5-2. Predicted and measured pile drag force and pile-head settlement for the Nikopol test.

Thickness of Collapsed Soil Layer (m)	Downdrag Force (kN)		Pile-Head settlement (mm)	Depth of Neutral Plane (N.P.) (m)
	Predicted	Measured		
6.0	183	186	17.8	5.7

5.3.4 Full Scale Pile Test at Volgodon Region [Grigorian 1997]

A second full-scale pile test (bored and cast in situ types) has been used to validate the presented approach reported by Grigorian (1997). Soil properties at the Volgodon region are given in Table 5-3. The installed pile had a length of 18 m and a diameter of 1.0 m. The pile, tested in Volgodon was equipped with three vibrating wire-type dynamometers (installed at depths of 5, 11, and 15 m from the pile head) and a ground dynamometer (at the pile tip). Local wetting of the collapsible soil layer was induced using a circular trench, 0.5-m wide and 1-m deep, dug around each pile. Four equally spaced vertical drainage holes (0.17 m in diameter and 16 m in length) were made at the bottom of the circular trench (Fig. 5-12). The lowest point of each drainage hole was 16.5 m from ground level. Both the circular trench and the drainage holes were filled with the draining material. Local wetting around the pile was induced after the pile was installed. According to the reported data, the bottom 4-m of the second collapsible soil (from depth 15-m up to 11-m below the ground surface) was subjected to the saturation process using the drainage hole (Fig. 5-12). Figure 5-13 shows the distribution of the downdrag and resisting force (-ve and +ve skin friction) acting on the pile and the settlement of both the soil and pile. It

can be noticed that the measured downdrag force acting on the pile is 740 kN, which is considerably less than the predicted one (1275 kN). Such a prediction of the downdrag force is consistent with the applied inundation process along with the depth and initial conditions of the inundated collapsible soil layer. It can be seen that saturation of the pile adjacent collapsible soil via the drainage hole could be insufficient to inundate an adequate and extended zone of soil around the pile. Moreover, the reported initial degree of saturation (S_{ro}) of the inundated soil was 56%, which was a high initial moisture content to induce any significant soil collapse after soil inundation as discussed earlier in Chapter 2. The reported experimental collapsible potential Cp = 8, which was not consistent with S_{ro} = 56%. Figure 5-14a displays rational values of Cp for inundated soil at depth 15 m up to 11 m below the ground surface. The developed procedure also allows the prediction of the post inundation soil and pile settlement, as shown in Fig. 5-14b.

Table 5-3. Soil profile and properties at Volgodon test site (Noor et al. 2013 after Grigorian 1997).

Depth (m)	w_n (%)	γ_{bulk} (kN/m^3)	G_s	e	S (%)	c (kPa)	φ (degrees)	Remarks
0–6	13.8	16.95	2.68	0.78	51	15	19	Collapsible
6–15	15	17.5	2.69	0.73	56	24	17	Collapsible
15–25	17.9	18.82	2.69	0.62	73	33	19	Noncollapsible, unsaturated
25–35	23.0	19.6	2.69	0.62	100	33	19	Noncollapsible, saturated

Table 5-4. Soil properties at the Volgodon region.

Thickness of Collapsed Soil Layer (m)	Downdrag Force (kN)		Pile-Head Settlement (mm)	Depth of Neutral Plane (N.P.) (m)
	Predicted	Measured		
4.0 m	1275	740	30	13

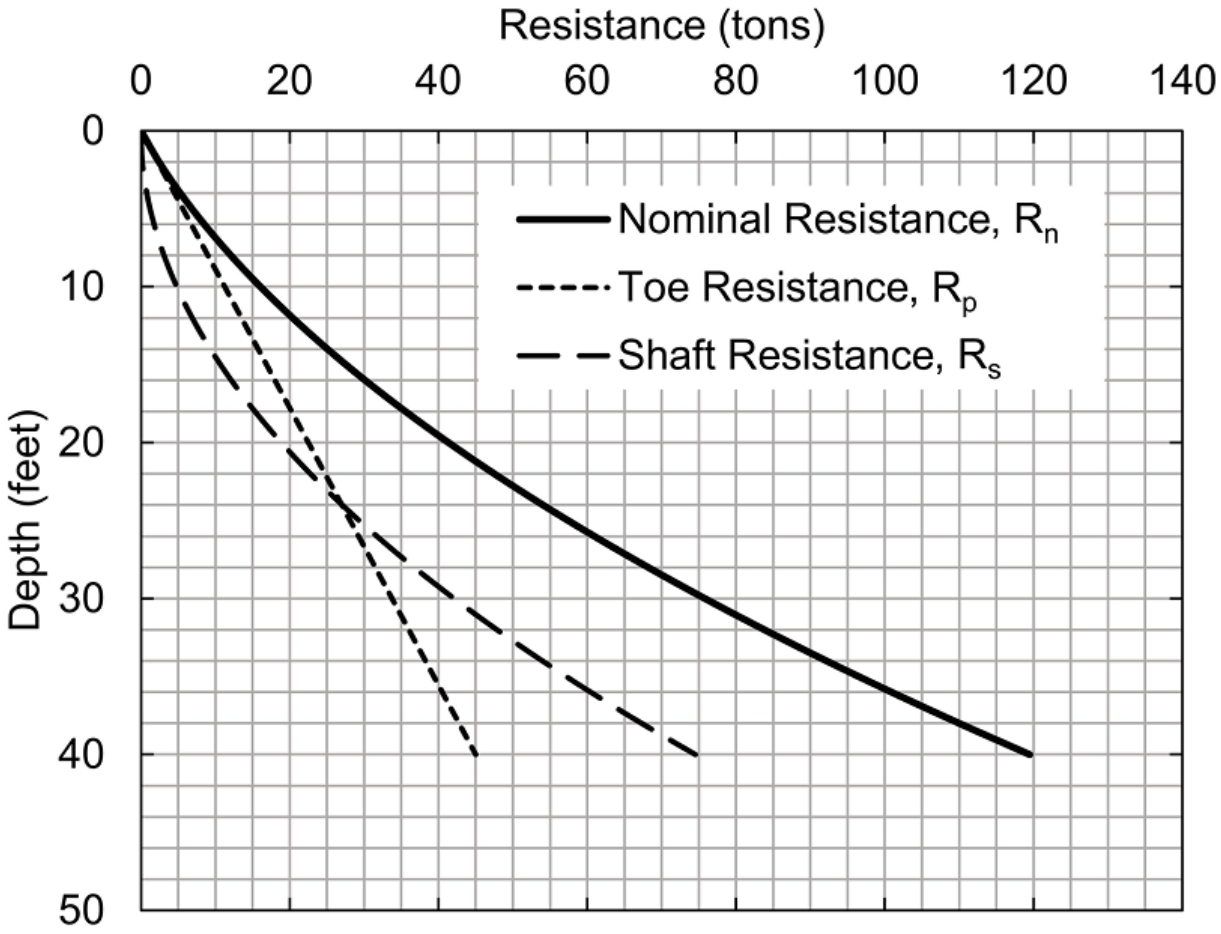

Fig. 5-1. Plot of static analysis results (after Siegel et al., 2013).

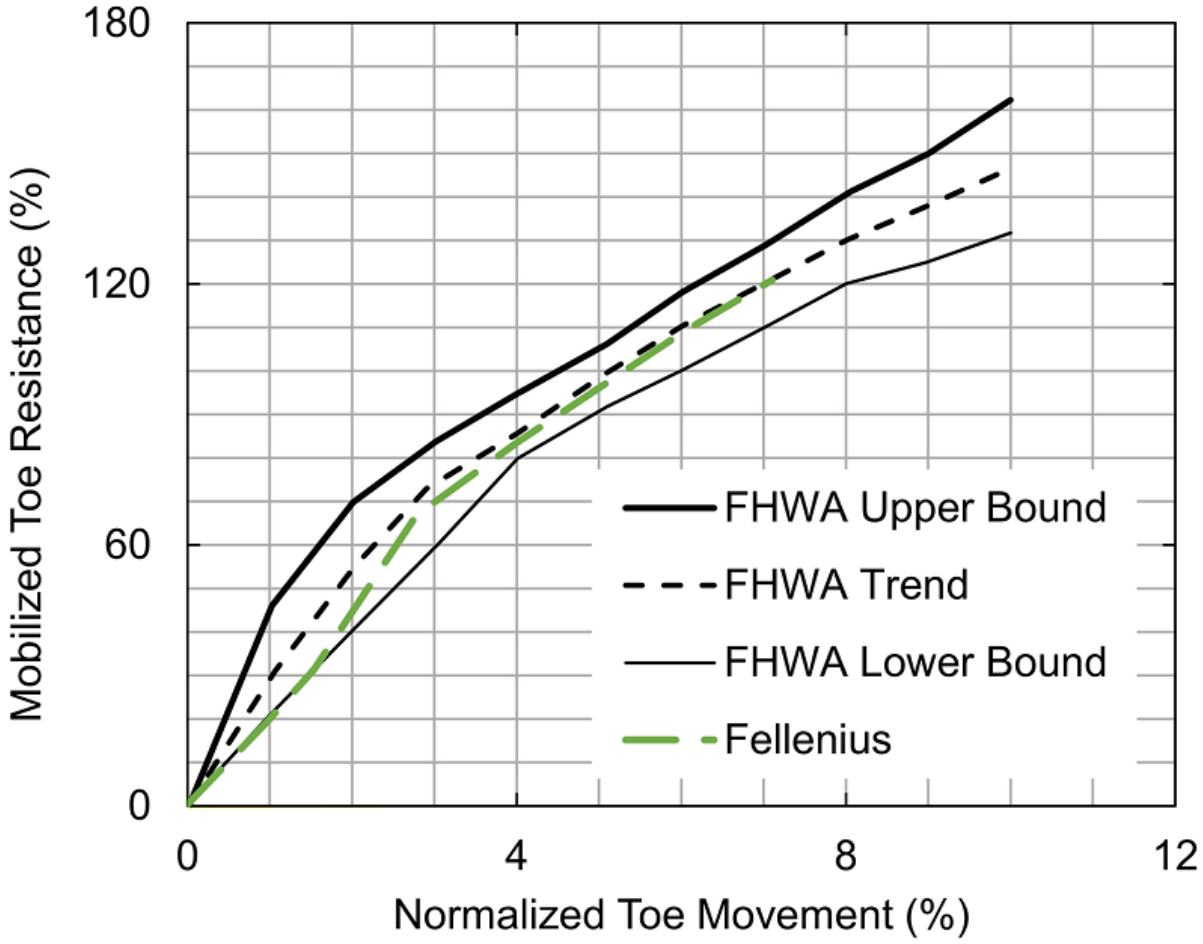

Fig. 5-2. Plot of normalized toe resistance versus toe movement (after Siegel et al. 2013).

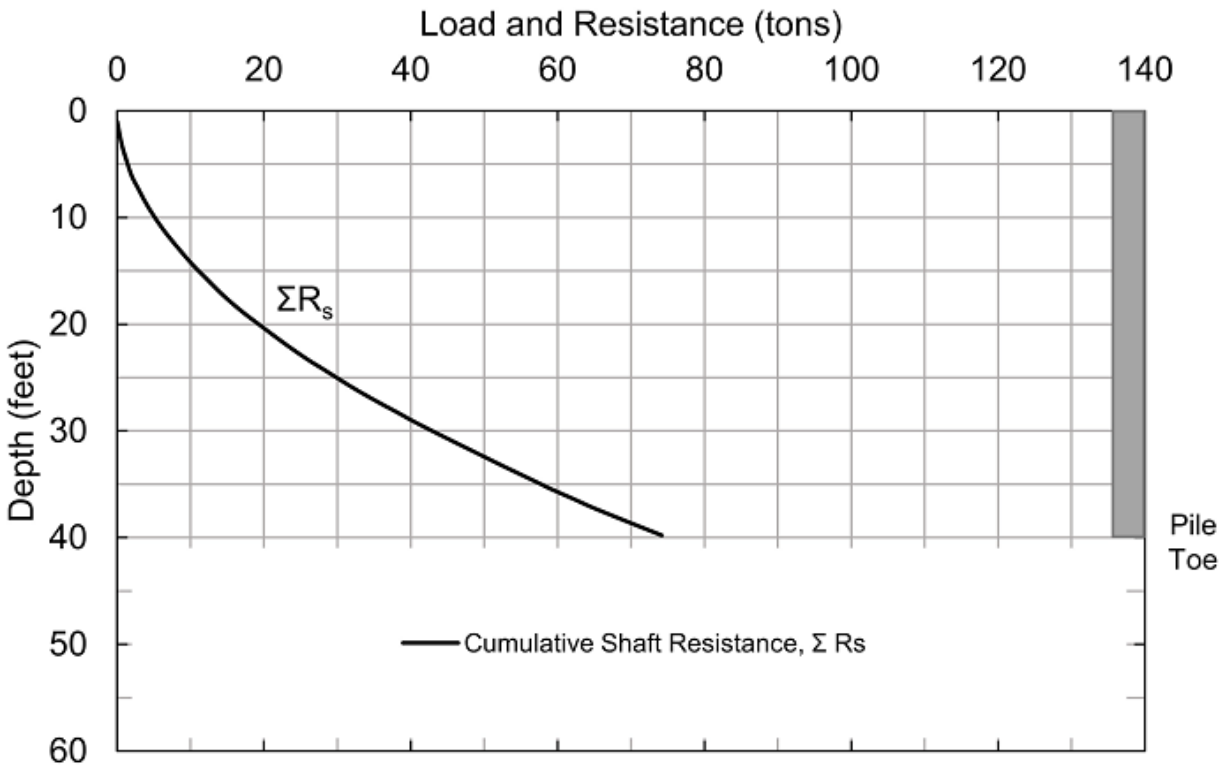

Fig. 5-3. Axial load and resistance plot cumulative shaft resistance vs. depth (after Siegel et al., 2013).

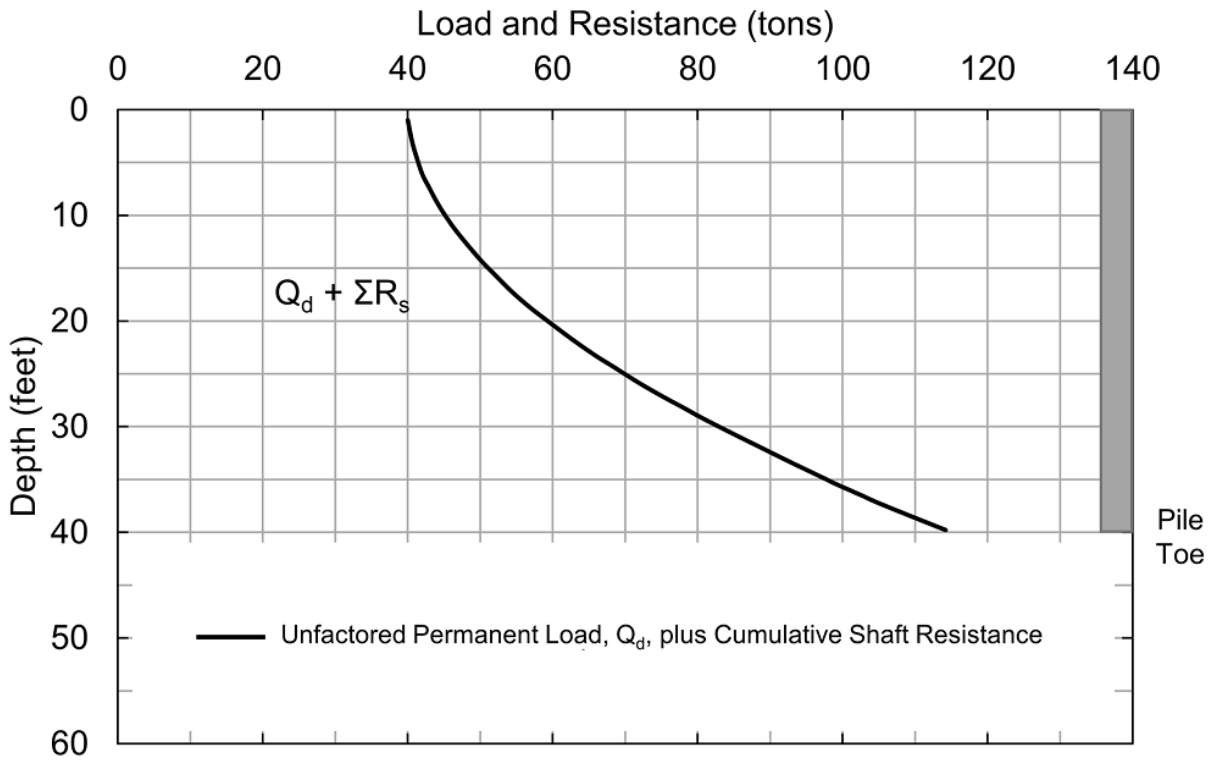

Fig. 5-4. Axial load and resistance plot of unfactored permanent load plus cumulative shaft resistance vs. depth (after Siegel et al., 2013).

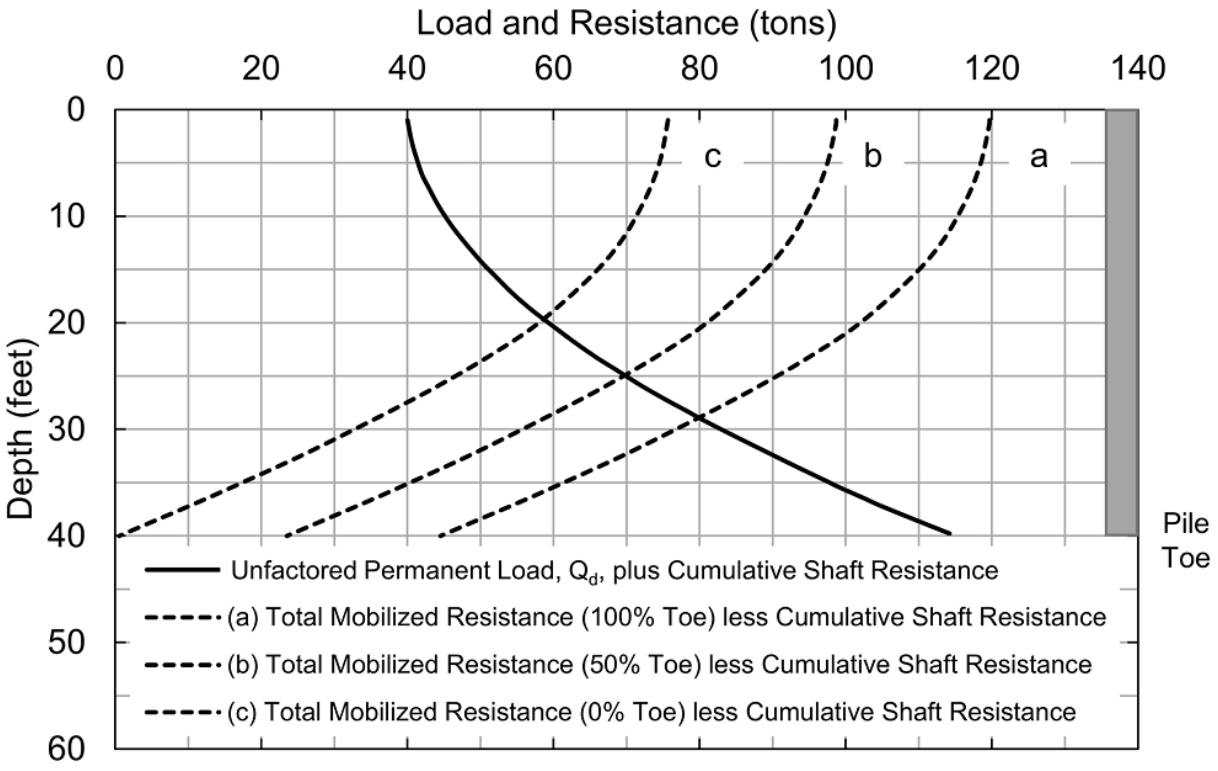

Fig. 5-5. Axial load and resistance plot, including mobilized resistances (after Siegel et al., 2013).

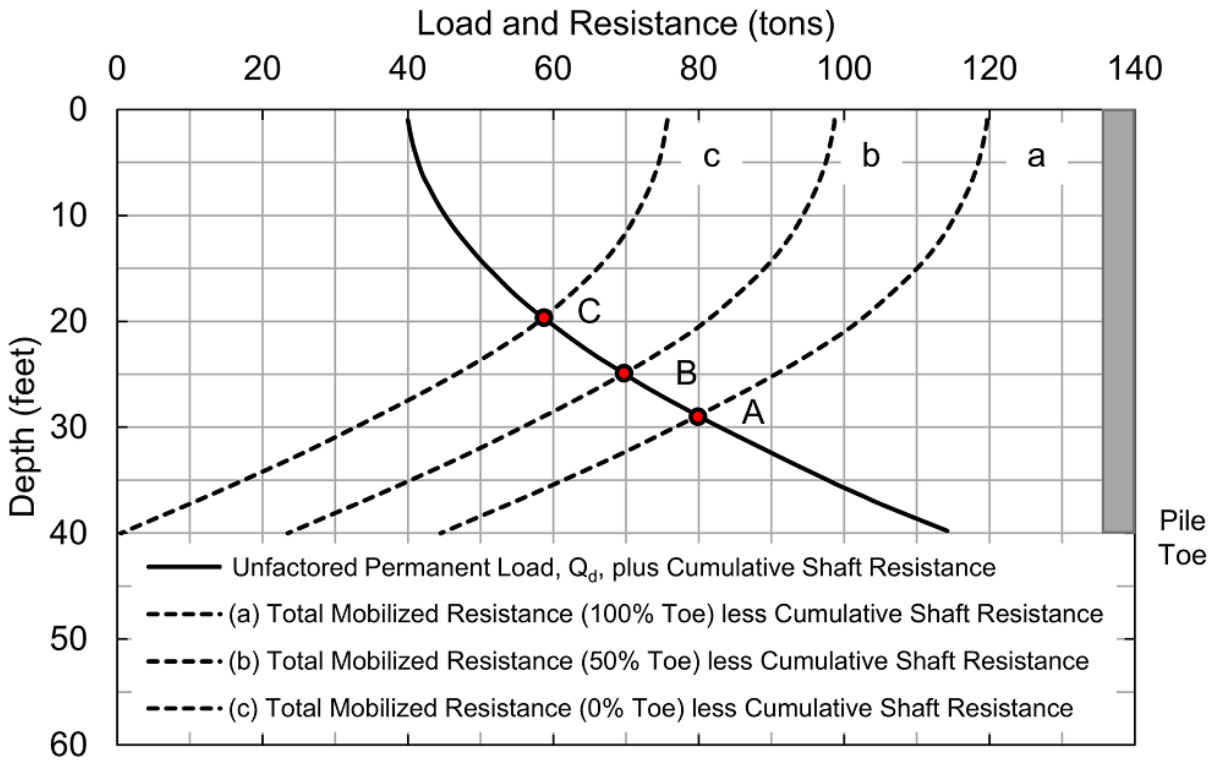

Fig. 5-6. Axial Load and resistance plot, including neutral plane location based on mobilized toe resistance (after Siegel et al., 2013).

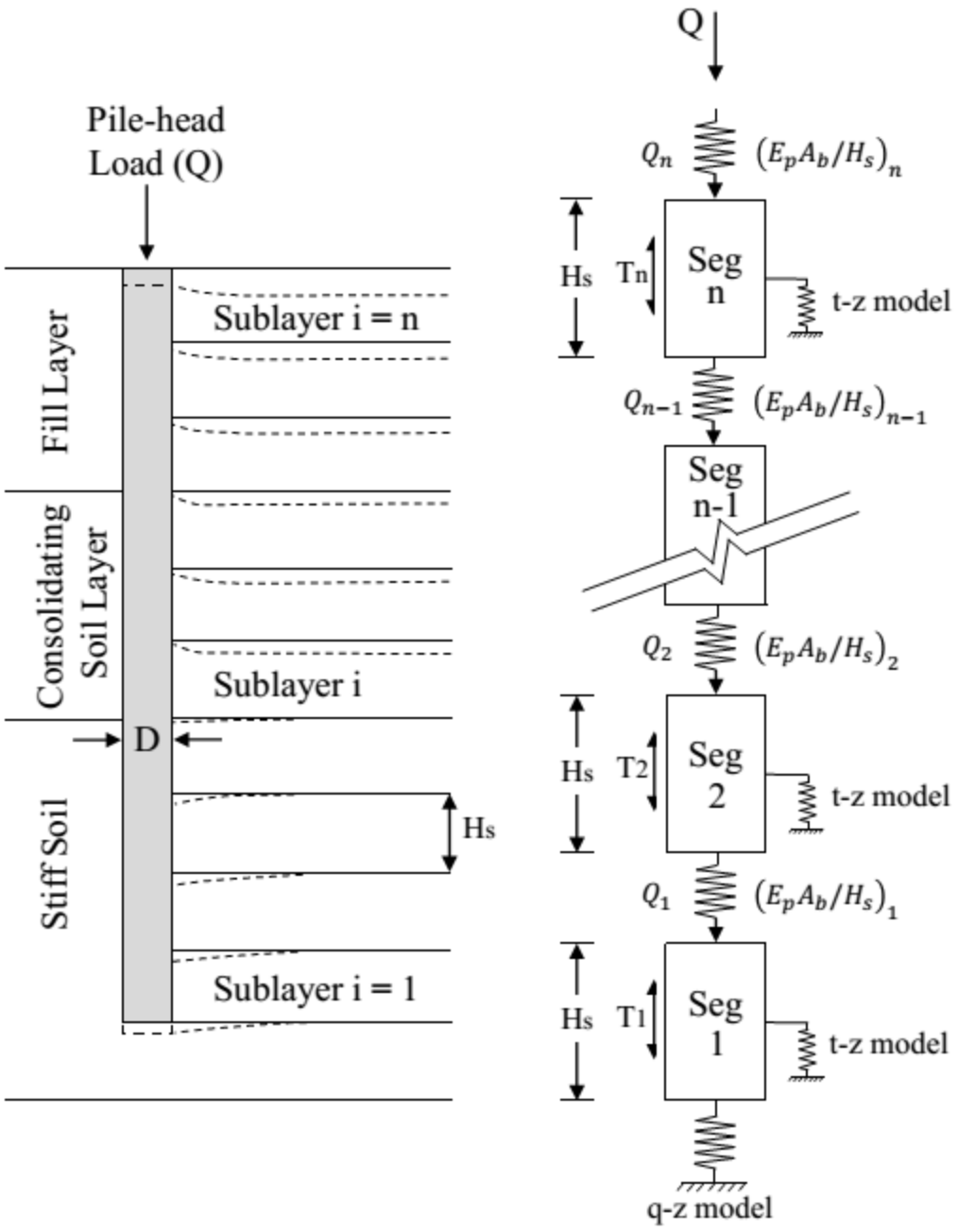

Fig. 5-7. Soil-pile modeling in sublayers and segments with a set of t-z and q-z springs.

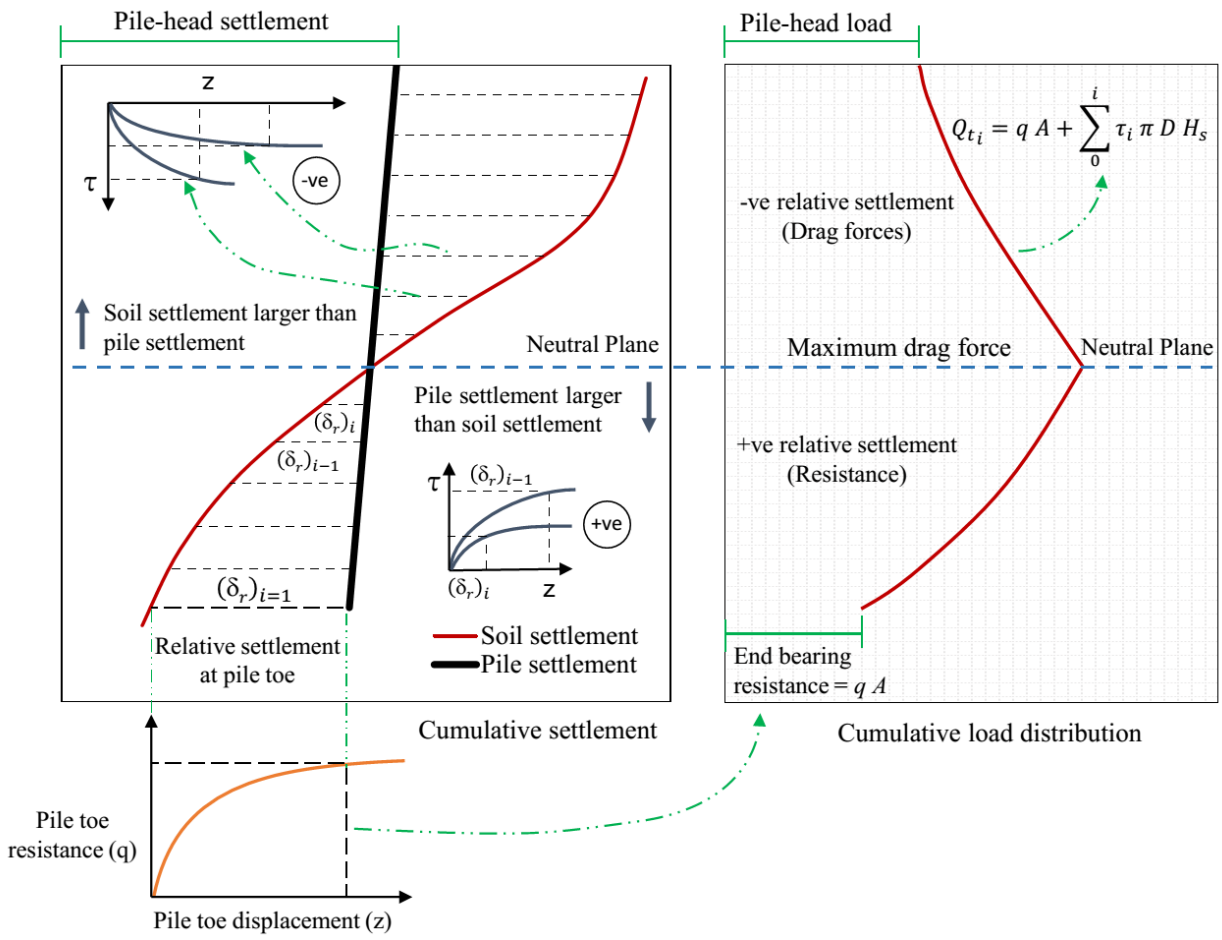

Fig. 5-8. Pile and soil settlement profiles coupled with pile side/toe load-displacement relationships to capture the mobilized response of a pile subjected to negative skin friction.

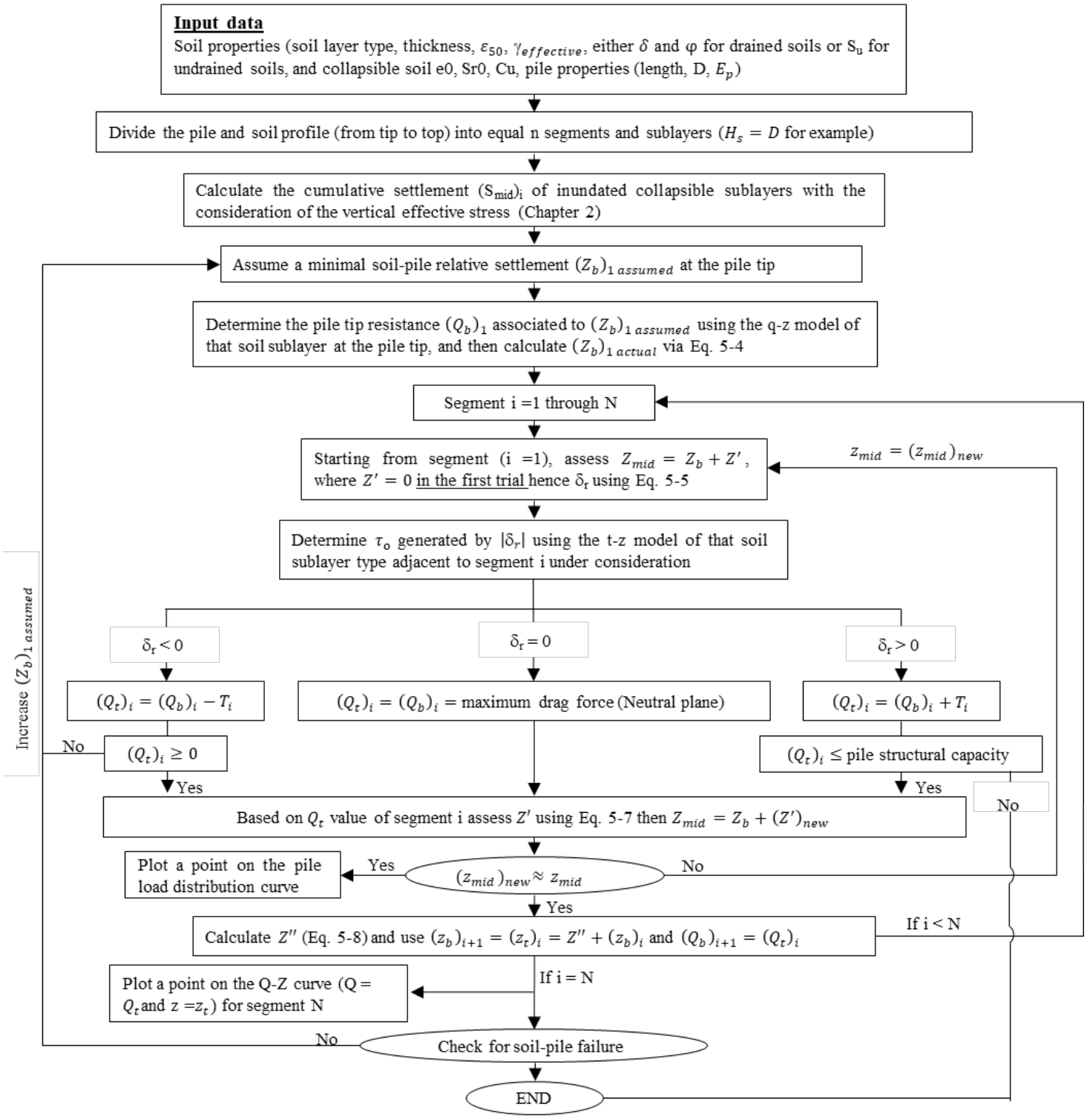

Fig. 5-9. Flowchart for the implemented procedure of downdrag force/settlement acting on a pile embedded into inundated collapsible soil(s).

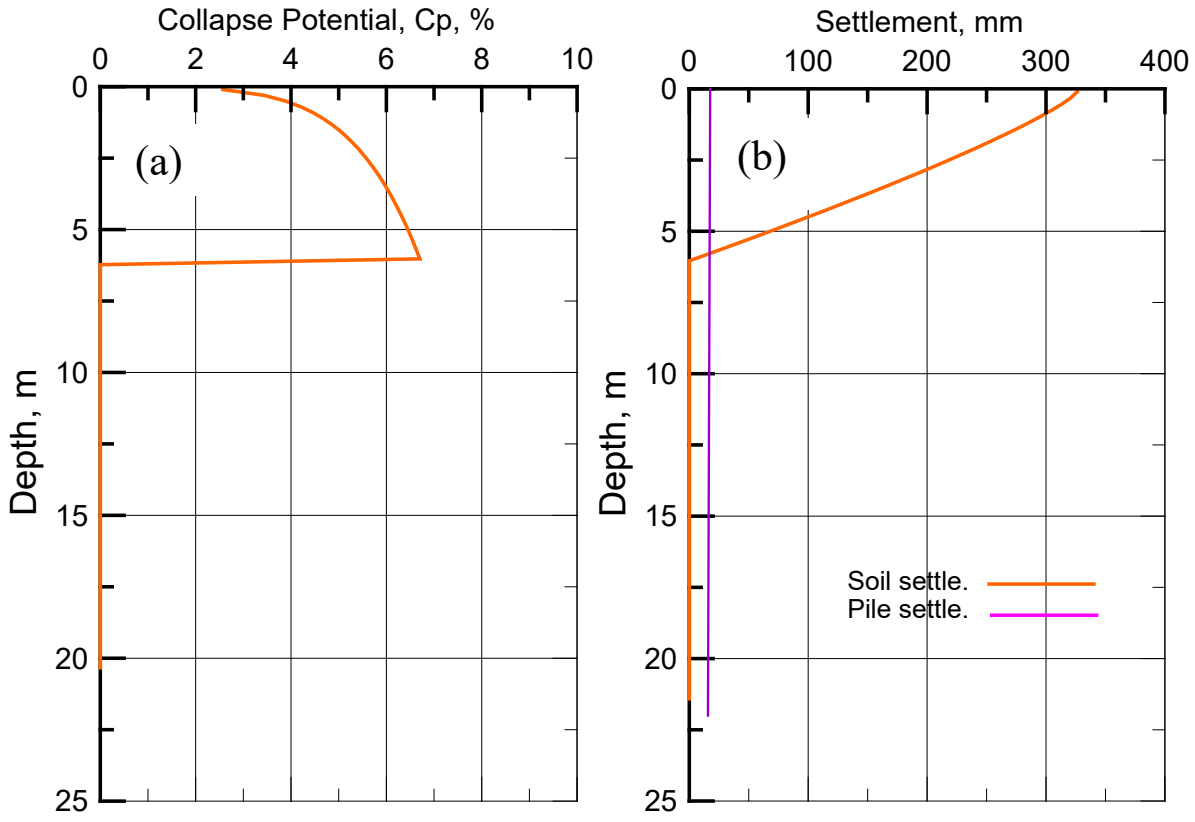

Fig. 5-10. (a) Predicted values of Cp over the depth at Nikopol Test (b) Predicted soil and pile settlement of inundated soil at Nikopol Test.

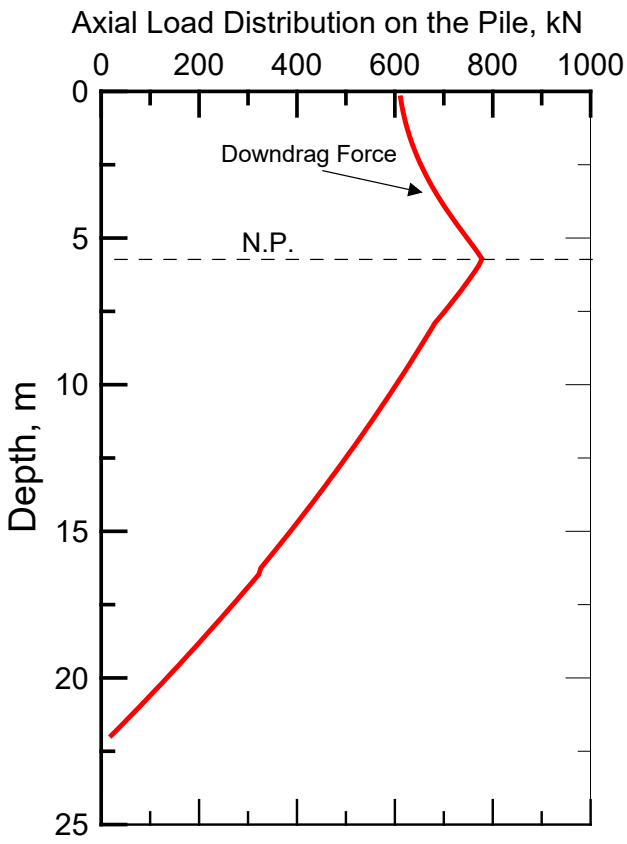

Fig. 5-11. Downdrag and resistance force along the pile at Nikopol test.

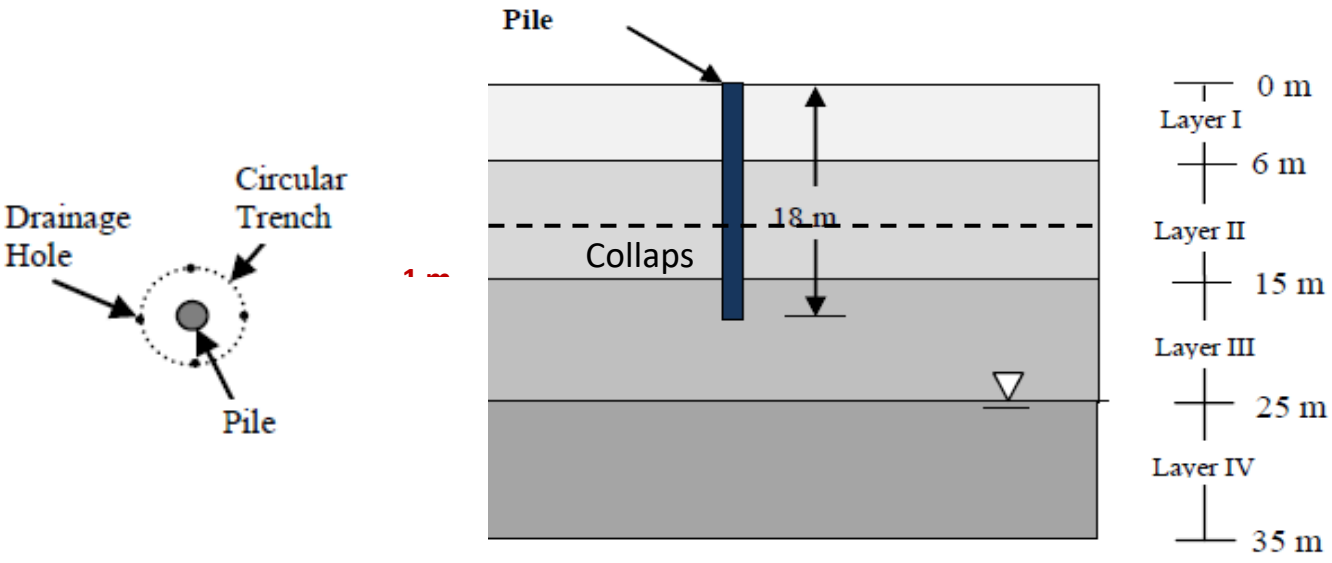

Fig. 5-12. Saturation drain holes and soil profile at Volgodon Region (Grigorian, 1997 and Noor et al., 2013).

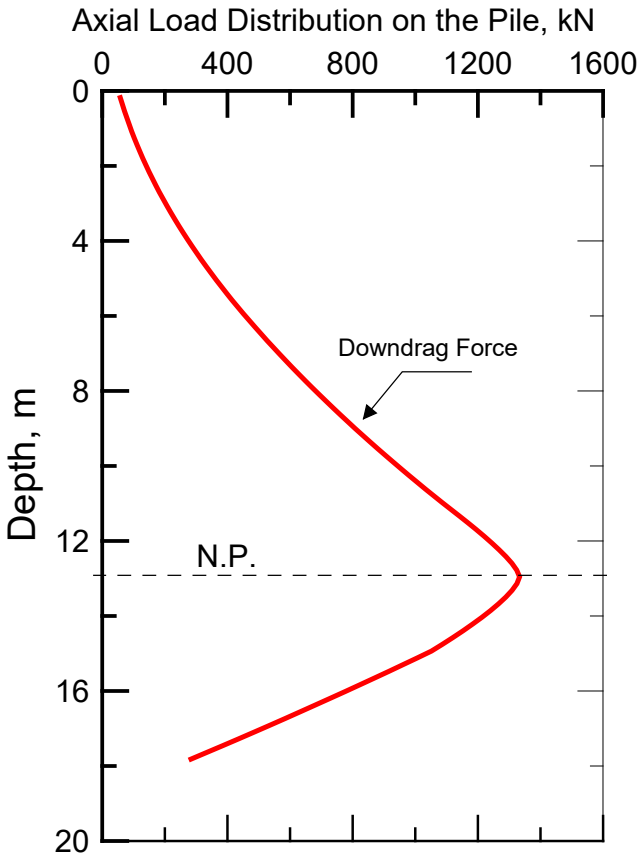

Fig. 5-13. Soil and pile settlement profiles for a 43-m long pile test in Tokyo, Japan.

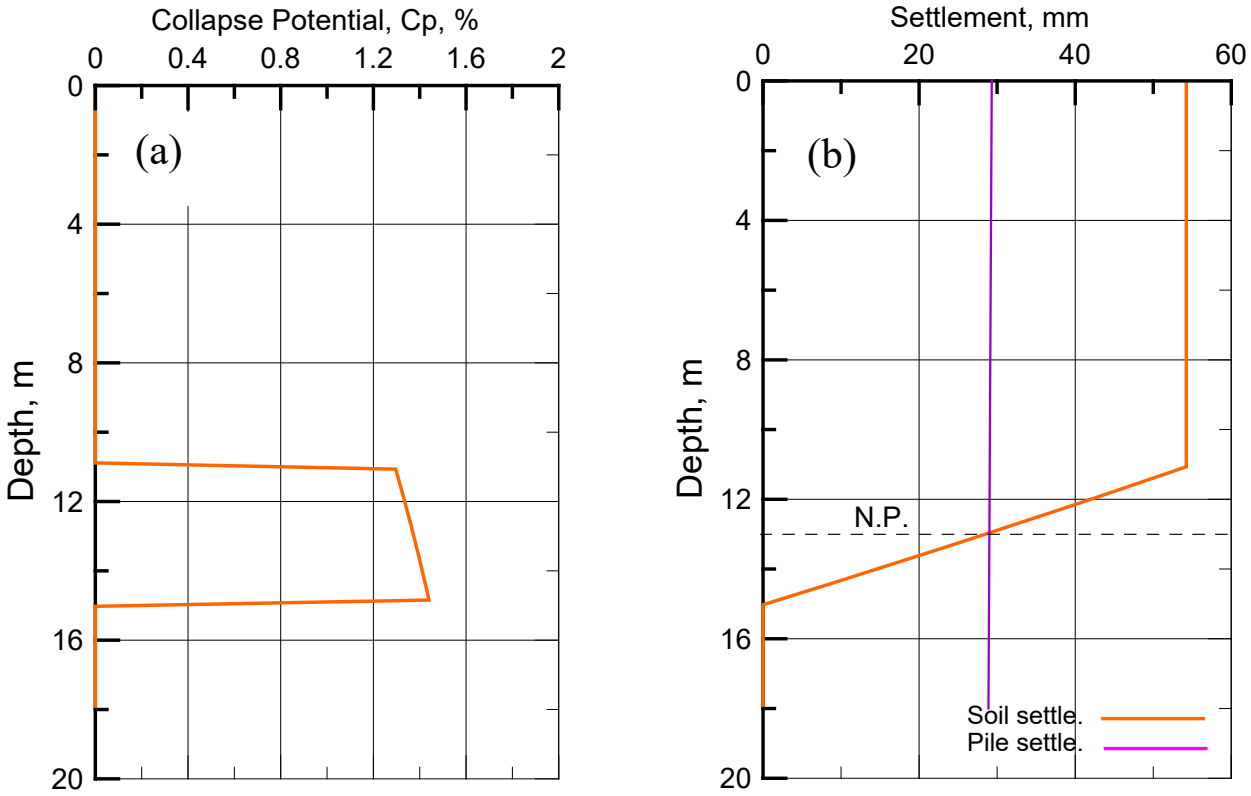

Fig. 5-14. (a) Predicted values of Cp over the depth settlement of inundated soil at Volgodon Test (b) Predicted soil and pile of inundated soil at Volgodon Test.

Chapter 6. References

American Association of State Highway and Transportation Officials (AASHTO). (2014). AASHTO LRFD Bridge Design Specifications, US Customary Units, Seventh Edition, with 2015 Interim Revisions. American Association of State Highway and Transportation Officials, Washington, D.C., 1960 p

Arman, Ara, and Samuel I. Thornton. Collapsible soils in Louisiana. No. Bulletin No. 111. Louisiana State University, Baton Rouge, 1972.

Ashour, M., Abbas, A., and Boskovic, S. 2019. "Pile cap interaction with bridge pile foundations under lateral loads." J. Bridge Eng. 24 (6): 04019053. https://doi.org/10.1061/(ASCE)BE.1943-5592.0001408.

Ashour, M., and A. Helal. 2017. "Pre-Liquefaction and post-liquefaction responses of axially loaded piles in sands." Int. J. Geomech. 17 (9): 04017073. https://doi.org/10.1061/(ASCE)GM.1943-5622.0000968.

Ashour, M., Norris, G., Elfass, S., and Al-Hamdan, A. (2010). "Mobilized side and tip resistances of piles in clay." Computers and geotechnics 37(7-8), pp 858-866. https://doi.org/10.1016/j.compgeo.2010.07.005

ASTM., 2004. Standard test method for measurement of collapse potential of soils. Designation: D 5333, American society for testing and materials.

Basma, A., and Tuncer, R., 1992. "Evaluation and control of collapsible soils." Journal of Geotechnical Engineering. 10.1061/(ASCE)0733-9410(1992)118:10(1491).

Bolton, M.D. (1986). "The strength and dilatancy of sand."Géotechnique, 36 (1), 65-78.

Booth, A., 1977. "Collapse settlement in compacted soils." Council for Scientific and Industrial Research Report 324, National Institute for Transport and Road Research Bulletin 13, pp. 1–34.

Chow, H.S.W. (2007). “Analysis of piled-raft foundations with piles of different lengths and diameters.” PhD thesis, University of Sydney.

Clemence, S.P., Finbarr, A.O. (1981). "Design Considerations for Collapsible soils". Journal of the Geotechnical Engineering Division; Proc. ASCE

Coyle H.M., and Reese L.C., (1966). “Load transfer for axially loaded piles in clay.” J. Soil Mechanics and Foundations Division (ASCE) 1966;92 (SM2).

Dudley, J. H., (1970) "Review of Collapsing Soils," Journal of the Soil Mechanics and Foundation Division, ASCE, Vol. 97, pp. 925-947.

Elfass, S. (2001). “A new approach for estimating the axial capacity of driven piles in sand up to true soil failure.” Ph.D. thesis, Univ. of Nevada, Reno, NV.

Elfass M, Pooranampillai J., Elsayed A, and Norris G. (2009). “Undrained point load point displacement response of piles/drilled shafts in clay and sand.” International Foundation Congress and Equipment Expo. https://doi.org/10.1061/41022(336)23.

El-Howayek, A., Huang, P., Bisnett, R., and Santagata, M., (2011) "Identification and behavior of collapsible soils." Publication FHWA/IN/JTRP-2011/12. Joint Transportation Research Program, Indiana Department of Transportation and Purdue University, West Lafayette, Indiana, 2011. doi: 10.5703/1288284314625.

Endo, M., Minou, A., Kawasaki, T., and Shibata, T. (1969) “Negative skin friction acting on steel piles in clay.” In Proceedings of the 8th International Conference on Soil Mechanics and

Foundation Engineering, Mexico City, 25–29 August 1969. Mexico Geotechnical Society. Vol. 2, pp. 85–92.

Evans, Jr. L. T., and Duncan, G. M (1982). "Simplified Analysis of Laterally Loaded Piles." University of California Berkeley, Rept. No. UCB/GT/82-04; 1982.

Fellenius, B. (2006) " Results from long-term measurement in piles of drag load and downdrag." Canadian Geotechnical Journal, 2006, 43(4): 409-430. https://doi.org/10.1139/t06-009.

Fellenius, B.H. (1999). "Basics of foundation design. 2nd expanded edition."BiTech Publishers, Vancouver, 140 p.

Fellenius, B. 1989. "Unified design of piles and pile groups." Transportation Research Board Record 1169, pp. 75–82.

Grigorian, A. A., (1997) "Pile foundations for buildings and structures in collapsible soil", A.A. Balkema, Brookfield, VT.

Hannigan, P. J., Rausche, F., Likins, G. E., Robinson, B. R., and Becker, M. L. (2016). Geotechnical engineering circular No. 12 – Volume 1, Design and construction of driven pile foundations. FHWA-NHI-16-009. U. S. Dept. of transportation, FHWA, Washington, DC.

Habibagahli, G., and Taherian, M., 2004. "Prediction of collapse potential for compacted soils using artificial neural networks." Scientia Iranica, Sharif University of Technology 11(12), pp. 1-20.

Haeri, S., Khosravi, A., Garakani, A., and Ghazizadeh, S., 2016. "Effect of soil structure and disturbance on hydromechanical behavior of collapsible loessial soils." International Journal of Geomechanics. 10.1061/(ASCE)GM.1943-5622.0000656.Houston, S. L., Houston, E., Zapata, C., (2001) Lawrence Geotechnical engineering practice for collapsible soils Geotechnical and Geological Engineering, 19 (3) (2001), pp. 333-355

Indraratna, B., Balasubramaniam, A., Phamvan, P., and Wong, Y. 1992. Development of negative skin friction on driven piles in soft Bangkok clay. Canadian Geotechnical Journal, 29(3): 393–404. https://doi.org/10.1139/t92-044

Lommler, J.C., and Bandini, P. (2015). Characterization of collapsible soils. Proceedings of IFCEE 2015, San Antonio, Texas (2015)

Kalashnikova, O. (1976) "Investigation of the behavior of piles in a collapsible soil stabilized through a leading hole" Soil Mechanics and Foundation Engineering, 13: 16–19.

Knodel, P. C. (1992). Characteristics and the problems of collapsible soils. Bureau of Reclamation, Materials Engineering Branch Research and Laboratory Services Division. U.S. Department of the Interior, Denver (1992)

Kraft, L.M., Richard, P.R., and Kagawa, T. (1981). "Theoretical t–z curves."J. Geotech. Engrg. Div., 107(11), 1543–1561.

Lawton, E., Fragaszy, R., and Hardcastle, J., 1989. "Collapse of compacted clayey sand." Journal of Geotechnical Engineering. 10.1061/(ASCE)0733-9410(1989)115:9(1252).

Mashhour, I., and Hanna, A. (2016) "Drag load on end-bearing piles in collapsible soil due to inundation" Can Geotech J 53(12):2030–2038.

Medero, G., Schnaid, F., and Gehling, W., 2009. "Oedometer behavior of an artificial cemented highly collapsible soil." Journal of Geotechnical and Geoenvironmental Engineering. 10.1061/ASCE1090-02412009135:6840.

Milovic., D., 1988. "Stress deformation properties of macroporous loess soils." Engineering Geology, Vol 25 pp 283-302. 10.1016/0013-7952(88)90033-6.

Norris, G. M. (1986). "Theoretically based BEF laterally loaded pile analysis." Proc., Numerical Methods in Offshore Piling: 3rd Int. Conf., Editions Technip, Paris, 361–386.

Noor S.T., Hanna A., and Mashhour I. (2013) “Numerical modeling of piles in collapsible soil subjected to inundation” International Journal of Geomechanics, 13(5): 514–526.

Naval Facilities Engineering Command (NAVFAC). (1986). Foundations and earth structures. Design manual 7.02, Naval Facilities Engineering Command, Alexandria, VA.

Owens, R. L, and Rollins, K. M. (1990) “Collapsible soil hazard mapping along the Wasatch Range” Utah, USA. In: Proceedings of the 6th international IAEG congress, Amsterdam, pp 221–227

Popescu, M., 1986. “A comparison between the behaviour of swelling and of collapsing soils.” Engineering Geology, Vol 23 pp 145-163. 10.1016/0013-7952(86)90036-0.

Qian, Z., Yang, W., Lu, X., and Qiang, C. (2014) "Behaviour of micropiles in collapsible loess under tension or compression load." Geomechanics and Engineering, Vol. 7, No. 5 (2014) 477-493. 10.12989/gae.2014.7.5.477.

Reginatto, A., and Ferrero, J., 1973. "Collapse potential of soils and soil-water chemistry." In: Proceedings of 8th international conference on soil mechanics and foundation engineering, vol 2. Moscow, pp 177–183. 10.1016/0148-9062(75)90062-5.

Rinaldi, V., and Capdevila, J., 2006. "Effect of cement and saturation on the stress-strain behavior of a silty clay." Fourth international conference on unsaturated soils (ASCE). 10.1061/40802(189)94.

Richart E. F., (1975). “Some effects of dynamic soil properties on soil-structure interaction.” J. Geotech Engg Division (ASCE) 1975;101(GT12):1197-240.

Robinsky, E. I., and Morrison, C. E. (1964). “Sand displacement and compaction around model friction piles.” Can. Geotech. J., 1(2), 81–93.

Roullier, P. (1992) "Hydrocollapsible soil correlations." University of Nevada, Las Vegas Retrospective Thesis & Dissertations. 216.

Randolph, M. F., (2003) “43rd Rankine Lecture: Science and empiricism in pile foundation design.” Géotechnique 2003;53(9):785-796.

Seo, H., Prezzi, M., and Salgado, R. (2008). “Settlement analysis of axially loaded piles.”Proc. of the 6th Int. Conf. on Case Histories in Geotech. Engrg. and Symposium, Arlington, VA.

Siegel, T., Lamb, R., Dasenbrock, D., and Axtell, P.J. (2013). “Alternative Design Approach for Drag Load and Downdrag with the LRFD Framework.” Proceedings of the 38th Annual Conference on Deep Foundations 2013, Phoenix, AZ, pp. 23-39

Schnertmann, J. H. (1970). “Static cone to compute static settlement over sand.”J. Geotech. Engrg. Div., 96(3), 1011–1043.

Schnertmann, J.H., Hartman, J.P., and Brown, P.R. (1978). “Improved strain influence factor diagram.”J. Geotech. Engrg. Div., 105(6), 715–726.

Skempton A. W., (1951). “The bearing capacity of clays.” In Proceedings of Bldg, Research Congress, vol. I; 1951.

Abid-Awn, S. H., and Hussain, H. Q., (2017) “Pullout Capacity of Piles in Collapsible Soil” International Journal of Engineering Trends and Technology (IJETT) – Volume 51 Number 3 September 2017 ISSN: 2231-5381

White, J. L., (2007). Characteristics and susceptibility of collapsible soils in Colorado: results of a Statewide study. In Proceedings of the 2006 Biennial Geotechnical Seminar (GEO-Volution) (pp. 86-98). Denver: ASCE. https://doi.org/10.1061/40890(219)6

Williams, T., and Rollins, K., 1991. Collapsible soil hazard map for the cedar city, Utah Area. Utah department of natural resources. Report 91-10.

Zaretskii, Yu, K., and Karabaev, M. I., (1987) “Analysis of settlements of bored-cast-in-place piles in collapsible soils” Soil Mechanics and Foundation Engineering volume 24, pages13–19 (1987)